OULU 2016
C 563

ACTA UNIVERSITATIS OULUENSIS

Jarkko Huusko

COMMUNICATION PERFORMANCE PREDICTION AND LINK ADAPTATION BASED ON A STATISTICAL RADIO CHANNEL MODEL

UNIVERSITY OF OULU GRADUATE SCHOOL;
UNIVERSITY OF OULU,
FACULTY OF INFORMATION TECHNOLOGY AND ELECTRICAL ENGINEERING;
CENTRE FOR WIRELESS COMMUNICATIONS;
INFOTECH OULU

ACTA UNIVERSITATIS OULUENSIS
C Technica 563

JARKKO HUUSKO

COMMUNICATION PERFORMANCE PREDICTION AND LINK ADAPTATION BASED ON A STATISTICAL RADIO CHANNEL MODEL

Academic dissertation to be presented with the assent of the Doctoral Training Committee of Technology and Natural Sciences of the University of Oulu for public defence in the OP auditorium (L10), Linnanmaa, on 8 April 2016, at 12 noon

UNIVERSITY OF OULU, OULU 2016

Acta Univ. Oul. C 563, 2016

Supervised by
Professor Markku Juntti

Reviewed by
Professor Lars Kildehøj Rasmussen
Professor Leszek Szczecinski

Opponent
Professor Kimmo Kansanen

ISBN 978-952-62-1146-6 (Paperback)
ISBN 978-952-62-1147-3 (PDF)

ISSN 0355-3213 (Printed)
ISSN 1796-2226 (Online)

Cover Design
Raimo Ahonen

JUVENES PRINT
TAMPERE 2016

Huusko, Jarkko, Communication performance prediction and link adaptation based on a statistical radio channel model.
University of Oulu Graduate School; University of Oulu, Faculty of Information Technology and Electrical Engineering; Centre for Wireless Communications; Infotech Oulu
Acta Univ. Oul. C 563, 2016
University of Oulu, P.O. Box 8000, FI-90014 University of Oulu, Finland

Abstract

This thesis seeks to develop a robust semi-analytical performance prediction method for an advanced iterative receiver that processes spatially multiplexed signals that have propagated through frequency-selective receive correlated multiple-input multiple-output (MIMO) wireless communication channels. In a change of perspective, the proposed performance prediction methods are applied at the transmitter, which seeks to attain a target frame error rate (FER) either by adaptive power control or by adaptive modulation and coding (AMC).

The performance prediction scheme utilises the statistical properties of the channel – namely noise variance, number of separable propagation paths and the eigenvalues of the receive correlation matrix – to predict the signal-to-interference-plus-noise ratio (SINR) at the output of a frequency domain soft interference cancellation minimum mean square error equaliser. The SINR distribution is used to derive the distribution of the variance of the log-likelihood ratios (LLRs) at the output of a soft symbol-to-bit demapper. Mutual information transfer charts establish a bijective relationship between the variance of the LLRs and mutual information. A 3rd Generation Partnership Project compliant turbo code is assumed. Since the decoder operates independently from the channel, its extrinsic information transfer (EXIT) charts can be simulated in advance. By utilising the approximate LLR variance distribution of the demapped equaliser output, it is possible to evaluate the probability of an intersection between an equaliser chart associated with a random channel realisation and a fixed decoder chart. This probability provides the FER.

Since the proposed performance prediction method does not require any instantaneous channel state information, it can be applied at the transmitter side as a robust link adaptation scheme. In adaptive transmission power control, the modulation order and code rate are fixed. By iteratively adjusting transmission power, the transmitter attempts to find an equaliser output LLR variance distribution that reaches a specified target FER. In AMC, transmission power is fixed. The equaliser output's LLR variance distribution is determined by the modulation order, while the decoder chart's position is determined by the code rate. The transmitter iteratively adjusts the code rate and attempts to find a modulation order and code rate pairing that reaches the target FER. For vertically encoded spatially multiplexed systems, the adaptive transmission power control and AMC schemes are complemented by adaptive repeat redundancy and incremental redundancy hybrid automatic repeat request (HARQ) techniques, respectively.

Keywords: EXIT charts, HARQ, link adaptation, MIMO, performance prediction

Huusko, Jarkko, Tilastolliseen radiokanavamalliin perustuva tiedonsiirron suorituskyvyn ennustaminen ja lähetyksen mukauttaminen.
Oulun yliopiston tutkijakoulu; Oulun yliopisto, Tieto- ja sähkötekniikan tiedekunta; Centre for Wireless Communications; Infotech Oulu
Acta Univ. Oul. C 563, 2016
Oulun yliopisto, PL 8000, 90014 Oulun yliopisto

Tiivistelmä

Työn tavoitteena on kehittää luotettava semianalyyttinen suorituskyvyn ennustusmenetelmä tehokkaalle iteratiiviselle vastaanottimelle, joka käsittelee taajuusselektiivisen, vastaanotinpäässä tilakorreloituneen moniantennikanavan (multiple-input multiple-output [MIMO] channel) kautta kulkeneita tilakanavoituja signaaleja. Toisessa vaiheessa esitettyjä ennustusmenetelmiä hyödynnetään mukauttamalla lähetystehoa tai modulaatioastetta ja koodisuhdetta (adaptive modulation and coding [AMC]), samalla säilyttäen tavoitteeksi asetetun kehysvirhesuhteen (frame error rate [FER]).

Suorituskyvyn ennustusmenetelmä hyödyntää kanavan tilastollisia ominaisuuksia – kohinan varianssia, eroteltavien etenemispolkujen lukumäärää sekä vastaanottimen korrelaatiomatriisin ominaisarvoja – ennustaakseen signaali–kohina-plus-interferenssisuhteen (signal-to-interference-plus-noise ratio [SINR]) jakauman taajuustasossa toimivan, häiriötä poistavan pienimmän keskineliösumman kanavakorjaimen lähdössä. SINR-jakaumasta johdetaan pehmän symboleista biteiksi -muunnoksen jälkeisten logaritmisten bittitodennäköisyyksien suhdelukujen (log-likelihood ratio [LLR]) jakauma. Keskinäisinformaation siirroskartat perustuvat LLR:ien varianssin sekä keskinäisinformaation väliseen bijektiivisyyteen. Informaatio on kanavakoodattu 3rd Generation Partnership Project -standardin mukaisella turbokoodilla. Turbodekooderin toiminta on kanavasta riippumatonta, joten dekooderin lisäinformaation siirroskartat (extrinsic information transfer [EXIT] charts) voidaan simuloida itsenäisesti. Hyödyntämällä kanavakorjaimen lähdön pehmeiden bittipäätösten LLR:ien varianssin jakaumaa, on mahdollista arvioida millä todennäköisyydellä korjaimen satunnaisen kanavarealisaation siirroskartta leikkaa dekooderin siirroskartan. Tämä todennäköisyys voidaan tulkita kehysvirhesuhteeksi.

Koska suorituskyvyn ennustusmenetelmä ei vaadi hetkellistä tietoa kanavan tilasta, sitä voidaan hyödyntää lähetyksen mukautuksessa. Mukautuvassa tehonsäädössä modulaatio ja koodisuhde eivät muutu. Lähetin pyrkii iteratiivisella tehonsäädöllä löytämään korjaimen lähdölle LLR-jakauman, joka tuottaa halutun kehysvirhesuhteen. Mukautuvassa modulaation ja koodisuhteen valinnassa lähetysteho säilyy vakiona. Modulaatioaste vaikuttaa korjaimen lähdön LLR-jakaumaan ja koodisuhde dekooderin siirroskartan muotoon. Iteratiivisesti koodisuhdetta säätämällä lähetin pyrkii löytämään modulaation ja koodisuhteen yhdistelmän, joka saavuttaa tavoitellun kehysvirhesuhteen. Vertikaalisesti tilakanavoiduissa järjestelmissä mukautuvaa tehonsäätöä täydennetään lähetystehoa mukauttavilla uudellenlähetyksillä, kun taas mukautuvaa modulaation ja koodisuhteen valintaa täydennetään puolestaan koodisuhdetta pienentävillä automattisilla uudelleenlähetyspyynnöillä (hybrid automatic repeat request [HARQ]).

Asiasanat: EXIT-kartat, HARQ, lähetyksen mukauttaminen, MIMO, suorituskyvyn ennustaminen

Preface

The research for this work was carried out at the Centre for Wireless Communications (CWC), University of Oulu, Finland. I want to thank Professor Matti Latva-aho, Dr. Ari Pouttu and Dr. Harri Posti, who served as the directors of CWC during my stay, as well as Professor Jari Iinatti, who headed the Department of Communications Engineering.

I am grateful to my supervisor, Professor Markku Juntti, whose wide-ranging technical expertise, guidance and support have been invaluable. Professor Lars Kildehøj Rasmussen from Kungliga Tekniska Högskolan, Stockholm, Sweden, and Professor Leszek Szczecinski from Institut national de la recherche scientifique, Université du Québec, Montréal, QC, Canada, the reviewers of this thesis, provided insightful comments that helped improve the quality of the manuscript.

The bulk of the work was carried under the MIMO Techniques for 3G System and Standard Evolution (MITSE) and Cooperative MIMO Techniques for Cellular System Evolution (CoMIT) projects, both of which were managed by Lic. Tech. Visa Tapio. The funding provided by Suomen Akatemia and the project partners of MITSE and CoMIT, namely the Finnish Funding Agency for Innovation (Tekes), Nokia, Elektrobit (renamed to Bittium), Xilinx, Texas Instruments, Uninord, Renesas Mobile and Broadcom is gratefully acknowledged. I also wish to thank my former colleagues at CWC, particularly Dr. Juha Karjalainen and Lic. Tech. Juha Pyhtilä, who, along with Professor Juntti, co-authored the papers that contributed to this thesis.

Finally, I wish to thank my parents, Jorma and Heljä, other relatives and friends for their support along the way.

Symbols and abbreviations

$\otimes$	Kronecker product
$(\cdot)^{\mathrm{H}}$	complex-conjugate transpose
$(\cdot)^{\mathrm{T}}$	transpose
$\mathbf{0}_N$	$N \times 1$ vector of zeros
$\mathbf{1}_N$	$N \times 1$ vector of ones
$\mathrm{avg}\,(\cdot)$	mean value of the scalars in a vector
$\boldsymbol{b}$	$N_b \times 1$ bit vector
b	bit
$\mathcal{CN}\left(\mu, \sigma^2\right)$	complex Gaussian distribution with mean μ and variance σ^2
$\mathrm{circ}\,\{\cdot\}$	circulant matrix generator
$\mathrm{diag}\,\{\cdot\}$	diagonal matrix generator
$\mathrm{E}\,\{\cdot\}$	expected value
$\mathfrak{F}$	$K \times K$ unitary discrete Fourier transform matrix
$\mathfrak{F}_{\mathrm{T}}$	$N_{\mathrm{T}}K \times N_{\mathrm{T}}K$ block diagonal discrete Fourier transform matrix: a Kronecker product of $\mathfrak{F}$ and a $K \times K$ identity matrix
$\mathfrak{F}^{-1}$	$K \times K$ unitary inverse discrete Fourier transform matrix
$\mathfrak{F}_{\mathrm{R}}^{-1}$	$N_{\mathrm{R}}K \times N_{\mathrm{R}}K$ block diagonal inverse discrete Fourier transform matrix: a Kronecker product of $\mathfrak{F}^{-1}$ and a $K \times K$ identity matrix
f_{k_1,k_2}	coefficient of the unitary discrete Fourier matrix
$f^{\mathrm{i}}_{k_1,k_2}$	coefficient of the unitary inverse discrete Fourier matrix
$f_{\hat{\beta}}\left(\hat{\beta}\right)$	PDF of the effective SINR of a SISO/SIMO channel or a vertically encoded MIMO transmission with respect to equaliser *a priori* information value $\hat{I}_{\mathrm{a}}^{\mathrm{apr}}$
$f_{\hat{\beta}_j}\left(\hat{\beta}_j\right)$	PDF of the effective SINR for transmit antenna j in a horizontally encoded MIMO transmission with respect to equaliser *a priori* information vector $\hat{\boldsymbol{I}}_{\mathrm{a}}^{\mathrm{apr}}$
$f_{\hat{\beta}_{j,k}}\left(\hat{\beta}_{j,k}\right)$	PDF of the effective SINR for transmit antenna j at the kth frequency bin of a frequency-selective MIMO channel with respect to equaliser *a priori* information vector $\hat{\boldsymbol{I}}_{\mathrm{a}}^{\mathrm{apr}}$

$f_{\hat{\beta}'_{j,k}}\left(\hat{\beta}'_{j,k}\right)$	PDF of the effective SINR for transmit antenna j at the kth frequency bin of a frequency-selective MIMO channel with respect to equaliser *a priori* information vector $\hat{\boldsymbol{I}}_{\mathrm{a}}^{\mathrm{apr}}$ with ISI removed (interference is comprised of CAI and/or CCI)
$f_{\hat{\beta}_k}\left(\hat{\beta}_k\right)$	PDF of the effective SINR at the kth frequency bin of a frequency-selective SISO/SIMO channel with respect to equaliser *a priori* information value $\hat{I}_{\mathrm{a}}^{\mathrm{apr}}$
$f_{\hat{\sigma}_{\mathrm{a}}^2}\left(\hat{\sigma}_{\mathrm{a}}^2\right)$	PDF of the approximated post equalisation LLR variance for a SISO/SIMO channel or a vertically encoded MIMO transmission with respect to equaliser *a priori* information value $\hat{I}_{\mathrm{a}}^{\mathrm{apr}}$
$f_{\hat{\sigma}_{\mathrm{a},j}^2}\left(\hat{\sigma}_{\mathrm{a},j}^2\right)$	PDF of the approximated post equalisation LLR variance of the jth spatial stream with respect to equaliser *a priori* information vector $\hat{\boldsymbol{I}}_{\mathrm{a}}^{\mathrm{apr}}$
$\widetilde{\mathrm{FER}}$	approximate FER for a SISO/SIMO system or a vertically encoded MIMO transmission
$\widetilde{\mathrm{FER}}_j$	approximate FER of the jth spatial stream for a horizontally encoded or an MU-MIMO transmission
$\overline{\mathrm{FER}}_{\mathrm{H}}$	upper limit for the FER of the weakest stream in the AMC scheme for horizontally encoded or MU-MIMO systems
$\overline{\mathrm{FER}}_{\mathrm{L}}$	lower limit of the target FER region defined for link adaptation
$\overline{\mathrm{FER}}_{\mathrm{U}}$	upper limit of the target FER region defined for link adaptation
d	global iteration index
$\hat{g}(\cdot)$	equaliser mapping function from *a priori* to *a posteriori* information
$\tilde{g}_j(\cdot)$	decoder mapping function from *a priori* to extrinsic information for the jth spatial stream
$g_{R_{\mathrm{c}}}(\cdot)$	mapping function from LLR variance to code rate
$\boldsymbol{H}$	$N_{\mathrm{R}}K \times N_{\mathrm{T}}K$ time domain channel matrix comprised of circulant submatrices
$\boldsymbol{H}_{i,j}$	$K \times K$ circulant time domain channel matrix between transmit antenna j and receive antenna i
$h_{i,j,l}$	time domain channel coefficient of the lth propagation path between transmit antenna j and receive antenna i
$\boldsymbol{I}_K$	$K \times K$ identity matrix
$\hat{\boldsymbol{I}}_{\mathrm{a}}^{\mathrm{apo}}$	$N_{\mathrm{T}} \times 1$ vector of equaliser's *a posteriori* mutual information
$\hat{\boldsymbol{I}}_{\mathrm{a}}^{\mathrm{apr}}$	$N_{\mathrm{T}} \times 1$ vector of equaliser's *a priori* mutual information
I_{a}	mutual information value

$\hat{I}_{\mathrm{a}}^{\mathrm{apr}}$	equaliser's *a priori* information
$\hat{I}_{\mathrm{a},j}^{\mathrm{apo}}$	equaliser's *a posteriori* information for the jth spatial stream
$\hat{I}_{\mathrm{opt}}^{\mathrm{apr}}$	a specific point on the equaliser's mutual information transfer chart that is considered in link adaptation
$\tilde{I}_{\mathrm{a},j}^{\mathrm{apr}}$	decoder's *a priori* information for the jth spatial stream
$\tilde{I}_{\mathrm{a},j}^{\mathrm{ext}}$	decoder's extrinsic information for the jth spatial stream
$\tilde{I}_{\mathrm{opt}}^{\mathrm{ext}}$	a specific point on the decoder's EXIT chart that is considered in link adaptation
$\Im(\cdot)$	imaginary part
i	receive antenna index
j	transmit antenna index
$\jmath$	imaginary unit
K	length of the discrete and inverse discrete Fourier transforms
K'	number of frequency domain channel coefficients that are used by the FD-SIC-MMSE equaliser when calculating the effective SINR across the frequency spectrum
k	frequency domain index
L	number of separable propagation paths
l	propagation path index
$\boldsymbol{\mathcal{L}}$	LLR vector
$\boldsymbol{\mathcal{L}}^{\mathrm{di}}$	decoder input LLR vector
$\boldsymbol{\mathcal{L}}^{\mathrm{do}}$	decoder output LLR vector
$\boldsymbol{\mathcal{L}}^{\mathrm{ei}}$	soft bit-to-symbol mapper (indirectly equaliser) input LLR vector
$\boldsymbol{\mathcal{L}}^{\mathrm{eo}}$	soft symbol-to-bit demapper (indirectly equaliser) output LLR vector
$\mathcal{L}_n$	LLR value of the nth bit
$\mathcal{L}_n^{\mathrm{di},w,d}$	the nth decoder input LLR value for the dth global iteration of the wth transmission of a packet (in RR-HARQ)
$\mathcal{L}_n^{\mathrm{eo},u,N_d(w-u)+1}$	the nth symbol-to-bit demapper (indirectly equaliser) output LLR value from the uth version of the packet during the $(w-1)$th retransmission and after its $(N_d(w-u)+1)$th global iteration (in RR-HARQ)
$\bar{\mathcal{L}}_n^{\mathrm{eo},w,d}$	the nth symbol-to-bit demapper (indirectly equaliser) output LLR value for the dth global iteration of the wth transmission of a packet (in RR-HARQ) after deinterleaving and depuncturing
M	modulation order
M_j	modulation order of the jth spatial stream

M^{opt}	optimised modulation order for a SISO/SIMO system or a vertically encoded MIMO transmission
M_j^{opt}	optimised modulation order of the jth spatial stream in a horizontally encoded system
$\mathcal{M}$	modulation alphabet
$\mathcal{M}_j$	modulation alphabet of the symbols transmitted from the jth antenna
m	Nakagami distribution's shape parameter
N_b	number of bits
N_d	number of global (or outer) iterations
$N_{\mathcal{M}}$	modulation dependent multiplier that is used when the LLR variance is calculated from the SINR
N_{R}	number of receive antennas
N_{s}	number of symbols
N_{T}	number of transmit antennas
$N_{\text{T}}^{\text{act}}$	number of active antennas employed in adaptive transmission ($N_{\text{T}}^{\text{act}} \leq N_{\text{T}}$)
$\mathcal{N}\left(\mu, \sigma^2\right)$	real Gaussian distribution with mean μ and variance σ^2
n	bit/symbol index
$\boldsymbol{P}$	$N_{\text{T}} \times N_{\text{T}}$ transmission power matrix
$\check{\boldsymbol{P}}$	$N_{\text{T}}K \times N_{\text{T}}K$ transmission power matrix: a Kronecker product of $\boldsymbol{P}$ and a $K \times K$ identity matrix
P_j	transmission power of the jth antenna
$P_{\max}$	maximum total transmission power (normalised to 1)
$P_{\max,j}$	maximum transmission power of the jth antenna
P_{opt}	optimised total transmission power for adaptive power control
$P_{\text{opt},j}^{(N_{\text{T}}^{\text{act}})}$	optimised transmission power of the jth antenna for adaptive power control when $N_{\text{T}}^{\text{act}}$ antennas transmit data
$P_{\text{RR}}^{(w+1)}$	adapted total transmission power for the wth RR-HARQ retransmission
$P_{\text{RR},j}^{(w+1)}$	adapted transmission power for the jth antenna during the wth RR-HARQ retransmission
P_{tot}	the summed transmission power of the N_{T} antennas (normalised to 1)
$\mathcal{P}_j^{\epsilon}\left(\hat{\boldsymbol{I}}_{\text{a}}^{\text{apr}}\right)$	the probability that the equaliser and decoder graphs of the jth spatial stream intersect with a given equaliser *a priori* vector $\hat{\boldsymbol{I}}_{\text{a}}^{\text{apr}}$
$\boldsymbol{R}$	$N_{\text{R}} \times N_{\text{R}}$ receive correlation matrix

$\breve{\boldsymbol{R}}$	$N_{\mathrm{R}}K \times N_{\mathrm{R}}K$ receive correlation matrix: a Kronecker product of $\boldsymbol{R}$ and a $K \times K$ identity matrix
R_{c}	code rate
$R_{\mathrm{c}}^{\mathrm{fb}}$	optimal code rate based on receiver feedback
$R_{\mathrm{c}}^{\mathrm{IR},w}$	code rate after the $(w-1)$th IR transmission
$R_{\mathrm{c}}^{\max}$	maximum code rate
$R_{\mathrm{c}}^{\min}$	minimum (unpunctured) code rate
$R_{\mathrm{c}}^{\mathrm{opt}}$	optimal code rate for a SISO/SIMO or a vertically encoded MIMO transmission
$R_{\mathrm{c},j}$	code rate for the jth spatial stream in a horizontally encoded MIMO transmission
$R_{\mathrm{c},j}^{\mathrm{opt}}$	optimal code rate for the jth spatial stream in a horizontally encoded MIMO transmission
$\Re(\cdot)$	real part
$Q_{P_{\mathrm{opt}}}^{\min}$	minimum ratio of the power of the RR-HARQ retransmitted packets and the optimised power of the initial transmission
$Q_{R_{\mathrm{c}}^{\mathrm{opt}}}^{\min}$	minimum code rate decrease for IR-HARQ transmissions
$\boldsymbol{r}$	$N_{\mathrm{R}}K \times 1$ received signal vector
$\bar{\boldsymbol{r}}_{\mathrm{FD}}$	$N_{\mathrm{R}}K \times 1$ frequency domain residual vector after soft interference cancellation
s_0	saddle point value
t	time domain index for discrete channel realisations
$\mathrm{tr}\{\cdot\}$	trace of a matrix
w	packet transmission index
$\boldsymbol{x}$	$N_{\mathrm{T}}K \times 1$ transmitted signal vector
$\hat{\boldsymbol{x}}$	$N_{\mathrm{T}}K \times 1$ symbol estimate vector at the equaliser output
$\tilde{\boldsymbol{x}}$	$N_{\mathrm{T}}K \times 1$ symbol estimate vector constructed from the soft decoder outputs
$\boldsymbol{x}_j$	$K \times 1$ signal vector transmitted from antenna j
$\hat{\boldsymbol{x}}_j$	$K \times 1$ symbol estimate vector of the jth transmit antenna at the equaliser output
$\tilde{\boldsymbol{x}}_j$	$K \times 1$ symbol estimate vector constructed from the soft decoder outputs corresponding to the symbols transmitted from antenna j
$\dot{\boldsymbol{x}}_j$	$K \times 1$ vector containing the expected powers of the symbols transmitted from antenna j

$\ddot{\boldsymbol{x}}_j$	$K \times 1$ vector containing the expected powers of the soft symbols calculated from the soft decoder outputs corresponding to transmit antenna j
$x_{j,k}$	symbol transmitted from the jth antenna at the kth frequency bin
$\hat{x}_{j,k}$	equaliser output soft estimate of the symbol transmitted from the jth antenna at the kth frequency bin
$\tilde{x}_{j,k}$	decoder output soft estimate of the symbol transmitted from the jth antenna at the kth frequency bin (constructed from the decoder's output LLRs)
α	modulation symbol coordinate
β_j	effective SINR at the output of the FD-SIC-MMSE equaliser for the jth transmit antenna
$\hat{\beta}$	effective SINR at the output of the FD-SIC-MMSE equaliser for a SISO/SIMO channel or a vertically encoded MIMO transmission with respect to *a priori* information value $\hat{I}_{\mathrm{a}}^{\mathrm{apr}}$
$\hat{\beta}_j$	effective SINR at the output of the FD-SIC-MMSE equaliser for the jth transmit antenna with respect to *a priori* information vector $\hat{\boldsymbol{I}}_{\mathrm{a}}^{\mathrm{apr}}$
$\hat{\beta}_{j,k}$	effective SINR at the output of the FD-SIC-MMSE equaliser for the jth transmit antenna at the kth frequency bin with respect to *a priori* information vector $\hat{\boldsymbol{I}}_{\mathrm{a}}^{\mathrm{apr}}$
$\hat{\beta}'_{j,k}$	effective SINR at the output of the FD-SIC-MMSE equaliser for the jth transmit antenna at the kth frequency bin with respect to *a priori* information vector $\hat{\boldsymbol{I}}_{\mathrm{a}}^{\mathrm{apr}}$ with ISI removed (interference is comprised of CAI and/or CCI)
$\hat{\beta}_k$	effective SINR at the output of the FD-SIC-MMSE equaliser for a SISO/SIMO channel or a vertically encoded MIMO system at the kth frequency bin with respect to *a priori* information value $\hat{I}_{\mathrm{a}}^{\mathrm{apr}}$
$\Gamma(\cdot)$	gamma function
$\gamma(\cdot,\cdot)$	lower incomplete gamma function
$\boldsymbol{\Delta}$	diagonal matrix containing the symbol-wise residual interference energy after soft interference cancellation
$\hat{\boldsymbol{\Delta}}_{\mathrm{a}}$	diagonal residual interference energy matrix corresponding to stream-wise *a priori* information
$\hat{\boldsymbol{\Delta}}_{\mathrm{a},-j}$	diagonal residual interference energy matrix corresponding to stream-wise *a priori* information with the jth column and row removed

$\hat{\Delta}_{\mathrm{a}}$	residual interference energy coefficient corresponding to a particular level of *a priori* information
$\hat{\Delta}_{\mathrm{opt}}$	residual interference energy coefficient used in link adaptation
ϵ	design parameter used to ensure the openness of convergence tunnel between the equaliser and decoder mutual information transfer charts
$\tilde{\epsilon}_{1,j}$	convergence tunnel gap requirement in the LLR variance domain for the jth spatial stream for $\tilde{I}_{\mathrm{a},j}^{\mathrm{ext}} \rightarrow 1$ and ϵ (horizontally encoded MIMO transmission)
$\tilde{\epsilon}_{\mathrm{a}}$	convergence tunnel gap requirement in the LLR variance domain for $\tilde{I}_{\mathrm{a}}^{\mathrm{ext}}$ and ϵ (SISO/SIMO or vertically encoded MIMO transmission)
$\tilde{\epsilon}_{\mathrm{a},j}$	convergence tunnel gap requirement in the LLR variance domain for the jth spatial stream for $\tilde{I}_{\mathrm{a},j}^{\mathrm{ext}}$ and ϵ (horizontally encoded MIMO transmission)
$\tilde{\epsilon}_{\mathrm{opt}}$	convergence tunnel gap requirement in the LLR variance domain used in link adaptation for $\tilde{I}_{\mathrm{opt}}^{\mathrm{ext}}$ and ϵ (SISO/SIMO or vertically encoded MIMO transmission)
ζ	ratio of transmit and receive antennas when $N_{\mathrm{R}} \rightarrow \infty$
$\zeta_{N_{\mathrm{R}}}$	ratio of transmit and receive antennas when N_{R} is finite
$\boldsymbol{\eta}$	$N_{\mathrm{R}}K \times 1$ zero-mean Gaussian noise vector with covariance matrix $\sigma_{\eta}^2 \boldsymbol{I}_{N_{\mathrm{R}}K}$
$\boldsymbol{\eta}_{\mathrm{a}}$	$N_b \times 1$ zero-mean Gaussian noise vector with covariance matrix $\sigma_{\mathrm{a}}^2 \boldsymbol{I}_{N_b}$
θ	gamma-distributed sum of squared absolute values of SIMO channel coefficients at a particular frequency bin (a squared absolute value of a channel coefficient for SISO channels)
$\lambda_i^{\boldsymbol{R}}$	ith eigenvalue of a receive correlation matrix
λ_j^{W}	jth eigenvalue of a complex Wishart matrix
$\mu_{\lvert\tilde{x}\rvert^2}$	mean of the squared absolute values of soft symbol vector $\tilde{\boldsymbol{x}}$
$\boldsymbol{\xi}$	vector of the impulse response's average amplitudes
ξ_l	average amplitude of the impulse response of the lth propagation path
ρ	receive correlation coefficient
$\boldsymbol{\Sigma}_{\tilde{\boldsymbol{r}}_{\mathrm{FD}}}$	$N_{\mathrm{R}}K \times N_{\mathrm{R}}K$ covariance matrix of the frequency domain residual vector after soft interference cancellation
σ_{a}^2	LLR variance
$\sigma_{\lvert\tilde{x}\rvert^2}^2$	variance of the squared absolute values of soft symbol vector $\tilde{\boldsymbol{x}}$
σ_{η}^2	noise variance

$\hat{\sigma}_0^2$	LLR variance at the equaliser output corresponding to $\hat{I}_{\mathrm{a}}^{\mathrm{apr}} = 0$ (SISO/SIMO or vertically encoded MIMO transmission)
$\hat{\sigma}_{0,j}^2$	LLR variance at the equaliser output corresponding to $\hat{I}_{\mathrm{a},j}^{\mathrm{apr}} = 0$ for the jth spatial stream (horizontally encoded MIMO transmission)
$\hat{\sigma}_{\mathrm{a}}^2$	LLR variance at the equaliser output corresponding to $\hat{I}_{\mathrm{a}}^{\mathrm{apr}}$ (SISO/SIMO or vertically encoded MIMO transmission)
$\hat{\sigma}_{\mathrm{a},j}^2$	LLR variance at the equaliser output corresponding to $\hat{I}_{\mathrm{a},j}^{\mathrm{apr}}$ for the jth spatial stream (horizontally encoded MIMO transmission)
$\hat{\sigma}_{\mathrm{a,RR}_w}^2$	accumulated LLR variance after the wth transmission of a packet in RR-HARQ corresponding to $\hat{I}_{\mathrm{a}}^{\mathrm{apr}}$ (SISO/SIMO or vertically encoded MIMO transmission)
$\hat{\sigma}_{\mathrm{a},t}^2(t)$	LLR variance at the intersection point of the equaliser and decoder mutual information transfer charts at a discrete time instant t (SISO/SIMO or vertically encoded MIMO transmission)
$\hat{\sigma}_{\mathrm{fb}}^2$	approximation of the LLR variance at the equaliser output after the first instance of equalisation (SISO/SIMO or vertically encoded MIMO transmission)
$\hat{\sigma}_{\mathrm{fb},w}^2$	approximation of the LLR variance at the equaliser output after the first instance of equalisation for the wth transmission of the packet (SISO/SIMO or vertically encoded MIMO RR-HARQ transmission)
$\tilde{\sigma}_{1,j}^2$	decoder LLR variance corresponding to $\tilde{I}_{\mathrm{a},j}^{\mathrm{ext}} \rightarrow 1$ for the jth spatial stream (horizontally encoded MIMO transmission)
$\tilde{\sigma}_{\mathrm{a}}^2$	decoder LLR variance corresponding to $\tilde{I}_{\mathrm{a}}^{\mathrm{ext}}$ (SISO/SIMO or vertically encoded MIMO transmission)
$\tilde{\sigma}_{\mathrm{a},j}^2$	decoder LLR variance corresponding to $\tilde{I}_{\mathrm{a},j}^{\mathrm{ext}}$ for the jth spatial stream (horizontally encoded MIMO transmission)
$\tilde{\sigma}_{\mathrm{opt}}^2$	decoder LLR variance corresponding to $\tilde{I}_{\mathrm{opt}}^{\mathrm{ext}}$
$\mathbf{\Phi}$	$N_{\mathrm{R}}K \times N_{\mathrm{T}}K$ frequency domain channel matrix
$\mathbf{\Phi}_{i,j}$	$K \times K$ diagonal frequency domain channel matrix between transmit antenna j and receive antenna i
$\mathbf{\Phi}_j$	$N_{\mathrm{R}}K \times K$ frequency domain channel matrix between transmit antenna j and the N_{R} receive antennas
$\phi_{ik,k}$	frequency domain channel coefficient for the ith receive antenna at the kth frequency bin of a SISO/SIMO channel
$\mathbf{\Psi}_k$	$N_{\mathrm{R}} \times N_{\mathrm{T}}$ channel matrix at the kth frequency bin

$\boldsymbol{\Psi}_{-j,k}$	$N_{\mathrm{R}} \times (N_{\mathrm{T}} - 1)$ channel matrix at the kth frequency bin; $\boldsymbol{\Psi}_k$ with the jth column removed
$\boldsymbol{\psi}_{k,j}$	$N_{\mathrm{R}} \times 1$ vector containing the frequency domain channel coefficients between transmit antenna j and the N_{R} receive antennas at the kth frequency bin
Ω	Nakagami distribution's spread parameter

1G	1st generation
2G	2nd generation
3G	3rd generation
3GPP	3rd Generation Partnership Project
3GPP2	3rd Generation Partnership Project 2
4G	4th generation
5G	5th generation
8-PSK	octal phase-shift keying
ACK	acknowledgement
AMC	adaptive modulation and coding
AMPS	Advanced Mobile Phone Service
APP	*a posteriori* probability
ARQ	automatic repeat request
AWGN	additive white Gaussian noise
BCJR	Bahl–Cocke–Jelinek–Raviv
BER	bit error rate
BICM	bit-interleaved coded modulation
BPSK	binary phase-shift keying
CAI	co-antenna interference
CCI	co-channel interference
CDF	cumulative distribution function
CDMA	code division multiple access
CLT	central limit theorem
CP	cyclic prefix
CQI	channel quality indicator
CSI	channel state information
CSIT	channel state information at the transmitter
CSIR	channel state information at the receiver

DFT	discrete Fourier transform
DS	direct-sequence
EDGE	Enhanced Data rates for GSM Evolution
EXIT	extrinsic information transfer
FD	frequency domain
FDD	frequency division duplexing
FDMA	frequency division multiple access
FEC	forward error control
FER	frame error rate
GSM	Global System for Mobile communications
GPRS	General Packet Radio Service
HARQ	hybrid automatic repeat request
HSPA	High Speed Packet Access
IBI	inter-block interference
IDFT	inverse discrete Fourier transform
IID	independently and identically distributed
IMT-A	International Mobile Telecommunications-Advanced
IR	incremental redundancy
ISI	inter-symbol interference
ITU	International Telecommunication Union
LA	link adaptation
LDPC	low-density parity check
LLR	log-likelihood ratio
LQM	link quality metric
LUT	look-up table
LTE	Long Term Evolution
LTE-A	Long Term Evolution-Advanced
MAI	multiple access interference
MAP	maximum *a posteriori*
MC	Monte Carlo
MCS	modulation and coding scheme
ML	maximum likelihood
MGF	moment generating function
MIMO	multiple-input multiple-output
MMSE	minimum mean-square error

MSE	mean-square error
MU	multi-user
NMT	Nordic Mobile Telephone
NACK	negative acknowledgement
OFDM	orthogonal frequency-division multiplexing
OFDMA	orthogonal frequency-division multiple access
PAPR	peak-to-average power ratio
PDF	probability density function
PDP	packet drop probability
PSK	phase-shift keying
QAM	quadrature amplitude modulation
QPSK	quaternary phase-shift keying
RA	repeat–accumulate
RAN	radio access network
RR	repetition redundancy
RX	receive
SC	single carrier
SDMA	space-division multiple access
SF	space–frequency
SIC	soft interference cancellation
SIMO	single-input multiple-output
SINR	signal-to-interference-plus-noise ratio
SIR	signal-to-interference ratio
SISO	single-input single-output
SNR	signal-to-noise ratio
SU	single user
ST	space–time
TD	time domain
TDD	time division duplexing
TDMA	time division multiple access
TX	transmit
UMTS	Universal Mobile Telecommunications System
WCDMA	Wideband Code Division Multiple Access
WiMAX	Worldwide Interoperability for Microwave Access
ZF	zero-forcing

Contents

1 Introduction

The rapid development of wireless communication services has had a profound effect on the lives of billions of people. First introduced to the greater public through downlink broadcast services like radio and television, the opening of uplink communication, from the user to the network, personalises the user experience. Although the analogue 1st generation (1G) cellular communication standards were restricted to voice services, the next evolutionary step, namely the 2nd generation (2G) family of standards, was already digital and had an eye on data transfer. The 3rd generation (3G) of standards fully recognise the importance of user-wise data services. The growth of—and demand for—such services has been rapid and shows no signs of abating. Hence, the 4th generation (4G), which is starting to reach its maturity, and the 5th generation (5G), where the development of the so-called Internet of things is expected to bring a manyfold increase in the number of terminal devices, continue in the path of increasing data rates and reduced latency.

1.1 Evolution of cellular networks

The first functional mobile radio system was installed by the Detroit Police Department in 1928 [1]. In 1946, AT&T installed a mobile radio system that could connect into public switched telephone networks [2]. In decades after World War II, commercial services started to pop up in various locations over the world. Due to the congestion in the radio spectrum, in the 1960's AT&T Bell Laboratories began to develop cellular communications where the coverage area is split into smaller cells [2].

Two notable 1G cellular communication techniques were developed in the 1970's: Nordic Mobile Telephone (NMT) and Advanced Mobile Phone Service (AMPS) [3]. While the analogue 1G services gained a foothold in the 1980's, the development of digital 2G standards had already begun. In Europe, where multiple regional and incompatible 1G systems had been in use, work began on a new Pan-European standard, dubbed the Global System for Mobile communications (GSM) (initially Groupe Spécial Mobile). GSM is based on time division multiple access (TDMA) technology, where separate time slots are allocated to different users. The North American IS-95, commercially known as cdmaOne, is a direct-sequence (DS) code division multiple access (CDMA) system where the receiver distinguishes the simultaneously transmitting

users by their unique spreading sequences. GSM and IS-95 are also frequency division multiple access (FDMA) systems, since only segments of the full frequency bandwidth are assigned to different users. The date rates of GSM networks were later improved by backwards compatible enhancements, notably General Packet Radio Service (GPRS) and Enhanced Data rates for GSM Evolution (EDGE) [4].

The 1G and 2G technologies were primarily designed to support voice traffic, which has limited peak rate requirements and low toleration for latency. The growing importance of data transfer was an important consideration in the development phase of 3G systems, also known as Universal Mobile Telecommunications System (UMTS) in Europe, in the early 1990's [5, 6]. Based on the legacies of GSM and IS-95, 3rd Generation Partnership Project (3GPP) and 3rd Generation Partnership Project 2 (3GPP2) set out to develop DS-CDMA-based standards, known as Wideband Code Division Multiple Access (WCDMA) and CDMA2000, respectively. A notable advancement from the field of channel coding was incorporated into WCDMA [5, 6]: while low data rates can be served by familiar convolutional codes [7], capacity-achieving turbo codes [8] are used with high data rates. The data rates of WCDMA were further enhanced by High Speed Packet Access (HSPA) [5, 6], which allows multiple-input multiple-output (MIMO) transmission, with the involvement of multiple transmit (TX) and receive (RX) antennas, in downlink.

While MIMO was an add-on for 3G, MIMO techniques are an integral feature of 4G. Long Term Evolution (LTE) is developed by the 3GPP and thereby traces its legacy back to GSM and UMTS [9]. The Worldwide Interoperability for Microwave Access (WiMAX) forum oversees a competing family of standards. The IEEE 802.16-2005 standard [10], also known as mobile WiMAX, promises similar data rates as LTE. LTE and mobile WiMAX do not fulfil the International Mobile Telecommunications-Advanced (IMT-A) demands set by the International Telecommunication Union (ITU) for 4G. Thus, although they are marketed as 4G, they are sometimes informally referred to as 3.5G or 3.9G [5, 11]. Long Term Evolution-Advanced (LTE-A) [11] and IEEE 802.16m-2011 [12], also known as WirelessMAN-Advanced and mobile WiMAX Release 2, are referred to as "true" 4G.

The most distinctive feature of upcoming 5G networks might be their operational frequency spectrum in the millimetre-wavelength region [13, 14]. The radio spectrum between 700 MHz and 2.6 GHz is becoming congested, while the 28–38 GHz band is currently available [14]. Millimetre waves suffer a significant attenuation loss when penetrating solid obstacles, such as buildings [13, 14]. This means that in

urban environments TX energy is mostly contained within the intended cell, thereby reducing the interference in remote cells where the same frequencies are reused, which consequently allows cell size reduction. Other frequently cited potential novel 5G techniques include cloud radio access networks (RANs), device-to-device, relay and multihop communications and massive MIMO architectures [15–27]. In massive MIMO [28–31], the base station may contain more than 100 antennas that serve a much smaller number of mobile terminals. In cloud RAN architectures, cloud-computing platforms are used to collectively perform signal processing for multiple base stations. Base stations can be switched on and off based on spatio-temporal traffic fluctuations, while centralised signal processing allows joint detection and can aid in interference avoidance and cancellation [23, 27].

This section is concluded by an interesting observation [32]: Starting in 1957, the wireless transmission capacity saw an approximately millionfold increase over a 50-year period. The widening of the frequency spectrum and its division into smaller subbands were responsible for 25- and 5-fold increases, respectively, while cell size reduction lead to a 1600-fold increase. All other improvements at the physical layer brought a 5-fold increase. Thus, despite seemingly impressive advances at the physical layer, the expansion of wireless communication capacity has been mostly driven by the development and addition of hardware. Bandwidth expansion and cell size shrinkage appear to be paramount factors also for 5G networks.

1.2 Broadband MIMO communication

In order to reach the ever-increasing target data rates, wider transmission bandwidths are required. Orthogonal frequency-division multiplexing (OFDM) is becoming a key technology in the efficient exploitation of limited frequency resources. When transmitting on orthogonal parallel flat fading subchannels, inter-symbol interference (ISI) and interchannel interference are avoided [33]. In OFDM, parallel data signals are formed at the transmitter by applying the discrete Fourier transform (DFT) and at the receiver they are reconstructed back into a serial stream by applying the inverse discrete Fourier transform (IDFT) [34]. An added benefit of OFDM is that relevant channel state information (CSI) is more readily available in the frequency domain (FD) than in the time domain (TD), particularly for fast fading channels. If reasonably accurate channel state information at the transmitter (CSIT) is available, the transmitter can allocate different TX power and modulation levels to the parallel subchannels. Thus, orthogonal

frequency-division multiple access (OFDMA) has been selected for LTE and IEEE 802.16e-2015 downlink, i.e. from network to terminals.

However, OFDM is susceptible to large variations in the instantaneous TX power. These variations are characterised by the peak-to-average power ratio (PAPR) metric. A high PAPR sets stringent demands for the linearity of power amplifiers. In the average power scenario, the amplifier must significantly scale back from its maximum power [35]. For downlink this is less of an issue, but for uplink, where the terminals have limited power resources, it becomes a considerable factor. Single carrier (SC)-FDMA is in many aspects similar to OFDMA, but by performing "DFT spreading", it achieves a smaller PAPR than OFDMA. In a localised transmission mode, the transmitter allocates symbols to adjacent subcarriers before DFT spreading, while in a distributed transmission mode, equidistant subcarriers are used, with zeros inserted between them. The "unused" subcarriers can be taken up by other terminals. LTE is the first communication standard that has selected SC-FDMA [36, Chap. 4]. IEEE 802.16e-2005 selected OFDMA for both directions [10].

The diversity gain brought by the employment of multiple TX and RX antennas was first discussed in [37]. Such architectures are commonly known as MIMO systems. The addition of parallel spatial streams causes multiple access interference (MAI). When the TX antennas are co-located, the MAI is labelled as co-antenna interference (CAI). In a multi-user (MU) scenario, where independent transmitters share the same time and frequency resources, the MAI is labelled as co-channel interference (CCI). If the number of RX antennas exceeds the number of TX antennas, the receiver can cancel out the interference from parallel streams and provide diversity gain [38]. When the parallel streams belong to independent users, such strategy is known as MU-MIMO or space-division multiple access (SDMA). For MIMO channels with perfect channel state information at the receiver (CSIR), the capacity increases linearly with the minimum of the number of TX and RX antennas [39, 40].

MIMO techniques can be divided into three main classes: Space–time (ST) (or space–frequency (SF), when applied in the FD) coding seeks to exploit the potential diversity that is brought by the presence of multiple TX antennas, while in spatial multiplexing the TX antennas send independent data. Smart antennas seek to reduce interference by beamforming. Multiple alternative ST/SF coding techniques have been proposed, e.g. ST block codes [41–43], ST trellis codes [44–46] and various iterative ST coding schemes [47–55].

Spatial multiplexing schemes seek to increase the data rates by transmitting independent data across the spatial streams. In diagonally encoded spatial multiplexing [56], symbols belonging to each independent packet are transmitted across all the available TX antennas for added diversity. In vertically encoded transmission a single independently encoded data packet is transmitted across all the available antennas, while in horizontally encoded transmission each antenna transmits its own independently encoded packet [57]. Since the receiver does not know or care of the physical locations of the TX antennas, the horizontally encoded spatial multiplexing scheme is similar to MU-MIMO, where the transmitting streams originate from different locations. The transmitter must make a fundamental trade-off in how it chooses to exploit the potential diversity and multiplexing gains brought by the spatial degrees of freedom [58]. It was concluded in [59] that modern communication systems, such as the LTE, favour multiplexing over diversity. For low-mobility users, link adaptation (LA) and scheduling make TX diversity redundant, while high-mobility users already benefit from time or frequency diversity, which reduces their demand for TX diversity.

Beamforming can reduce interference, thereby producing array (or antenna) gain, but requires accurate CSI [60–62]. CSIR can usually be inferred reasonably accurately from pilot signals, but accurate CSIT is harder to obtain. In time division duplexing (TDD), the terminal and base station transmit on the same frequency band but at different time slots. If the channel remains relatively static between time slots, the CSIT can be inferred directly from the CSIR. However, the powers of the transmitted and received signals can vary by as much as 100 dB. Therefore, most commercial mobile radio standards employ frequency division duplexing (FDD) [63, Sect. 4.1], where the forward and backward transmissions take place at different frequency bands. With FDD, the transmitter must rely on feedback provided by the intended receiver. The feedback loop causes delay, which makes the CSI more sensitive to rapid channel changes. Furthermore, for the CSI to be accurate, detailed feedback is required. The signalling overhead of control channels directly reduces the capacities of genuine communication channels. Unlike beamforming, a trade-off between spatial diversity and multiplexing modes is an option even with limited CSI.

Other key features of modern telecommunication standards, such as iterative coding and receiver processing, LA and hybrid automatic repeat request (HARQ) techniques are discussed in Sects. 2.1, 2.4 and 2.5, respectively.

1.3 Aims and outline of the thesis

The main contribution of this thesis is the development of a robust performance prediction technique for an advanced iterative receiver. In the second part, the performance prediction method serves as a basis for iterative LA algorithms.

The reason why many recent (and sometimes old!) advances in signal processing have become implementable is due to the vast improvements in computing capacity. While increased complexity enables higher data rates, it also makes it more difficult to predict or analytically evaluate the system performance. Therefore, exhaustive Monte Carlo (MC) computer simulations, where every operational block is modelled in full detail, are required. The adoption of iterative receivers and decoders multiply the number of computations. Hence, such simulations are often time-consuming. Analytical performance prediction is usually restricted to linear receivers and only occasionally takes into account forward error control (FEC) channel coding. Even then, capacity-achieving codes are rarely considered.

This thesis seeks to develop a flexible performance prediction scheme for an efficient, iterative MIMO minimum mean-square error (MMSE) receiver, which employs a 3GPP compliant turbo decoder [64] and backward error control in the form of the repetition redundancy (RR)-HARQ protocol [65, 66][1] to detect data arriving through an SC-FDMA uplink channel. The prediction scheme can take into account different channel dimensions, RX correlation, multipath profiles (by considering the number of separable channels taps), modulations, code rates and alternative spatial multiplexing techniques (vertically and horizontally encoded transmission). Although only turbo coding is considered here, the same semi-analytical performance prediction procedure would be applied with different FEC methods, such as convolutional, low-density parity check (LDPC) and repeat–accumulate (RA) codes without any major modifications. In general, channel codes that can be represented by factor graphs and decoded by belief propagation algorithms would be good candidates.

LA is dependent on the availability of CSIT. Accurate CSIT is particularly difficult to obtain for fast fading channels and with FDD-systems. Consequently, there are previous LA proposals that have considered inaccurate or quantised CSIT. Hence,

[1] Bit probability combining in conjunction with repetition coding across automatic repeat request (ARQ) transmissions was first proposed in [65]. The combining technique is often referred to as Chase combining after a subsequent paper [66], where repetition coding across ARQ transmissions with maximum likelihood (ML) sequence decoding was examined. Following the nomenclature in [67], the abbreviation RR shall be used hereafter.

in order to create a separation to existing literature, the secondary goal of this thesis is to develop robust LA schemes that rely on minimal CSIT. Noise variance, the number of separable propagation paths and eigenvalues of the RX correlation matrix provide sufficient information. TX power control and adaptive modulation and coding (AMC) schemes are developed for both considered spatial multiplexing techniques. The AMC schemes adhere to the recommendation given in [68] that equalisation and the modulation and coding scheme (MCS) selection should be viewed within a unified framework, from an information theoretic perspective, when seeking to optimally exploit the capacity of a time-varying fading channel. The vertically encoded TX power control and AMC schemes are complemented by adaptive RR-HARQ and incremental redundancy (IR)-HARQ [69] schemes.

Most of the results presented in this thesis have been presented in peer-reviewed conferences and in a journal paper. For the sake of clarity and coherence, the thesis has been written as a monograph.

Chap. 2 contains a literature review of previous and parallel work that relates to the contributions of this thesis. Iterative decoding and receiver processing and the convergence analysis of such techniques are central aspects, as is statistical performance analysis. An overview of LA and HARQ techniques conclude the literature review.

The system model that is used throughout the thesis is featured in Chap. 3. A frequency-selective MIMO channel model is described and an iterative FD soft interference cancellation (SIC) MMSE equaliser is presented.

The core contribution of this thesis is found in Chap. 4. Its results were published in [70–73]. Firstly, mutual information transfer charts are used to semi-analytically track the convergence of the FD-SIC-MMSE equaliser that operates in conjunction with a standard 3GPP turbo decoder. Then the properties of statistical single-input single-output (SISO), single-input multiple-output (SIMO), as well as RX correlated MIMO channel models are used to derive the effective signal-to-interference-plus-noise ratio (SINR) at the output of the considered equaliser/demapper. The log-likelihood ratio (LLR) variance distribution can be derived from the effective SINR distribution. The LLR variance distribution proves to be very useful, since it can be used to predict frame error rates (FERs) of SISO/SIMO and vertically and horizontally encoded MIMO systems. Three levels of phase-shift keying (PSK) are considered, namely binary phase-shift keying (BPSK), quaternary phase-shift keying (QPSK) and octal phase-shift

keying (8-PSK).[2] For SISO/SIMO and vertically encoded MIMO, the predictions are complemented by RR-HARQ.

Chap. 5, whose partial results were published [74], features iterative LA algorithms that utilise the described performance prediction method. TX power control and AMC schemes are developed for vertically and horizontally encoded MIMO systems. The adaptive RR-HARQ and IR-HARQ schemes utilise feedback that reflects the level of mutual information at the receiver.

The main findings of the thesis are summarised in Chap. 6. In addition, some open questions and potential future research topics are discussed.

1.4 Author's contribution to publications

The thesis is based on four conference papers [70–72, 74] and one journal paper [73]. The author played the main role in developing the ideas, producing the results and writing the papers.

The idea of extrinsic information transfer (EXIT)-chart-based LA for HARQ transmissions was proposed by Dr. Juha Karjalainen, who was the second author in [70, 71]. The formula for the asymptotic SINR in [72, 73] (and Appendix 4 in this thesis), which was later applied in the iterative TX power control schemes in [74], was derived by Lic. Tech. Juha Pyhtilä, who was the second author in the cited papers. Prof. Markku Juntti (the third author in [70–74]) provided guidance and comments during the preparation of the papers.

The simulation model used in [70–74] was based on a model created by Dr. Karjalainen. The simulations utilised a channel generator developed by Dr. Esa Kunnari. The turbo encoding and decoding software, and the 3GPP rate matching software, were from the Coded Modulation Library.[3] The performance prediction and LA software were developed solely by the author of this thesis.

[2] Modern wireless standards apply different degrees of quadrature amplitude modulation (QAM) for band efficient communications. They are omitted here due to the non-Gaussian distribution of the demapped LLRs, which interferes with the proposed semi-analytical framework. This issue is further discussed in Sect. 4.1.

[3] The Coded Modulation Library is distributed under the GNU Lesser General Public License. For more information, refer to: `http://www.iterativesolutions.com/`

2 Review of earlier and parallel work

This chapter reviews relevant prior and parallel published work. Sect. 2.1 discusses the evolution and proliferation of iterative receiver processing, which followed the introduction of turbo codes. Sect. 2.2 reviews techniques that have been developed to analyse the convergence of iterative receiver algorithms. Sect. 2.3 is dedicated to various efforts that have sought to explain how the properties of statistical radio channel models can be used to analyse the receiver performance. The MIMO channels' spatial dimension can be considered in LA, as can be witnessed in Sect. 2.4. Finally, recent work related to HARQ techniques is reviewed in Sect. 2.5.

2.1 Iterative decoding and receiver processing

After Shannon derived formulae for the capacities of communication channels [75], much of the ensuing work in the field of telecommunications has focused on developing techniques that could exploit the capacity. One fundamental aspect in that pursuit has been the development of FEC methods that introduce redundancy to the transmitted data. The receiver can exploit the redundancy and recover the original data even when the channel partially corrupts the packet.

One of the landmark moments in the field of coding theory was the introduction of turbo codes [8]. In the classical turbo decoding set-up, two parallel soft-input soft-output decoders, which are separated by an interleaver and a corresponding deinterleaver, process recursive systematic convolutional codes. Traditionally, convolutional codes are decoded by the Viterbi algorithm [76, 77], which performs ML sequence detection. In turbo decoding, the constituent decoders utilise a modified Bahl–Cocke–Jelinek–Raviv (BCJR)-algorithm [78], which outputs bit-wise *a posteriori* probabilities (APPs). After the bit-wise *a priori* values are subtracted from the *a posteriori* values, the newly obtained bit-wise extrinsic information values become *a priori* information for the following constituent decoder. By using logarithmic values, the multiplications of the BCJR-algorithm become additions [79, 80]. Even in the log-domain, the maximum *a posteriori* (MAP) implementation of the BCJR-algorithm involves a complex logarithmic summation of exponentials. Descriptions of different alternative implementations, including the most commonly used optimal log-MAP and sub-optimal max-log-MAP solutions [79, 80], can be found in [81].

Many papers have sought to explain the efficacy of turbo codes and iterative decoding techniques in general. In work specifically related to turbo codes, a phenomenon dubbed "spectral thinning" was observed: an increase in the interleaver length reduces the number of possible code words with low Hamming weights, thereby reducing the number of code words that are close to each other bit-wise [82, 83]. The steepness of the "turbo cliff", the region where the FER drops rapidly, is largely attributed to the interleaving gain, but the code's distance spectrum properties influence the level of the FER floor [82–84].

It was soon noted that the fundamental concepts behind the efficacy of turbo codes have many other applications besides the decoding of parallel concatenated codes [85]. Bit-interleaved coded modulation (BICM) provides an example of interleaving gain in a different scenario: when a bit level interleaver is added between a convolutional encoder and a serially concatenated bit-to-symbol mapper, diversity within the encoded bit sequence is increased, which in turn improves the coding gain [86, 87]. This is a significant departure from the original concept of coded modulation, where channel coding and modulation, and demodulation and decoding, are intrinsically linked [88]. Naturally, a turbo code can be used as the constituent code in a BICM scheme [89].

Iterative decoding has been expanded beyond convolutional codes and parallel concatenation. Design criteria for serially concatenated block and convolutional codes were developed in [90]. The emergence of turbo codes also resurrected the interest in LDPC codes [91] (and a proposed decoding structure [92]), when simulations showed that their performance was close to the Shannon capacity [93]. The capacity of LDPC codes was further studied in [94]. Based on this work, LDPC codes that exceeded the performance of turbo codes were developed [95–97]. Another class of iterative codes, the so-called RA codes, were presented in [98, 99]. The iterative decoding process can be viewed as an instance of belief propagation [100], where the extrinsic messages exchanged between the component decoders express their belief about a certain bit in the form of an LLR. The iterative decoding algorithms can be divided into two families: min-sum algorithms (e.g. the Viterbi algorithm and the soft output Viterbi algorithm [101, 102]) and sum-product algorithms (e.g. the BCJR algorithm) [103, 104].

The concept of iterative processing is not restricted to decoding. One of the first examples where the iterative loop was expanded to the entire receiver was iterative equalisation [105], where soft information from the decoder was used in SIC. Iterative equalisation has since attracted further attention, in one form or another, e.g. [106–123]. Some measure of the benefit of iterative equalisation is given by the observation that the

bit error rate (BER) performance of an iterative equaliser–decoder pairing converges to that of an additive white Gaussian noise (AWGN) channel at high signal-to-noise ratios (SNRs) when BPSK is assumed, which indicates successful ISI removal [116].

2.2 Convergence analysis of iterative decoding and equalisation

Much effort has been spent on studying the convergence of iterative decoders. Geometric analyses, such as [124–130], seek to characterise the behaviour of iterative decoding algorithms by finding fixed (or stationary) points in the belief propagation [100] interpretation of the iterative decoding process. However, the existence of fixed points does not explicitly indicate whether an iterative decoder will converge or not [131]. Furthermore, such deterministic methods are computationally complex, which makes them impractical for turbo decoder performance prediction [132].

Stochastic analysis methods, which are concerned with the statistical properties of the inputs and outputs of iterative blocks, have proven to be more popular. They generally assume infinite codeword lengths and perfectly random interleavers. An important requirement is the so-called consistency (or symmetry) condition [94], which states that for bit-sign-wise symmetric input distributions, the channel's and component decoders' bit-sign-wise output distributions should also be symmetric. Thereby, their performance is independent of the particular processed codeword. It was discovered in [133] that after a few iterations, the output distributions of sum-product algorithms, such as the BCJR algorithm, closely resemble the Gaussian distribution. This observation has proven to be useful for the stochastic analysis methods. In [134–136], the input and extrinsic output SNR distributions were observed. Transfer characteristic bands that could take into account finite-length code words were introduced in [136]. In [137], measurements of the correlation between actual bit values and their soft estimates were used as a convergence metric. EXIT charts [138] have become the most widely used method to track the convergence of iterative decoders or receivers. They are the method of choice also in this thesis. EXIT charts assume that the mean-to-variance ratio of the bit-sign-wise Gaussian distributed LLRs is $1/2$. Under this assumption, the SNR of Gaussian distributed LLRs becomes half of their mean [139], which makes the two measures, i.e. the mean and SNR, equivalent. EXIT charts only map the measure to the mutual information domain. However, the approximation that the mean-to-variance ratio would be $1/2$ is not entirely accurate. Therefore, in an alternative approach [132], distinct parameters were designated for the mean and variance.

The decoder EXIT chart is obtained by MC simulations, where inputs corresponding to a certain level of *a priori* information are fed into the decoder and the level of extrinsic information is measured from the output. The equaliser chart, or the chart of a similar front end receiver block, can be formed in a similar manner, as was done in [107–112, 140, 141]. If the chart of the front end receiver block is approximately linear, the intermediate points can be interpolated by only considering the extreme cases with no *a priori* and full *a priori* information [113]. Each unique channel realisation has its own transfer chart, which makes the measurement-based approach somewhat impractical. For certain front end receiver blocks, the EXIT chart can be determined analytically for a known channel realisation [114, 115, 120, 142, 143]. These studies serve as important precursors for the work carried out in this thesis.

The majority of the papers that utilise EXIT charts or alternative stochastic analysis methods to study the performance of iterative receivers assume convolutional codes, e.g. [107–117, 140–146]. Although the transmitter–receiver structure featured in this thesis uses turbo codes in channel coding, the convergence analysis largely follows the same outlines as the analyses that feature convolutional codes. In [147], EXIT charts were used to track the convergence of an iterative BICM receiver with a turbo code as the constituent code, while an RA code was assumed in [148, 149].

The prevalence of EXIT charts does not mean that alternative convergence tracking methods would not have been used. In [150], mean-square error (MSE) charts were used to examine LDPC codes, while BER transfer charts and the SNR variance evolution method were used to analyse the performance of iterative equalisers in [113, 122] and [115], respectively. In addition to BER transfer charts, EXIT charts were also used in [113], while in [122], empirically formed LDPC decoder BER transfer curves could take into account finite block lengths. In [116], the convergence was tracked by observing the ratio between the channel noise variance and variances of the input/output distributions of a MAP equaliser and a convolutional decoder. In [151], inspired by [132], the convergence of an iterative MIMO receiver that included a turbo decoder was examined by using large look-up tables (LUTs), which contained mean and variance pairings for the information and parity bit LLRs. This was done as EXIT charts proved to be inaccurate for the considered receiver.

2.3 Statistical performance analysis

This section focuses on work that has sought to develop an understanding on how the statistical properties of propagation channels influence the output distributions of receiver filters. The earliest analytical results that provided insight into the output distribution of an MMSE filter were presented in [152]. It was shown that the interference at the output of an MMSE MU detector, which is comprised of MAI and noise, was in many cases approximately Gaussian. It was later proved that the distributions of output MAI [153], signal-to-interference ratio (SIR) [154] and decision statistics [155] of an MMSE receiver in an uplink DS-CDMA channel are asymptotically Gaussian. The asymptotic distributions aptly describe the behaviour of DS-CDMA systems, which employ long spreading sequences and accommodate large numbers of users. Thus, the results from random matrix theory, which generally assumes infinite matrix dimensions but a finite ratio of dimensions, are particularly attractive. However, it was noted already in [154] that for small SIR and a spreading length of 16, the Gaussian approximation is inaccurate for the tails of the genuine SIR distribution. By applying this into MIMO channels, the spreading length corresponds to the number of RX antennas, while the number of users corresponds to the number of TX antennas. "Regular" MIMO channel matrices have much smaller dimensions than DS-CDMA systems, which means that the MMSE filter's output distributions rarely exhibit asymptotic Gaussian behaviour. In the TDD-based massive MIMO [28–31], the base station may have more than 100 antennas that serve a much smaller number of mobile terminals. At this stage, massive MIMO is an emerging concept. Therefore, this thesis shall only consider established MIMO architectures with moderate spatial dimensions.

One early paper which sought to develop a probability density function (PDF) for the distribution of the SINR at the output of an MMSE filter was [156]. It considered a MIMO channel with two TX antennas, and a successive interference cancellation MMSE filter. In [157], the gamma and generalised gamma distributions were used as approximations of the genuine SINR distribution for a MIMO channel. This was accomplished by finding the first three asymptotic moments of the distribution and then defining a (generalised) gamma function with matching moments. The paper also provided BER approximations that needed to be evaluated numerically. In [158], the results of [157] were generalised to allow receive RX correlation. The same paper provided closed form solutions for the BER approximations. The gamma-distribution-based approximation found further use in [159], where it was used to estimate the

BERs of M-ary QAM schemes in TX correlated Rayleigh flat fading channels. The gamma distribution was again used in [160] to approximate the post-detection MIMO MMSE SINR in *ad hoc* networks. There have also been alternative SINR distribution approximations. In [161], MMSE SINR distributions for small-dimensional channel matrices were developed, while in [162] the same methodology was expanded for TX correlated channels. The Gaussian distribution was suggested as a suitable approximation in [163, 164]. Papers comparing the asymptotic performance of MMSE and zero-forcing (ZF) receivers in MIMO channels have also been published [165, 166].

Most of the contributions listed above consider asymptotic behaviour or try to find well-known distributions that would resemble the actual SINR distribution at the output of an MMSE filter. Particularly, for configurations with a limited number of RX antennas, the gamma and Gaussian distributions fail to match the tails of the genuine SINR distribution. A far more accurate distribution was proposed in [167]. This particular approximation does not attempt to match the SINR distribution with any well-known distribution. When generalisations are avoided, the distribution's tails can be accurately approximated even for a 2×2 antenna set-up. This robust approximation will later form the cornerstone of the performance prediction method developed in Chap. 4. It is also general for any antenna configuration, unlike the method in [161, 162]. In addition, [167] develops the SINR PDF for ZF receivers.

There have been other noteworthy contributions that are not applicable to this thesis' problem setting due to some inherent assumptions or restrictions. Nevertheless, they provide some interesting insights into statistical performance evaluation and deserve to be brought up. In [168], MMSE-filtered SINR distributions were derived for linearly precoded single user (SU) and MU-MIMO systems in a 3GPP LTE downlink. Often, the consideration is restricted to SISO channels. A PDF of the extrinsic information at the output of an SIC-MMSE equaliser was formed in [118]. However, the equaliser still required some simulations before the expectation-maximisation algorithm could be used to determine the proper mixture of Gaussian distributions contributing to the PDF of the extrinsic information. Knowledge of this distribution was then used in the design of LDPC codes. In [169], cumulative distribution functions (CDFs) were developed for the output SINRs of linear FD-MMSE and FD-ZF equalisers that processed QPSK symbols that had propagated through frequency-selective SISO channels. The CDFs were then used to approximate the equalisers' output BERs. An approximated distribution of the Euclidean distance between transmitted and estimated BPSK sequences at the output of a multipath SISO channel was derived in [123]. The distribution was subsequently used

to develop an upper bound for the FER of an ML receiver, which contained an iterative equaliser. Some papers have assumed practical channel codes. A semi-analytical study of the impact of channel estimation errors on the BER of a turbo decoder was conducted in [170]. In [171, 172], cumulant generating functions of the LLRs of BICM and BPSK schemes, respectively, in flat fading SISO channels were formed. The cumulant generating functions were used to form BER bounds for convolutional and RA codes. A similar approach was taken in [173], where approximate LLR PDFs for Gray-mapped QAM BICM schemes were developed. The PDFs were subsequently used to calculate the BICM capacity and develop BER bounds for convolutional codes.

2.4 Link adaptation for MIMO channels

LA requires CSIT. If TDD is employed and the channel remains relatively static between the TX and RX modes, the transmitter can infer the CSI from the packets itself received. With FDD, which is more commonly used than TDD, the transmitter must rely on feedback provided by the intended receiver.

Receiver feedback, where the receiver supplies the transmitter with CSI, which the transmitter then uses in LA, was first proposed in [174]. Classically, the transmitter can adapt its power and/or rate [175], but the introduction of MIMO also allows spatial LA. The value of feedback depends on the system scenario, but feedback is usually most beneficial when the transmitter can compensate for some disturbance induced by the channel, e.g. ISI, MAI/CCI/CAI, etc. [176]. MIMO systems are particularly problematic for LA schemes that require accurate, coefficient-wise CSIT. The feedback requirement grows with the product of the TX antennas, RX antennas, delay spread and the number of users, while the capacity only grows linearly [177]. However, even a few feedback bits can often improve the performance close to an optimal scenario with perfect CSIT [176, 177].

The feedback can relate either to instantaneous or statistical CSI. LA schemes relying on statistical feedback will suffer a performance loss compared to systems that rely on instantaneous CSI, but fast LA schemes also require large signalling overheads [176, 178]. Hence, in addition to slow fading channels, statistical CSI feedback may also be useful for channels where the low-rate feedback cannot keep up with rapid channel fluctuations [177]. The iterative decoding of the powerful capacity-approaching iterative codes discussed in Sect. 2.1 increases the feedback delay. If outdated or inaccurate CSIT is used, it is possible that the current channel is in

outage, i.e. its capacity does not support the intended TX rate. The impact of imperfect (assuming only statistical knowledge) and erroneous CSIT on AMC has been studied in [179–187]. It was discovered in [181] that the considered beamforming[4] and adaptive modulation scheme became more resistant to imperfect CSIT as the number of antennas, particularly the number of RX antennas, increased. Adaptive spatial multiplexing schemes, which are of interest in this thesis, are more sensitive to imperfect CSIT than beamforming schemes [186].

In AMC, an optimal MCS is picked to match the channel conditions. AMC can be performed without exact knowledge of the channel coefficients. A channel quality indicator (CQI), or a link quality metric (LQM), to use an alternative term, is still needed. Regardless of their formal definitions, CQIs/LQMs are usually, in one way or another, linked to the effective SNR/SINR measured at the detector output. Different effective SNR/SINR metrics for time and frequency-selective channels have been proposed [188–190]. Mutual information metrics can be approximated from the soft demapped bit-wise LLRs [191, 192]. The uncoded BER is often obtained by applying the Q-function, which can be used to obtain the modulation-wise symbol error probabilities for non-binary modulations in an AWGN channel [193, Sect. 5.2]. LA schemes require a target; BER and FER are the most commonly used, while constant rate is also a possibility. There are approximate decoding-algorithm-dependent ways to map the uncoded BER into coded BER and/or FER, e.g. for convolutional codes [194] and LDPC codes [195]. Channel capacity has also been used as a CQI/LQM, in which case a constant outage capacity becomes a natural target for LA.

From a practical point of view, transmission rate adaptation schemes should always take into account channel coding. Nevertheless, several early and/or theoretical TX rate adaptation studies have assumed uncoded systems [179–187, 196–205], while more practical studies assume some form of channel coding. In [206], adaptively punctured convolutional codes were considered with a fixed modulation (BPSK). Convolutional codes [190, 192, 194, 195, 207–216] are also the most popular option in AMC, while trellis-coded modulation [217–222], turbo codes [223] and LDPC codes [195, 224] have also been considered. Rate adaptation can be combined with adaptive TX power control [197, 205, 225–228], but the spectral efficiency suffers relatively little if either TX power or transmission rate remains constant [203].

[4]Beamforming and precoding are fundamental concepts in MIMO LA. They require coefficient-wise CSIT and thereby fall outside the scope of this thesis.

In addition to MCS selection, CSIT can be exploited in many different scenarios. It can be used to determine the number of active spatial streams [212, 229], or to choose between diversity and spatial multiplexing modes or their hybrid [230, 231], between beamforming and spatial multiplexing modes [191, 232], or between SU and MU modes [233]. An important aspect is how the transmitter selects the appropriate TX mode. It can use an LUT, which contains the CQI/LQM switching thresholds between different TX modes. The thresholds can be obtained through simulations or measurements [178], machine learning [214, 234, 235] or channel sounding [216]. In some cases, the transmitter can semi-analytically determine the value of the target parameter that results from a particular MCS. The transmitter then selects the MCS that attains the predefined target and offers the best spectral efficiency.

Services that require low and constant data rates prioritise energy efficiency over spectral efficiency. In addition to TX power consumption, devices want to minimise circuit power consumption. Battery life in general is an important factor for mobile terminals. The energy efficiency aspect has been considered in LA [236, 237]. Adaptive TX power control also helps reduce the level of interference experienced by other users.

LA schemes that assume iterative receivers often use EXIT charts in the analysis. Due to the receiver set-up considered in this thesis, such schemes are of particular interest. If the transmitter knows the channel coefficients, the analytically calculated detector transfer chart can be used as a basis of transmission optimisation. Such an approach is known as curve-fitting and has been used in code design [238–242], in code rate adaptation [243], in MCS selection for multilevel BICM-MIMO schemes [144, 145] and in TX power optimisation [148]. Adaptive MCS selection in an SC-FDMA uplink with iterative MMSE receivers was studied in [244, 245]. Both proposals utilised the effective SINR at output of the MMSE filter in LA. As has been noted in this section and in Sect. 2.2, the effective SNR/SINR and mutual information are closely related. In [244], hard decision successive interference cancellation was assumed, while in [245], the performance prediction method from [143] was utilised along with turbo codes.

2.5 Hybrid ARQ techniques

A combination of FEC and ARQ, first explored in [246, 247], is labelled as HARQ. The purpose of HARQ techniques is to introduce backward error control into communication systems. The inclusion of HARQ is beneficial, particularly when the transmitter cannot fully exploit instantaneous channel capacity [248]. Stop-and-wait ARQ, where the

transmitter waits for an acknowledgement (ACK) or a negative acknowledgement (NACK) message before any further transmissions, is assumed throughout this thesis.

When MIMO channels are complemented by HARQ techniques, the diversity–multiplexing trade-off from [58] gains a third dimension: delay. Even in the worst-case scenario, in terms of diversity, where the channel remains quasi-static for the ARQ retransmissions, the system exhibits a diversity gain [249]. The diversity–multiplexing–delay trade-off was further studied in the case of delay-sensitive systems [250] and block fading[5] MIMO channels [251]. With high transmission rates or low TX powers, the instantaneous channel may be in outage, but subsequent HARQ transmissions allow the capacity to be used more efficiently at the cost of delay. Even so, there is still plenty of room for improvement: the throughputs attained by contemporary HARQ techniques fall well short of the ergodic capacity in the high rate regime [67]. Thus, the HARQ schemes brought up in this thesis should not be viewed as fully matured technological advances. One way to slightly bridge the capacity gap is to utilise CSIT to control the TX power and rate. Such a system attains higher multiplexing and diversity gains than a system with fixed TX power and rate that merely relies on packet retransmissions [228]. This motivates the development of adaptive HARQ schemes that complement LA schemes in partial CSIT situations. Most communication systems oversee the packet transmissions through ACK and NACK messages, depending on whether the packet was successfully recovered or not. Hence, if additional bits are allocated to ARQ messages, CSIT can be updated through the data link layer [176].

Two distinct HARQ schemes are considered in this thesis, namely RR-HARQ [65, 66] and IR-HARQ [69]. In RR-HARQ, the receiver accumulates SINR[6], while in IR-HARQ, it accumulates mutual information [252]. There is extensive literature that deals with ARQ and the so-called type-I HARQ, sometimes referred to as generalised slotted Aloha, where the receiver discards erroneously decoded packets once the ARQ is sent, e.g. [208, 252–262]. However, such schemes fall outside the scope of this thesis.

In RR-HARQ, versions of the same packet that were transmitted in different time slots are combined at the receiver. A simple way to perform RR is by summing the bit-wise LLRs from the different packets at the input of the decoder. With iterative

[5] A block fading channel is assumed to be quasi-static for the duration of a transmitted block, but temporally uncorrelated between successive blocks.

[6] An example of SNR (the considered system model does not induce interference at the receiver) accumulation can be found in [215]. A very close approximation of the throughput performance of a convolutionally encoded RR-HARQ system was obtained simply by inserting a sum of the transmission-wise SNRs into an SNR-to-FER mapping function.

receivers, more advanced forms of combining become possible. In [263, 264], a turbo decoder was utilised in iterative equalisation of interleaved versions of the original packet. An integrated iterative equalisation architecture, which utilised the modified BCJR-algorithm, was proposed in [265]. The "integration" takes place during the calculation of the BCJR-algorithm's transition probabilities, which are obtained by recursively considering the transmission-wise soft symbol probabilities. Along the same lines, computationally less intensive combining schemes involving MMSE equalisers were proposed in [117, 266]. Reliability-based HARQ provides a slight twist to the retransmission principle. The receiver uses the LLRs to identify symbols that were severely corrupted by the channel. If the original packet has not been recovered, the receiver sends an ARQ that specifies the symbols it would like to receive again. Reliability-based HARQ uses the transmission resources more efficiently than regular RR-HARQ, but requires more feedback to specify the symbols that are desired for retransmission [267]. Another way to reduce the sizes of the HARQ packets in an environment that induces burst errors is to transmit several independently decodable subpackets within a single transmission resource block [268].

If a NACK is received, IR-HARQ schemes aid the receiver by transmitting additional coded bits or symbols.[7] IR-HARQ outperforms RR-HARQ in terms of throughput, particularly when the initial code rate is high [252, 269, 270]. This can be traced back to the improved coding gain, but comes at the cost of larger RX buffers [269]. An IR-HARQ scheme, with an infinite number of possible IR transmission slots, can with a finite average delay attain the same maximum throughput as a pure FEC system that relies on infinite delay to deliver the codeword [252]. The IR transmissions often contain coded bits or symbols that were initially punctured, e.g. convolutional [271] and turbo [272] codes, but the IR packets themselves can be independently decodable, while still aiding the decoding of the initial packet, if necessary, e.g. [273, 274].

The turbo principle lends itself also to IR-HARQ: In [275], the original information bit sequence was passed through an interleaver before being turbo-encoded for IR transmissions. For each IR transmission, the "cumulative" bit-wise LLRs from the previous transmission(s) were used as *a priori* information. In [276], the initial packet was encoded by a recursive systematic convolutional code, a type of code used as

[7] RR can be viewed as a special case of IR. It is also possible that an HARQ transmission contains a mixture of previously transmitted and punctured coded bits or symbols, particularly when a constant packet size is desired. Within this thesis, IR refers to the case where the HARQ transmissions only contain coded bits or symbols that have not yet been transmitted. Therefore, the two considered HARQ modes are distinctly different.

constituent codes in turbo coding. If the initial transmission, which was decoded by a modified BCJR-algorithm, was unsuccessful, the first IR transmission contained a parity bit sequence obtained by encoding an interleaved version of the data sequence. Hence, after the first IR transmission, the standard turbo decoder could be employed. Subsequent transmissions, if necessary, were RR retransmissions and in turn contained the information bit sequence and the two parity bit sequences.

There are two main ways to determine the sizes of the IR packets: rate allocation (or assignment) and rate adaptation. In rate allocation, the rates of the IR transmissions follow a predefined pattern and are determined by the transmission index. Rate allocation is suitable for the case where only a single feedback bit is allocated for the ACK/NACK-message. Various code rate allocation methods for truncated IR-HARQ, where the number of IR transmissions is finite, have been proposed: In [277], the error probability only depended on the number of available non-punctured bits at the decoder. Rate allocation strategies for quasi-static and block fading channels can be found from [278, 279] and [280, 281], respectively. In quasi-static channels, where the future channel coefficients are known in advance, rate allocation can be complemented by power allocation [278, 279] under average power constraint. In a quasi-static scenario, an optimised IR-HARQ scheme can attain the same average throughput as an LA scheme that utilises quantised CSI feedback [279].

Rate adaptation utilises multi-bit feedback to deliver a metric of the accumulated mutual information to the transmitter, which utilises the metric to optimise the rates of the IR transmissions. Examples of this approach can be found in [280–282]. For block fading channels, the feedback metric can be interpreted as fully outdated CSI [280]. In performance evaluations of comparable rate allocation and rate adaptation schemes [280, 281], the latter offered superior throughput.

Concentrating on block fading channels, there is common ground between RR-HARQ and rate allocation IR-HARQ in a transmission optimisation sense. When the rates of the HARQ transmissions are fixed, TX power optimisation becomes a convenient research problem. Various channel models, CSIT assumptions and alternative design criteria allow for different approaches. One early proposal for an RR-HARQ scheme without CSIT involved simple power ramping [283]. It was later discovered in [284] that for block fading channels without CSIT, the optimal power allocation sequence cannot be characterised as either increasing or decreasing. This can be contrasted with the discovery that for slow fading channels with perfect CSIT, the TX powers should decrease with each retransmission [285].

In [286, 287], average TX power minimisation strategies under a packet drop probability (PDP) constraint were proposed for rate allocation IR-HARQ systems that had access to one-bit ACK/NACK feedback. The scheme proposed in [286], which assumed no CSIT, is somewhat impractical, since channel measurements or simulations were required to establish the necessary PDP statistics. In [287], where statistical CSIT was assumed, a PDP minimisation strategy was developed for a scenario with an average TX power constraint. When a single IR-HARQ transmission was allowed, the PDP and average TX power minimisation schemes became equivalent. However, the optimisation scheme only started to outperform a constant TX power allocation scheme at PDPs below 10^{-2}. Multi-bit feedback also aids TX power optimisation in rate allocation IR-HARQ. There are a couple of papers that have studied the impact of quantised information from slightly different perspectives. In [261], adaptive TX power control strategies for RR-HARQ and IR-HARQ were developed under the assumption of quantised CSIT. In related work [288], quantised feedback was utilised to determine the powers of the IR packets for a block fading channel. Additional feedback bits that inform the transmitter of the level of accumulated mutual information at the receiver bring the throughput closer to the ergodic capacity [261] and reduce the probability of an outage (i.e. PDP) [288]. In [289], under the assumption of a discrete initial transmission rate, an IR-HARQ power allocation strategy was developed for a scenario, where the transmitter had accurate knowledge of the accumulated mutual information at the receiver through a perfect feedback channel while only having statistical CSIT. It should be noted that the discussed rate allocation schemes [261, 286–289] assumed constant IR packet sizes.

The impact of HARQ can be taken into account when an MCS is being selected for the initial transmission. In [290], under a slow fading assumption, instantaneous SINR was utilised to develop an average throughput optimisation criterion for MCS selection along with RR-HARQ. This work was later expanded and improved upon in [291], which also considered IR-HARQ with fixed IR packet sizes. An MCS selection method for RR-HARQ that sought to maximise the delay-limited throughput in temporally correlated channels, which can be viewed as a generalisation of slow and block fading, was proposed in [292]. In slow fading channels, simple ACK/NACK-based code rate switching is also feasible [293].

3 System model and receiver algorithms

SC-FDMA uplink transmission is considered. Hence, Sect. 3.1 presents a general RX correlated frequency-selective MIMO channel model and transports it from TD to FD, while Sect. 3.2 describes the FD-SIC-MMSE equaliser that is used throughout the thesis. For the purposes of this thesis, the specific qualities of the equaliser are only incidental. The main ingredients are the inclusion of MMSE filtering and the presence of iterative feedback from the decoder. This will be discussed more in Chap. 4.

3.1 Channel model

Consider a block fading multipath MIMO channel, where the channel remains quasi-static for the duration of the transmitted block, but is independent between successive blocks. It is assumed that the system employs a sufficiently long cyclic prefix (CP) that negates the inter-block interference (IBI). Thus, in the absence of spatial correlation, a multipath channel with L propagation paths between TX antenna j and RX antenna i can be represented as a circulant matrix, i.e. $\boldsymbol{H}_{i,j} = \text{circ}\left\{\left[h_{i,j,1}, \ldots, h_{i,j,l}, \ldots, h_{i,j,L}, \mathbf{0}_{K-L}^{\text{T}}\right]^{\text{T}}\right\} \in \mathbb{C}^{K\times K}$, where $\text{circ}\{\cdot\}$ generates a circulant matrix, $h_{i,j,l}$ is the channel coefficient of the lth path between TX antenna j and RX antenna i, $\mathbf{0}_N$ denotes a $N \times 1$ vector of zeros, $(\cdot)^{\text{T}}$ indicates a transpose and K denotes the length of the associated DFT and IDFT. The time domain channel coefficient, $h_{i,j,l}$, is a complex Gaussian[8] random variable with zero mean and variance ξ_l^2, i.e. $h_{i,j,l} \sim \mathcal{CN}\left(0, \xi_l^2\right)$, where ξ_l is the statistical average amplitude of the impulse response of the lth path, and $\sum_{l=1}^{L} \xi_l^2 = 1$. Thus, the multipath MIMO channel matrix with spatially uncorrelated entries,

$$\boldsymbol{H} = \begin{bmatrix} \boldsymbol{H}_{1,1} & \cdots & \boldsymbol{H}_{1,N_{\text{T}}} \\ \vdots & \ddots & \vdots \\ \boldsymbol{H}_{N_{\text{R}},1} & \cdots & \boldsymbol{H}_{N_{\text{R}},N_{\text{T}}} \end{bmatrix} \in \mathbb{C}^{N_{\text{R}}K\times N_{\text{T}}K}, \tag{1}$$

where N_{R} and N_{T} denote the number of RX and TX antennas, respectively. It shall be assumed that $N_{\text{R}} \geq N_{\text{T}}$. Furthermore, all the signals that have propagated through different paths face the same RX correlation matrix $\boldsymbol{R} \in [0,1]^{N_{\text{R}}\times N_{\text{R}}}$.

[8]Notations $z \sim \mathcal{N}\left(\mu, \sigma^2\right)$ and $z \sim \mathcal{CN}\left(\mu, \sigma^2\right)$ stand for real and complex Gaussian random variables, respectively, where μ and σ^2 denote the mean and variance, respectively.

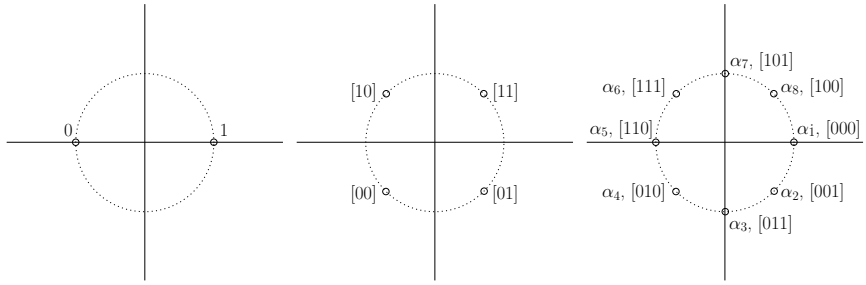

Fig. 1. Gray mapped PSK constellations. All constellation points lie on the unit circle and the Euclidean distance between two adjacent symbols is constant for each modulation. The symbol coordinates, α_n, $n = 1, \ldots, 8$, of 8-PSK are used in soft symbol-to-bit demapping (see Table 1).

In the so-called "Kronecker model", the spatial correlation matrix of a MIMO channel is represented as a Kronecker product of separate TX and RX correlation matrices [294]. Although this model has known deficiencies [295–297], it is analytically convenient. As will be later seen in Sect. 4.2.1, the MIMO channel's approximated SINR distribution can take into account RX correlation, when the Kronecker model is assumed.

Consider two simple types of correlation. For equicorrelated matrices, all the off-diagonal elements of $\boldsymbol{R}$ contain coefficients $\rho \in [0, 1]$. In the case of exponential correlation,

$$\boldsymbol{R} = \begin{bmatrix} 1 & \rho & \cdots & \rho^{N_\mathrm{R}-1} \\ \rho & 1 & \cdots & \rho^{N_\mathrm{R}-2} \\ \vdots & \ddots & \ddots & \vdots \\ \rho^{N_\mathrm{R}-1} & \cdots & \rho & 1 \end{bmatrix} \in [0, 1]^{N_\mathrm{R} \times N_\mathrm{R}}. \tag{2}$$

Let $\breve{\boldsymbol{R}} = \boldsymbol{R} \otimes \boldsymbol{I}_K \in [0, 1]^{N_\mathrm{R}K \times N_\mathrm{R}K}$, where $\boldsymbol{I}_K$ is a $K \times K$ identity matrix and $\otimes$ denotes the Kronecker product. By Cholesky decomposition, $\breve{\boldsymbol{R}} = \breve{\boldsymbol{R}}^{\frac{1}{2}} \breve{\boldsymbol{R}}^{\frac{\mathrm{T}}{2}}$. $\boldsymbol{P} \in [0, 1]^{N_\mathrm{T} \times N_\mathrm{T}}$ is the TX power matrix whose diagonals, P_j, contain the antenna-wise TX powers. The powers are scaled such that $P_\mathrm{tot} = \sum_{j=1}^{N_\mathrm{T}} P_j = 1$. Let $\breve{\boldsymbol{P}} = \boldsymbol{P} \otimes \boldsymbol{I}_K$. The TX signal vector is denoted by $\boldsymbol{x} = \left[\boldsymbol{x}_1^\mathrm{T}, \ldots, \boldsymbol{x}_{N_\mathrm{T}}^\mathrm{T}\right]^\mathrm{T}$, where the stream-wise symbols $\boldsymbol{x}_j \in \mathcal{M}_j^{K \times 1}$, with $\mathcal{M}_j$ denoting the modulation alphabet of the jth stream.

Using DFT and IDFT, $\boldsymbol{H}$, which is composed of circulant submatrices, is transformed to an FD matrix that is composed of diagonal submatrices. The received signal is

expressed as

$$\boldsymbol{r} = \breve{\boldsymbol{R}}^{\frac{1}{2}} \boldsymbol{H} \breve{\boldsymbol{P}}^{\frac{1}{2}} \boldsymbol{x} + \boldsymbol{\eta} = \mathfrak{F}_{\mathrm{R}}^{-1} \breve{\boldsymbol{R}}^{\frac{1}{2}} \boldsymbol{\Phi} \breve{\boldsymbol{P}}^{\frac{1}{2}} \mathfrak{F}_{\mathrm{T}} \boldsymbol{x} + \boldsymbol{\eta} \in \mathbb{C}^{N_{\mathrm{R}} K \times 1}, \tag{3}$$

where the FD channel matrix,

$$\boldsymbol{\Phi} = \begin{bmatrix} \boldsymbol{\Phi}_{1,1} & \cdots & \boldsymbol{\Phi}_{1,N_{\mathrm{T}}} \\ \vdots & \ddots & \vdots \\ \boldsymbol{\Phi}_{N_{\mathrm{R}},1} & \cdots & \boldsymbol{\Phi}_{N_{\mathrm{R}},N_{\mathrm{T}}} \end{bmatrix} \in \mathbb{C}^{N_{\mathrm{R}} K \times N_{\mathrm{T}} K}, \tag{4}$$

in which $\boldsymbol{\Phi}_{i,j}$ are the $K \times K$ diagonal submatrices. $\boldsymbol{\eta} \in \mathbb{C}^{N_{\mathrm{R}} K \times 1}$ is the independently and identically distributed (IID) Gaussian noise vector with zero mean and variance σ_η^2, i.e. $\boldsymbol{\eta} \sim \mathcal{CN}\left(\boldsymbol{0}_{N_{\mathrm{R}} K}, \sigma_\eta^2 \boldsymbol{I}_{N_{\mathrm{R}} K}\right)$. $\mathfrak{F} \in \mathbb{C}^{K \times K}$ is the unitary DFT matrix, whose elements, $f_{k_1,k_2} = K^{-1/2} \exp\left(-\jmath 2\pi \left(k_1 - 1\right)\left(k_2 - 1\right)/K\right)$, with $k_1, k_2 = 1, \ldots, K$, and $\jmath = \sqrt{-1}$. $\mathfrak{F}_{\mathrm{T}} = \boldsymbol{I}_{N_{\mathrm{T}}} \otimes \mathfrak{F} \in \mathbb{C}^{N_{\mathrm{T}} K \times N_{\mathrm{T}} K}$ is a block diagonal DFT matrix. $\mathfrak{F}_{\mathrm{R}}^{-1} = \boldsymbol{I}_{N_{\mathrm{R}}} \otimes \mathfrak{F}^{-1} \in \mathbb{C}^{N_{\mathrm{R}} K \times N_{\mathrm{R}} K}$, where the elements of the IDFT matrix $\mathfrak{F}^{-1}$ are $f^{\mathrm{i}}_{k_1,k_2} = K^{-1/2} \exp\left(\jmath 2\pi \left(k_1 - 1\right)\left(k_2 - 1\right)/K\right)$, $k_1, k_2 = 1, \ldots, K$. The Cholesky decomposition of $\breve{\boldsymbol{R}}$ is a triangular block matrix, whose submatrices are products of scalars and identity matrices. For such matrices, $\mathfrak{F}_{\mathrm{R}}^{-1} \breve{\boldsymbol{R}}^{\frac{1}{2}} \mathfrak{F}_{\mathrm{R}} = \breve{\boldsymbol{R}}^{\frac{1}{2}}$. Similarly, $\mathfrak{F}_{\mathrm{T}}^{-1} \breve{\boldsymbol{P}}^{\frac{1}{2}} \mathfrak{F}_{\mathrm{T}} = \breve{\boldsymbol{P}}^{\frac{1}{2}}$.

3.2 Frequency domain soft interference cancellation MMSE equaliser

The FD-SIC-MMSE equaliser considered in this thesis was previously the focus of Kansanen's D.Sc. (Tech.) thesis [298]. The work was carried on, particularly in an MU scenario, in Karjalainen's D.Sc. (Tech.) thesis [299]. For a more detailed treatment of the equaliser, the reader is referred to [120, 121] or to the two theses above, which also offer a comprehensive survey of advanced equalisation techniques. Throughout the thesis, perfect CSIR is assumed.

The receiver, depicted in Fig. 2, contains two iterative loops. In the outer loop, the turbo decoder operates in parallel with an FD-SIC-MMSE equaliser. The receiver performs a predetermined number of global (or outer) iterations between the equaliser and decoder. The second loop is within the decoder, which performs a fixed number of iterations before passing the soft output bits to the equaliser. Fig. 2 displays the receiver structure for horizontally encoded and MU-MIMO transmissions, where the parallel streams are decoded separately. For vertically encoded transmissions, the parallel spatial LLR streams are serialised after soft demapping, and again parallelised before soft symbol mapping.

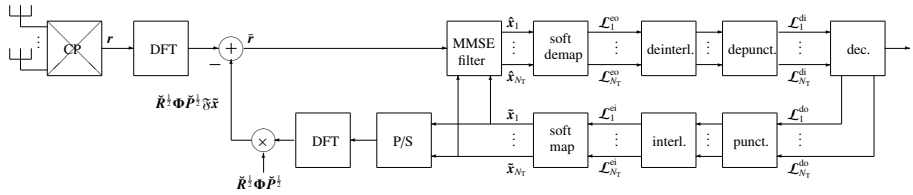

Fig. 2. Block diagram of the iterative receiver for horizontally encoded and MU-MIMO transmissions. For vertically encoded transmission, a parallel-to-serial converter is added between the soft demapper and deinterleaver, and a serial-to-parallel converter is added between the interleaver and soft mapper. RR is performed between depuncturing and decoding. ([73], © 2014 IEEE.)

For the symbols transmitted from the jth antenna, the equaliser output $\hat{\boldsymbol{x}}_j \in \mathbb{C}^{K\times 1}$,

$$\hat{\boldsymbol{x}}_j = \frac{\operatorname{avg}\left(\dot{\boldsymbol{x}}_j\right)}{1+\beta_j \operatorname{avg}\left(\ddot{\boldsymbol{x}}_j\right)}\left(\Im^{-1} P_j^{\frac{1}{2}} \boldsymbol{\Phi}_j^{\mathrm{H}} \breve{\boldsymbol{R}}^{\frac{\mathrm{T}}{2}} \boldsymbol{\Sigma}_{\bar{\boldsymbol{r}}_{\mathrm{FD}}}^{-1} \bar{\boldsymbol{r}}_{\mathrm{FD}} + \beta_j \tilde{\boldsymbol{x}}_j\right), \tag{5}$$

where $\operatorname{avg}(\cdot)$ represents the mean of the scalar values of a vector, $(\cdot)^{\mathrm{H}}$ denotes the complex conjugate transpose, $\boldsymbol{\Phi}_j \in \mathbb{C}^{N_{\mathrm{R}}K\times K}$ denotes $\boldsymbol{\Phi}$'s jth column of blocks, $\tilde{\boldsymbol{x}}_j = \mathrm{E}\left\{\boldsymbol{x}_j\right\} \in \mathbb{C}^{K\times 1}$ is the soft symbol estimate vector with $\mathrm{E}\{\cdot\}$ denoting the expected value and $\bar{\boldsymbol{r}}_{\mathrm{FD}} = \Im_{\mathrm{R}}\boldsymbol{r} - \breve{\boldsymbol{R}}^{\frac{1}{2}}\boldsymbol{\Phi}\breve{\boldsymbol{P}}^{\frac{1}{2}}\Im_{\mathrm{T}}\tilde{\boldsymbol{x}} \in \mathbb{C}^{N_{\mathrm{R}}K\times 1}$ is the FD residual vector after SIC. Then, let $\dot{\boldsymbol{x}}_j = \left[\mathrm{E}\left\{|x_{j,1}|^2\right\},\ldots,\mathrm{E}\left\{|x_{j,K}|^2\right\}\right]^{\mathrm{T}} \in \mathbb{R}^{K\times 1}$ and $\ddot{\boldsymbol{x}}_j = \left[\mathrm{E}\left\{|\tilde{x}_{j,1}|^2\right\},\ldots,\mathrm{E}\left\{|\tilde{x}_{j,K}|^2\right\}\right]^{\mathrm{T}} \in \mathbb{R}^{K\times 1}$, where $\tilde{x}_{j,k}$ denotes the soft symbol estimate for the jth TX antenna at the kth frequency bin that is constructed from the decoder's output LLRs. For $\mathcal{M}_j$'s with normalised mean power, $\operatorname{avg}\left(\dot{\boldsymbol{x}}_j\right) = 1$.

The effective SINR,

$$\beta_j = \frac{1}{K}\operatorname{tr}\left\{P_j \boldsymbol{\Phi}_j^{\mathrm{H}} \breve{\boldsymbol{R}}^{\frac{\mathrm{T}}{2}} \boldsymbol{\Sigma}_{\bar{\boldsymbol{r}}_{\mathrm{FD}}}^{-1} \breve{\boldsymbol{R}}^{\frac{1}{2}} \boldsymbol{\Phi}_j\right\}, \tag{6}$$

where $\operatorname{tr}\{\cdot\}$ is the trace of a matrix and $\boldsymbol{\Sigma}_{\bar{\boldsymbol{r}}_{\mathrm{FD}}} = \sigma_\eta^2 \boldsymbol{I}_{N_{\mathrm{R}}K} + \breve{\boldsymbol{R}}^{\frac{1}{2}}\boldsymbol{\Phi}\breve{\boldsymbol{P}}\boldsymbol{\Delta}\boldsymbol{\Phi}^{\mathrm{H}}\breve{\boldsymbol{R}}^{\frac{\mathrm{T}}{2}} \in \mathbb{C}^{N_{\mathrm{R}}K\times N_{\mathrm{R}}K}$ is the covariance matrix of the FD residual vector after SIC[9]. The residual interference energy is contained on the diagonals of $\boldsymbol{\Delta} \in [0,1]^{N_{\mathrm{T}}K\times N_{\mathrm{T}}K}$,

$$\boldsymbol{\Delta} = \operatorname{diag}\left\{\left(\operatorname{avg}\left(\dot{\boldsymbol{x}}_1\right) - \operatorname{avg}\left(\ddot{\boldsymbol{x}}_1\right)\right)\boldsymbol{1}_K,\ldots,\left(\operatorname{avg}\left(\dot{\boldsymbol{x}}_{N_{\mathrm{T}}}\right) - \operatorname{avg}\left(\ddot{\boldsymbol{x}}_{N_{\mathrm{T}}}\right)\right)\boldsymbol{1}_K\right\} \tag{7}$$

$$= \operatorname{diag}\left\{\left(1 - \operatorname{avg}\left(\ddot{\boldsymbol{x}}_1\right)\right)\boldsymbol{1}_K,\ldots,\left(1 - \operatorname{avg}\left(\ddot{\boldsymbol{x}}_{N_{\mathrm{T}}}\right)\right)\boldsymbol{1}_K\right\}. \tag{8}$$

[9]When $K \gg L$, the FD channel coefficients of neighbouring frequency bins are almost identical. Thus, in the calculation of β_j, it is sufficient to consider a $N_{\mathrm{R}}K' \times N_{\mathrm{R}}K'$ covariance matrix $\boldsymbol{\Sigma}_{\bar{\boldsymbol{r}}_{\mathrm{FD}}}$, where the K' frequency bins are evenly distributed across the signal's frequency spectrum. Throughout the featured simulations, $K' = 32$.

where diag $\{\cdot\}$ transforms a $N_{\mathrm{T}}K$-length vector to a $N_{\mathrm{T}}K \times N_{\mathrm{T}}K$ diagonal matrix and $\mathbf{1}_N$ denotes a $N \times 1$ vector of ones.

The MMSE filter outputs can be approximated as

$$\hat{x}_{j,k} = \mu_j x_{j,k} + \omega, \tag{9}$$

where

$$\mu_j = \frac{\beta_j}{1 + \beta_j \left(1 - \frac{1}{K}\mathrm{tr}\{\mathbf{\Delta}_j\}\right)}, \tag{10}$$

and $\omega \sim \mathcal{CN}\left(0, \mu_j(1-\mu_j)\right)$.

The soft symbols, $\hat{\boldsymbol{x}}$, need to be converted into soft bits, i.e. LLRs, $\boldsymbol{\mathcal{L}}^{\mathrm{eo}}$, which after deinterleaving and depuncturing become decoder inputs, $\boldsymbol{\mathcal{L}}^{\mathrm{di}}$.[10] After decoding, the soft bits, $\boldsymbol{\mathcal{L}}^{\mathrm{do}}$, are reinterleaved and repunctured to $\boldsymbol{\mathcal{L}}^{\mathrm{ei}}$, which are then converted into soft symbols, $\tilde{\boldsymbol{x}}$, to be used in (5). The soft symbol-to-bit and bit-to-symbol conversion formulae are found in Tables 1 and 2, respectively.[11] They are principally the same as those in [106], but slightly altered due to different mappings. Therefore, they are reproduced here. The real and imaginary parts of a complex number are denoted by $\Re(\cdot)$ and $\Im(\cdot)$, respectively.

The vertically encoded transmission is complemented by the inclusion of RR-HARQ. Two distinct options are considered. In the simpler one, only the latest received version of the packet is equalised during each global iteration cycle. In the more complex option, as proposed in [117], the different versions of the received packet are equalised separately during each global iteration cycle before they are combined. The processing gain arises from the enhanced quality of the decoder's output LLRs. The latter method requires more memory, since the channel coefficients and received signal vectors of the previous transmissions need to be stored for future equalisation. Compared to the simpler option, the latter method is expected to reduce the FER, since the effective SINRs of the preceding transmissions are improved through SIC. The selection of the combination technique does not impact the transmitter, which in both cases only retransmits the original packet.

RR is performed at the input of the decoder. In the simpler RR scenario, the LLR values at the decoder input are obtained by summing the demapped, serialised,

[10] The equaliser outputs soft symbols, as in (5). However, the demapper is considered to be intrinsically connected to the equaliser. In the context of LLRs, the equaliser output technically refers to the demapper output.

[11] The complex conjugates of the 8-PSK symbol coordinates, α_n^*, $n = 1, \ldots, 8$, required in Table 1, are found from Fig. 1c.

Table 1. Soft symbol-to-bit conversion.

Modulation	Conversion formulae
BPSK	$\mathcal{L}^{\mathrm{eo}}_{j,k} = \frac{4}{1-\mu_j}\,\Re\left(\hat{x}_{j,k}\right),$
QPSK	$\mathcal{L}^{\mathrm{eo}}_{j,2(k-1)+1} = \frac{\sqrt{8}}{1-\mu_j}\,\Re\left(\hat{x}_{j,k}\right),$ $\mathcal{L}^{\mathrm{eo}}_{j,2(k-1)+2} = \frac{\sqrt{8}}{1-\mu_j}\,\Im\left(\hat{x}_{j,k}\right),$
8-PSK	$q^{j,k}_n = \frac{2}{1-\mu_j}\,\Re\left(\hat{x}_{j,k}\alpha^*_n\right), \quad n = 1,\ldots,8,$ $\hat{\ell}^{j,k}_n = \frac{\mathcal{L}^{\mathrm{ei}}_{j,3(k-1)+n}}{2}, \quad n = 1,\ldots,3,$ $\mathcal{L}^{\mathrm{eo}}_{j,3(k-1)+1} = \ln\left(\frac{e^{q^{j,k}_6+\hat{\ell}^{j,k}_2+\hat{\ell}^{j,k}_3}+e^{q^{j,k}_5+\hat{\ell}^{j,k}_2-\hat{\ell}^{j,k}_3}+e^{q^{j,k}_7-\hat{\ell}^{j,k}_2+\hat{\ell}^{j,k}_3}+e^{q^{j,k}_8-\hat{\ell}^{j,k}_2-\hat{\ell}^{j,k}_3}}{e^{q^{j,k}_3+\hat{\ell}^{j,k}_2+\hat{\ell}^{j,k}_3}+e^{q^{j,k}_4+\hat{\ell}^{j,k}_2-\hat{\ell}^{j,k}_3}+e^{q^{j,k}_2-\hat{\ell}^{j,k}_2+\hat{\ell}^{j,k}_3}+e^{q^{j,k}_1-\hat{\ell}^{j,k}_2-\hat{\ell}^{j,k}_3}}\right),$ $\mathcal{L}^{\mathrm{eo}}_{j,3(k-1)+2} = \ln\left(\frac{e^{q^{j,k}_6+\hat{\ell}^{j,k}_1+\hat{\ell}^{j,k}_3}+e^{q^{j,k}_5+\hat{\ell}^{j,k}_1-\hat{\ell}^{j,k}_3}+e^{q^{j,k}_3-\hat{\ell}^{j,k}_1+\hat{\ell}^{j,k}_3}+e^{q^{j,k}_4-\hat{\ell}^{j,k}_1-\hat{\ell}^{j,k}_3}}{e^{q^{j,k}_7+\hat{\ell}^{j,k}_1+\hat{\ell}^{j,k}_3}+e^{q^{j,k}_8+\hat{\ell}^{j,k}_1-\hat{\ell}^{j,k}_3}+e^{q^{j,k}_2-\hat{\ell}^{j,k}_1+\hat{\ell}^{j,k}_3}+e^{q^{j,k}_1-\hat{\ell}^{j,k}_1-\hat{\ell}^{j,k}_3}}\right),$ $\mathcal{L}^{\mathrm{eo}}_{j,3(k-1)+3} = \ln\left(\frac{e^{q^{j,k}_6+\hat{\ell}^{j,k}_1+\hat{\ell}^{j,k}_2}+e^{q^{j,k}_7+\hat{\ell}^{j,k}_1-\hat{\ell}^{j,k}_2}+e^{q^{j,k}_3-\hat{\ell}^{j,k}_1+\hat{\ell}^{j,k}_2}+e^{q^{j,k}_2-\hat{\ell}^{j,k}_1-\hat{\ell}^{j,k}_2}}{e^{q^{j,k}_5+\hat{\ell}^{j,k}_1+\hat{\ell}^{j,k}_2}+e^{q^{j,k}_8+\hat{\ell}^{j,k}_1-\hat{\ell}^{j,k}_2}+e^{q^{j,k}_4-\hat{\ell}^{j,k}_1+\hat{\ell}^{j,k}_2}+e^{q^{j,k}_1-\hat{\ell}^{j,k}_1-\hat{\ell}^{j,k}_2}}\right).$

Table 2. Soft bit-to-symbol conversion.

Modulation	Conversion formulae
BPSK	$\tilde{x}_{j,k} = \tanh\left(\frac{\mathcal{L}^{\mathrm{ei}}_{j,k}}{2}\right),$
QPSK	$\tilde{x}_{j,k} = \frac{1}{\sqrt{2}}\left(\tanh\left(\frac{\mathcal{L}^{\mathrm{ei}}_{j,2(k-1)+1}}{2}\right)+\jmath\tanh\left(\frac{\mathcal{L}^{\mathrm{ei}}_{j,2(k-1)+2}}{2}\right)\right),$
8-PSK	$\tilde{\ell}^{j,k}_n = \tanh\left(\frac{\mathcal{L}^{\mathrm{ei}}_{j,3(k-1)+n}}{2}\right), \quad n = 1,\ldots,3,$ $\tilde{x}_{j,k} = \frac{\left(1+\sqrt{2}\right)\jmath-1}{4}\tilde{\ell}^{j,k}_1 - \frac{1+\sqrt{2}+\jmath}{4}\tilde{\ell}^{j,k}_2$ $+\,\tilde{\ell}^{j,k}_3\left(\frac{1-\sqrt{2}+\jmath}{4}\tilde{\ell}^{j,k}_1 + \frac{1+\left(\sqrt{2}-1\right)\jmath}{4}\tilde{\ell}^{j,k}_2\right).$

deinterleaved and depunctured LLRs from the latest equaliser output, $\bar{\boldsymbol{\mathcal{L}}}^{\mathrm{eo},w,d}$, with the ones from the last global iteration of the previous transmissions. The packet transmission and global iteration indices are denoted by w and d, respectively. Since the N_{T} parallel streams were serialised to a single stream, stream-wise indexing is omitted. Thus, the nth LLR at the decoder input

$$\mathcal{L}_n^{\mathrm{di},w,d} = \begin{cases} \bar{\mathcal{L}}_n^{\mathrm{eo},w,d}, & w = 1, \\ \bar{\mathcal{L}}_n^{\mathrm{eo},w,d} + \sum_{u=1}^{w-1} \bar{\mathcal{L}}_n^{\mathrm{eo},u,N_d}, & w \geq 2, \end{cases} \tag{11}$$

where $\bar{\mathcal{L}}_n^{\mathrm{eo},w,d}$ is the nth demapped LLR of the equaliser output after serialisation, deinterleaving and depuncturing, and N_d denotes the maximum number of global iterations. For the more complex RR-HARQ option, where each version of the received packet is equalised separately during each global iteration cycle, the nth LLR at the decoder input

$$\mathcal{L}_n^{\mathrm{di},w,d} = \begin{cases} \bar{\mathcal{L}}_n^{\mathrm{eo},w,d}, & w = 1, \\ \bar{\mathcal{L}}_n^{\mathrm{eo},w,d} + \sum_{u=1}^{w-1} \bar{\mathcal{L}}_n^{\mathrm{eo},u,N_d(w-u)+d}, & w \geq 2. \end{cases} \tag{12}$$

Thus, the uth version of the received packet is equalised $N_d\,(w-u)+d$ times.

4 Semi-analytical receiver performance prediction

The core contribution of the thesis is featured in this chapter. Although a very specific equaliser is considered, the semi-analytical framework allows the same prediction method to be applied, at least in principle, with different MMSE filters and even with ZF filters, by utilising the PDFs developed in [167].

The papers that helped establish the framework for the convergence analysis of iterative receivers often assumed convolutional codes, e.g. [107–117, 140–146]. It is assumed here that the constituent decoders of the turbo decoder only exchange extrinsic information between each other and that there is no alternating activation scheduling between the equaliser and the constituent decoders. Therefore, the established convergence analysis framework can be used here. This also implies that convolutional codes would be a convenient channel coding option for the proposed performance prediction method. In [148, 149], RA codes, with the sum-product decoding algorithm, were successfully used to evaluate the convergence of iterative receivers. Naturally, LDPC codes would also merit consideration. In general, codes that can be described by factor graphs and decoded by belief propagation algorithms are strong candidates.

4.1 Mutual information transfer charts and convergence analysis

Mutual information transfer charts provide a neat way to visualise the convergence of an iterative decoder. The intersection point of the curves identifies the attainable level of mutual information, assuming that a sufficient number of iterations are performed. The turbo decoder inputs and outputs LLRs. Thus, it is necessary to establish a relation between the LLRs and mutual information. Consider the real-valued LLR vector

$$\boldsymbol{\mathcal{L}} = \frac{\sigma_{\mathrm{a}}^2}{2}\boldsymbol{b} + \boldsymbol{\eta}_{\mathrm{a}} \in \mathbb{R}^{N_b \times 1}, \tag{13}$$

where $\boldsymbol{b} \in \{-1, 1\}^{N_b \times 1}$ contains the original N_b bits and $\boldsymbol{\eta}_{\mathrm{a}} \sim \mathcal{N}\left(\mathbf{0}_{N_b}, \sigma_{\mathrm{a}}^2 \boldsymbol{I}_{N_b}\right)$. Thus, $\mathcal{L}_n \sim \mathcal{N}\left(\pm\sigma_{\mathrm{a}}^2/2, \sigma_{\mathrm{a}}^2\right)$ satisfy the consistency condition [94], with the sign of $\mathcal{L}_n$ being conditioned on the sign of b_n.

Table 3. The parameters of the approximate J-function in (15a), Gray mapping (Modified from [73], © 2014 IEEE.)

Modulation	H_1	H_2	H_3
BPSK [300]	0.3073	0.8935	1.1064
QPSK [120, 298]	0.3073	0.8935	1.1064
8-PSK [120, 298]	0.2516	0.7274	1.2392

Knowing the signs of the bits, the mutual information, $I_\mathrm{a} \in [0, 1]$, can be calculated from the LLRs [138],

$$I_\mathrm{a} = \frac{1}{2} \sum_{q=\pm 1} \int_{-\infty}^{\infty} f_{\mathcal{L}}\left(\mathcal{L} \middle| b = q\right) \log_2 \left(\frac{2 f_{\mathcal{L}}\left(\mathcal{L} \middle| b = q\right)}{f_{\mathcal{L}}\left(\mathcal{L} \middle| b = -1\right) + f_{\mathcal{L}}\left(\mathcal{L} \middle| b = 1\right)} \right) d\mathcal{L}, \tag{14}$$

where $f_{\mathcal{L}}\left(\mathcal{L} \middle| b = q\right)$ denotes the conditional PDF of the LLRs. Thus, I_a and σ_a are related through a bijective J-function, i.e. $I_\mathrm{a} = J(\sigma_\mathrm{a})$ and $\sigma_\mathrm{a} = J^{-1}(I_\mathrm{a})$. When the bit-sign-wise mean of the LLRs is half of their variance, σ_a^2, a convenient, approximate J-function and its inverse can be used [300],

$$J(\sigma_\mathrm{a}) \approx \left(1 - 2^{-H_1 \sigma_\mathrm{a}^{2H_2}}\right)^{H_3}, \tag{15a}$$

$$J^{-1}(I_\mathrm{a}) \approx \left(-\frac{1}{H_1} \log_2 \left(1 - I_\mathrm{a}^{\frac{1}{H_3}}\right)\right)^{\frac{1}{2H_2}}, \tag{15b}$$

where H_1, H_2 and H_3 depend on the chosen modulation and mapping. Table 3 lists them for BPSK and Gray-mapped versions of QPSK and 8-PSK.

Before proceeding further, two notable weaknesses associated with the considered prediction method need to be pointed out. The considered receiver uses the *a posteriori* LLRs, after de/interleaving and de/puncturing, as inputs to the decoder and in soft symbol mapping, as it has been noted to lead to a better performance than the use of extrinsic information values [119, 301–303]. The difference in performance is usually slight in terms of SNR, but is sufficiently large at a particular SNR value for moderate FERs to warrant the use of *a posteriori* values. Thus, labelling the equaliser chart as an EXIT chart would be something of a misnomer. A bigger issue is that while semi-analytically evaluating the equaliser's performance, the decoder's bit-sign-wise conditioned feedback LLRs are assumed to be Gaussian distributed [120]. In reality, the joint distribution of the conditional *a posteriori* LLRs of the information and unpunctured parity bits at the output of a turbo decoder is not Gaussian. This deviation from the ideal, bit-sign-wise Gaussian densities also leads to suboptimal equaliser

performance. This issue is circumvented by using the extrinsic information of the information bits, whose conditional LLR distribution is approximately Gaussian, as a performance metric. In other words, the decoder's EXIT charts are considered, even though the receiver actually uses the *a posteriori* LLRs of the information and parity bits. Although this approach does not provide a completely accurate depiction of the receiver's (possible) convergence, the chosen metric and approach are sensible and sufficiently accurate, as will be later illustrated in Fig. 3. Even though the decoder's *a posteriori* LLRs are used in soft symbol mapping, the possible gain the equaliser enjoys in SIC is based on the extrinsic information provided by the decoder. If the decoder is unable to reduce the number of bit errors and produce extrinsic information, further attempts of SIC do not help.

A second issue is the distribution of the LLRs after soft symbol-to-bit demapping. The behaviour of an SIC-MMSE equaliser that operated as a part of a DS-CDMA system was studied in [114]. It was discovered that with BPSK and Gray-mapped QPSK, the LLRs at the demapper's output approximately satisfy the assumption that the mean of the LLRs is half of their variance. Furthermore, it was observed that the distributions of the LLRs exchanged between the equaliser and decoder can be approximated as Gaussian, even though fading multipath channels were considered, as opposed to AWGN channels.

Here, 8-PSK is also considered, even though the demapper's output LLR distribution does not reduce to a Gaussian density, although it is symmetric, thereby satisfying the consistency condition. This can be deduced intuitively from Fig. 1c. For the first two bit positions, all symbols containing either -1's or 1's lie on different half-planes. For any symbol, one of the neighbouring symbols has an opposite valued third bit. Therefore, the LLRs of the third bit are bound to have smaller absolute means than the LLRs of the first two bits. Thus, the joint LLR distribution cannot be reduced to a single Gaussian density. Nevertheless, Fig. 3 and the numerical results in Sect. 4.4 illustrate that the deviation from the ideal Gaussian density is not so severe that the approximation would become invalid.

Similarly to Table 3, H_1, H_2 and H_3 values for Gray-mapped 16-QAM can also be found in [120, 298]. However, during the preparation of this thesis it was observed that the distribution of the demapped LLRs significantly deviated from the Gaussian distribution assumed in the simulation of the decoder EXIT charts. Thus, the accuracy of the FER prediction was compromised: the predicted FER started to decrease at the proper SNR range, but the turbo cliff of the predicted FER curve was steeper than the

turbo cliff of the MC simulated curve. Thus, 16-QAM shall not be considered in this thesis. Other examples of the deficiencies of EXIT charts can be found in [132, 151].

Bearing this in mind, the decoder is viewed as a bijective function, which maps a certain *a priori* information value, $\tilde{I}_{\mathrm{a},j}^{\mathrm{apr}} \in [0,1]$, to a unique extrinsic information value, $\tilde{I}_{\mathrm{a},j}^{\mathrm{ext}} \in [0,1]$, for the information bits. MC simulations are required to find the corresponding pairs of $\tilde{I}_{\mathrm{a},j}^{\mathrm{apr}}$ and $\tilde{I}_{\mathrm{a},j}^{\mathrm{ext}}$ for different code rates. At this point, the analysis is deliberately detached from the actual performance of the receiver. Here $\tilde{I}_{\mathrm{a},j}^{\mathrm{ext}}$ becomes *a priori* information for the equaliser, i.e. $\hat{I}_{\mathrm{a},j}^{\mathrm{apr}} = \tilde{I}_{\mathrm{a},j}^{\mathrm{ext}}$, even though the genuine receiver uses the *a posteriori* LLRs of the information and uncpunctured parity bits to calculate the soft symbol estimates, $\tilde{\boldsymbol{x}}$. The equaliser uses $\tilde{\boldsymbol{x}}$, associated with $\hat{\boldsymbol{I}}_{\mathrm{a}}^{\mathrm{apr}} = \left[\hat{I}_{\mathrm{a},1}^{\mathrm{apr}}, \ldots, \hat{I}_{\mathrm{a},N_{\mathrm{T}}}^{\mathrm{apr}}\right] \in [0,1]^{N_{\mathrm{T}} \times 1}$ and the channel matrix to calculate its output soft symbol estimates, $\hat{\boldsymbol{x}}$. These are soft demapped into LLRs, with mutual information level $\hat{I}_{\mathrm{a},j}^{\mathrm{apo}}$, which subsequently become inputs for decoder, i.e. $\tilde{I}_{\mathrm{a},j}^{\mathrm{apr}} = \hat{I}_{\mathrm{a},j}^{\mathrm{apo}}$. Alternatively expressed,

$$\tilde{I}_{\mathrm{a},j}^{\mathrm{ext}} = \tilde{g}_j\left(\tilde{I}_{\mathrm{a},j}^{\mathrm{apr}}\right), \quad j = 1, \ldots, N_{\mathrm{T}}, \tag{16a}$$

$$\hat{\boldsymbol{I}}_{\mathrm{a}}^{\mathrm{apo}}(t) = \hat{g}\left(\hat{\boldsymbol{I}}_{\mathrm{a}}^{\mathrm{apr}}; \check{\boldsymbol{R}}^{\frac{1}{2}} \boldsymbol{H}(t) \check{\boldsymbol{P}}^{\frac{1}{2}}; \mathcal{M}_j, j = 1, \ldots, N_{\mathrm{T}}\right). \tag{16b}$$

Since the equaliser output depends on the channel realisation $\boldsymbol{H}(t)$, where t is the discrete time index used to identify the realisations of the block fading channel matrix, t is included in $\hat{g}(\cdot)$ and $\hat{\boldsymbol{I}}_{\mathrm{a}}^{\mathrm{apo}}(t)$ in (16b), as are the antenna-wise modulation mappings $\mathcal{M}_j$. The index t was omitted in Chap. 3 for notational conciseness. The channel has no direct impact on the decoder's performance; the decoder only sees variations in $\tilde{I}_{\mathrm{a},j}^{\mathrm{apr}}$. The decoder's mapping function, $\tilde{g}_j(\cdot)$, takes into account the stream-wise code rates, $R_{\mathrm{c},j}$. A successful convergence requires an open tunnel between the equaliser and decoder graphs for all pairs of $\hat{I}_{\mathrm{a},j}^{\mathrm{apr}}(t)$ and $\tilde{I}_{\mathrm{a},j}^{\mathrm{ext}}$ on the horizontal axis of the mutual information transfer chart (see Figs. 3 and 10), i.e.

$$\hat{I}_{\mathrm{a},j}^{\mathrm{apo}}(t) \geq \tilde{I}_{\mathrm{a},j}^{\mathrm{apr}} + \epsilon, \tag{17}$$

where ϵ is a design variable used to ensure the openness of the tunnel. For practical reasons, which will become apparent in Sect. 4.3, it is desirable to move from the mutual information domain to the LLR variance domain. Since the J-function is monotonically increasing, the condition for a successful convergence in (17) can be, without loss of

generality, reformulated[12] as

$$\left[J^{-1}\left(\hat{I}_{\mathrm{a},j}^{\mathrm{apo}}(t)\right)\right]^2 \geq \left[J^{-1}\left(\tilde{I}_{\mathrm{a},j}^{\mathrm{apr}}+\epsilon\right)\right]^2, \tag{18}$$

which is equivalent to

$$\hat{\sigma}_{\mathrm{a},j}^2(t) \geq \tilde{\sigma}_{\mathrm{a},j}^2 + \tilde{\epsilon}_{\mathrm{a},j}. \tag{19}$$

This same approach can be used to predict the performance of linear receivers. The linear receiver can be viewed as a special case of the iterative receiver, which performs a single global iteration. For a successful convergence, the LLR variance at the equaliser output with no *a priori* information, $\hat{\sigma}_{0,j}^2(t)$, must be above the entire decoder EXIT chart. When viewed from the horizontal axis, the decoder EXIT chart is at its highest when $\tilde{I}_{\mathrm{a},j}^{\mathrm{ext}} \to 1$. The corresponding LLR variance value is denoted as $\tilde{\sigma}_{1,j}^2$. The convergence condition becomes

$$\hat{\sigma}_{0,j}^2(t) \geq \tilde{\sigma}_{1,j}^2 + \tilde{\epsilon}_{1,j}. \tag{20}$$

Thus, in the context of a linear receiver, a successful decoding requires that the equaliser graph's position at the left edge of the chart is above the decoder graph's position at the right edge of the chart.

The accuracy of this approach is demonstrated in Fig. 3. It depicts two measured equaliser *a posteriori* charts for a particular realisation of an uncorrelated 2×2 Proakis-C[13] multipath channel with a vertically encoded[14] transmission. In the first scenario, QPSK and $P_{\mathrm{tot}}/\sigma_\eta^2 = -2$ dB were assumed, while in the second scenario, 8-PSK and $P_{\mathrm{tot}}/\sigma_\eta^2 = 4$ dB were assumed. 3GPP turbo codes of rates $R_{\mathrm{c}} = 1/3$ and $R_{\mathrm{c}} = 1/2$ were applied to the two scenarios, respectively. Their EXIT charts are also depicted. The receiver's convergence is explored by using (14) to calculate the amount of *a posteriori* mutual information at the output of the equaliser and the amount of extrinsic information from the information bits at the output of the decoder.

[12]The mean-to-variance ratio of the decoder's bit-sign-wise extrinsic LLRs is not generally $\pm 1/2$ [132]. For the purposes of the analysis here, it suffices that the mean-to-variance ratio of the equaliser's bit-sign-wise *a posteriori* LLRs is approximately $\pm 1/2$. The J-function can be used to transport the LLR variance to the mutual information domain. However, the requirement of an open convergence tunnel is valid in both domains. Therefore, transportation of the decoder's EXIT graph to the LLR variance domain, by the use of the inverse J-function, serves the exact same purpose.

[13]The statistical average amplitudes of the impulse responses, $\boldsymbol{\xi} = [0.227, 0.460, 0.688, 0.460, 0.227]$ [193, Fig. 10.2-5(c)].

[14]In vertically encoded spatial multiplexing, a single data packet is transmitted across multiple antennas with equal power. Therefore, stream-wise index j can be dropped from the decoder's *a priori* and extrinsic information symbols.

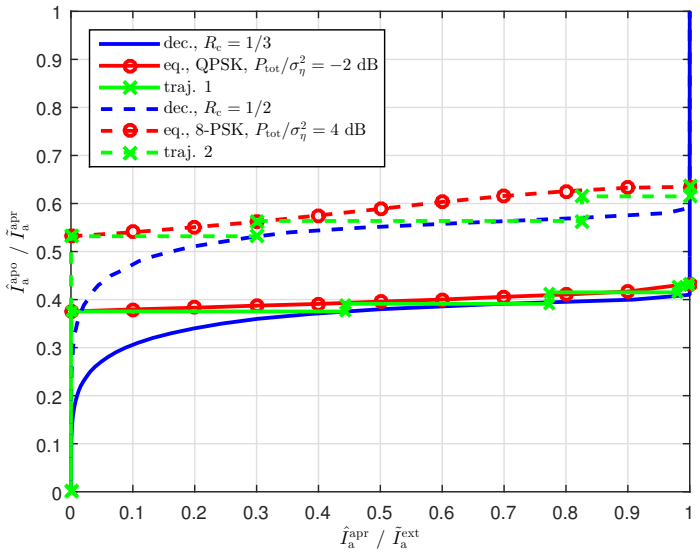

Fig. 3. The measured decoder EXIT and equaliser *a posteriori* transfer charts for a particular realisation of an uncorrelated 2×2 Proakis-C multipath channel and the associated trajectories in a vertically encoded scenario. The first case assumed QPSK, $R_c = 1/3$ and $P_{tot}/\sigma_\eta^2 = -2$ dB, while the second one assumed 8-PSK, $R_c = 1/2$ and $P_{tot}/\sigma_\eta^2 = 4$ dB. ([73], © 2014 IEEE.)

The vertical and horizontal segments of the trajectories correspond to equalisation and decoding, respectively. Even though the trajectories do not always perfectly exploit the full width of the gap between the equaliser and decoder charts, or stay within the gap, the charts are sufficiently accurate to evaluate the probability of a successful convergence. It should be emphasised that the receiver operated in its normal fashion, using the decoder's *a posteriori* LLRs of the transmitted bits in soft bit-to-symbol mapping. Therefore, $\hat{I}_a^{apr}$ and $\tilde{I}_a^{ext}$ on the horizontal axis of Fig. 3 are not the exact same quantities.

4.2 Distribution of the effective SINR at the output of the equaliser/demapper

The distribution of the effective SINR, β_j, which was defined in (6), is approximated in two phases. In Sect. 4.2.1, a flat fading channel is assumed. This can be thought to represent a random frequency bin. Two different scenarios are considered. First, SISO and spatially uncorrelated SIMO channels are assumed. The second scenario considers an RX correlated MIMO channel. The method used with the RX correlated MIMO channel can also take into account SISO and spatially uncorrelated SIMO channels. In

Sect. 4.2.2, the central limit theorem (CLT) is applied to the distributions from Sect. 4.2.1 to approximate the effective SINR distribution of a frequency-selective channel.

4.2.1 Frequency-bin-wise effective SINR distribution

The semi-analytical performance evaluation of the FD-SIC-MMSE equaliser starts by controlling the mutual information level of $\tilde{\boldsymbol{x}}_j$ used in SIC on a stream-wise basis. This is done by forming modulation-wise LUTs. The cardinality of $\mathcal{M}$, i.e. $M = |\mathcal{M}|$, is referred to as the modulation order. For a given I_a, a sequence of LLRs, $\mathcal{L}_n \sim \mathcal{N}\left(\pm\sigma_\mathrm{a}^2/2, \sigma_\mathrm{a}^2\right)$, $n = 1, \ldots, \log_2(M) N_\mathrm{s}$, is generated by applying (15b) with the appropriate H_1, H_2 and H_3 from Table 3. The LLRs are mapped into soft symbols, $\tilde{\boldsymbol{x}} \in \mathbb{C}^{N_\mathrm{s}\times 1}$, by applying the formulae from Table 2. Let $\mu_{|\tilde{x}|^2}$ and $\sigma^2_{|\tilde{x}|^2}$ denote the mean and variance of the soft symbol powers $|\tilde{x}_n|^2$, $n = 1, \ldots, N_\mathrm{s}$, respectively. The variance of the averaged samples, $\mathrm{var}\left(N_\mathrm{s}^{-1}\sum_{n=1}^{N_\mathrm{s}}|\tilde{x}_n|^2\right) = \sigma^2_{|\tilde{x}|^2}/N_\mathrm{s}$ [304, Sect. VI–3.1]. When $N_\mathrm{s}\to\infty$, $\mathrm{var}\left(N_\mathrm{s}^{-1}\sum_{n=1}^{N_\mathrm{s}}|\tilde{x}_n|^2\right)\to 0$. Consequently, $N_\mathrm{s}^{-1}\sum_{n=1}^{N_\mathrm{s}}|\tilde{x}_n|^2 \to \mu_{|\tilde{x}|^2}$. Hence, for large N_s, $\hat{\Delta}_\mathrm{a} = N_\mathrm{s}^{-1}\mathrm{tr}\left\{\hat{\boldsymbol{\Delta}}_\mathrm{a}\right\} = \mathrm{avg}\left(\mathbf{1}_{N_\mathrm{s}} - |\tilde{\boldsymbol{x}}|^2\right)$, $|\tilde{\boldsymbol{x}}|^2 = \left[|\tilde{x}_1|^2, \ldots, |\tilde{x}_n|^2, \ldots, \left|\tilde{x}_{N_\mathrm{s}}\right|^2\right]^\mathrm{T}$, provides an accurate mean of the residual interference energy after SIC with respect to I_a.

SISO and uncorrelated SIMO channels

In the case of an uncorrelated SIMO channel, (6) can be rewritten as

$$\hat{\beta} = \frac{1}{K}\sum_{k=1}^{K}\frac{\sum_{i=1}^{N_\mathrm{R}}|\phi_{ik,k}|^2}{\hat{\Delta}_\mathrm{a}\sum_{i=1}^{N_\mathrm{R}}\left|\phi_{ik,k}\right|^2 + \sigma_\eta^2}, \tag{21}$$

where $\phi_{ik,k}$ is the element on the kth column of the ikth row of an $N_\mathrm{R}K \times K$ FD channel matrix $\boldsymbol{\Phi}$. The Fourier transform of a time series is a complex Gaussian, i.e. the real and imaginary parts of $\phi_{ik,k}$ have mean 0 and variance $\sigma^2_{\phi_{ik,k}}/2$. $\left|\phi_{ik,k}\right|^2$ follows an exponential distribution with mean $\sigma^2_{\phi_{ik,k}}$ [305]. $\phi_{ik,k}$ are assumed to have a standard complex Gaussian distribution, i.e. the variance $\sigma^2_{\phi_{ik,k}} = 1$. It follows that the mean and variance of $\left|\phi_{ik,k}\right|^2$ are both 1. Thus, the PDF of $\left|\phi_{ik,k}\right|^2$, $f_{|\phi_{ik,k}|^2}\left(\left|\phi_{ik,k}\right|^2\right) = \exp\left(-\left|\phi_{ik,k}\right|^2\right)$. Let $\theta = \sum_{i=1}^{N_\mathrm{R}}\left|\phi_{ik,k}\right|^2$. The sum of exponentially distributed variables follows the Erlang distribution.[15]

[15]The exponential and Erlang distributions are special cases of the gamma distribution. The PDF of θ, $f_\theta(\theta) = \theta^{N_\mathrm{R}-1}\exp(-\theta)/\Gamma(N_\mathrm{R})$, where $\Gamma(N_\mathrm{R}) = \int_0^\infty z^{N_\mathrm{R}-1}\exp(-z)dz$. Since N_R is a positive integer, $\Gamma(N_\mathrm{R}) = (N_\mathrm{R}-1)!$ $\Gamma(\cdot)$ is known as the gamma function.

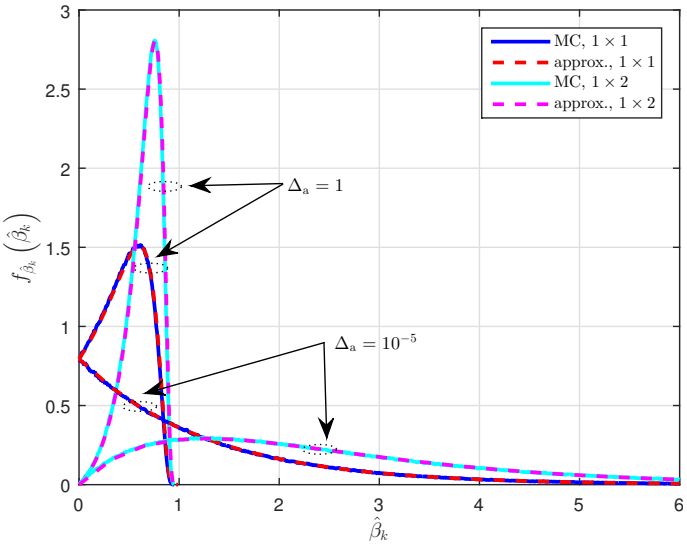

Fig. 4. MC simulated ($2 \cdot 10^6$ samples) and approximated frequency-bin-wise effective SINR distributions at the equaliser output for SISO and uncorrelated 1×2 SIMO channels at $P_{\text{tot}}/\sigma_\eta^2 = -2$ dB.

Knowing the PDF of θ, the PDF of the quotient within the summation in (21), denoted as $\hat{\beta}_k$, becomes

$$f_{\hat{\beta}_k}\left(\hat{\beta}_k\right) = \frac{\sigma_\eta^2}{(1-\hat{\Delta}_a\hat{\beta}_k)^2} \frac{\left(\frac{\hat{\beta}_k\sigma_\eta^2}{1-\hat{\Delta}_a\hat{\beta}_k}\right)^{N_R-1}}{(N_R-1)!} \exp\left(-\frac{\hat{\beta}_k\sigma_\eta^2}{1-\hat{\Delta}_a\hat{\beta}_k}\right). \tag{22}$$

The derivation of (22) is detailed in Appendix 1. The mean $\mathrm{E}\left\{\hat{\beta}_k\right\}$ and variance $\mathrm{var}\left(\hat{\beta}_k\right)$ are obtained from the PDF. A comparison of MC simulated and analytical SINR distributions for SISO and uncorrelated 1×2 SIMO channels at $P_{\text{tot}}/\sigma_\eta^2 = -2$ dB is featured in Fig. 4. In terms of SIC, the two extreme cases are considered. When $\hat{I}_a^{\text{apr}} = 0$, $\hat{\Delta}_a = 1$, and when $\hat{I}_a^{\text{apr}} \to 1$, $\hat{\Delta}_a \to 0$.

Receive correlated MIMO channels

As previously with SISO and uncorrelated SIMO channels, a particular frequency bin is considered. The effective SINR is examined from the perspective of a single TX antenna, as in (6). Let $\mathbf{\Psi}_k \in \mathbb{C}^{N_R \times N_T}$ denote a matrix obtained by collecting the kth diagonals from the submatrices $\mathbf{\Phi}_{i,j}$ in (4). Furthermore, let $\hat{\mathbf{\Delta}}_a \in [0,1]^{N_T \times N_T}$ denote the residual interference energy matrix, whose diagonal values are controlled on a stream-wise basis.

The effective SINR for the jth TX antenna in the kth frequency bin

$$\hat{\beta}_{j,k} = P_j \boldsymbol{\psi}_{k,j}^{\mathrm{H}} \boldsymbol{R}^{\frac{\mathrm{T}}{2}} \left(\sigma_\eta^2 \boldsymbol{I}_{N_\mathrm{R}} + \boldsymbol{R}^{\frac{1}{2}} \boldsymbol{\Psi}_k \hat{\boldsymbol{\Delta}}_\mathrm{a} \boldsymbol{P} \boldsymbol{\Psi}_k^{\mathrm{H}} \boldsymbol{R}^{\frac{\mathrm{T}}{2}} \right)^{-1} \boldsymbol{R}^{\frac{1}{2}} \boldsymbol{\psi}_{k,j} \tag{23}$$

$$= \hat{\Delta}_{\mathrm{a},j}^{-1} \left(1 - \left(1 + \hat{\beta}'_{j,k} \right)^{-1} \right), \tag{24}$$

where

$$\hat{\beta}'_{j,k} = \hat{\Delta}_{\mathrm{a},j} P_j \boldsymbol{\psi}_{k,j}^{\mathrm{H}} \boldsymbol{R}^{\frac{\mathrm{T}}{2}} \left(\sigma_\eta^2 \boldsymbol{I}_{N_\mathrm{R}} + \boldsymbol{R}^{\frac{1}{2}} \boldsymbol{\Psi}_{-j,k} \hat{\boldsymbol{\Delta}}_{\mathrm{a},-j} \boldsymbol{P}_{-j} \boldsymbol{\Psi}_{-j,k}^{\mathrm{H}} \boldsymbol{R}^{\frac{\mathrm{T}}{2}} \right)^{-1} \boldsymbol{R}^{\frac{1}{2}} \boldsymbol{\psi}_{k,j}. \tag{25}$$

$\boldsymbol{\psi}_{k,j} \in \mathbb{C}^{N_\mathrm{R} \times 1}$ denotes the jth column of $\boldsymbol{\Psi}_k$ and $\boldsymbol{\Psi}_{-j,k} \in \mathbb{C}^{N_\mathrm{R} \times N_\mathrm{T}-1}$ is $\boldsymbol{\Psi}_k$ with the jth column removed. $\hat{\Delta}_{\mathrm{a},j}$ denotes the jth diagonal of $\hat{\boldsymbol{\Delta}}_\mathrm{a}$, while $\hat{\boldsymbol{\Delta}}_{\mathrm{a},-j}$ denotes $\hat{\boldsymbol{\Delta}}_\mathrm{a}$ with the jth column and row removed. A detailed derivation of (24) is provided in Appendix 2.

The moment generating function (MGF) of $\hat{\beta}'_{j,k}$ is equivalent to the MGF of the difference of two correlated MIMO mutual information functions [167]. For large N_R and N_T, the mutual information values are asymptotically Gaussian, and therefore their difference is also asymptotically Gaussian. The PDF, which is derived from the MGF, is very robust: it can accommodate different antenna-wise TX powers and RX correlation matrices.

$\hat{\beta}'_{j,k}$ represents a situation where the interference is comprised solely of CAI and/or CCI. Thus, the PDF of $\hat{\beta}'_{j,k}$ is only an intermediate step when the goal is to derive the PDF of $\hat{\beta}_{j,k}$. Utilising the PDF of $\hat{\beta}'_{j,k}$, the PDF of $\hat{\beta}_{j,k}$,

$$\begin{aligned} f_{\hat{\beta}_{j,k}} \left(\hat{\beta}_{j,k} \right) = & \frac{\hat{\Delta}_{\mathrm{a},j}}{\left(1 - \hat{\Delta}_{\mathrm{a},j} \hat{\beta}_{j,k} \right)^2 \sqrt{2\pi}} \cdot \\ & \exp\left(s_0 \left(\frac{1}{1 - \hat{\Delta}_{\mathrm{a},j} \hat{\beta}_{j,k}} - 1 \right) - I_{\mathrm{erg}}(s_0) + I_{\mathrm{erg}}(0) + \frac{v_1(s_0) + v_2(s_0)}{2} \right). \end{aligned} \tag{26}$$

The PDF of $\hat{\beta}'_{j,k}$ and the terms within (26) are detailed in Appendix 3. They are fundamentally the same as those in [167], but due to differences in notation and scaling, they are written out in full. For vertically encoded MIMO, $\hat{\boldsymbol{\Delta}}_\mathrm{a} = \hat{\Delta}_\mathrm{a} \boldsymbol{I}_{N_\mathrm{T}}$ and $\boldsymbol{P} = N_\mathrm{T}^{-1} \boldsymbol{I}_{N_\mathrm{T}}$. Figs. 5 and 6 compare histograms drawn from $2 \cdot 10^6$ samples to the PDFs given by (26). Fig. 5 considers a vertically encoded scenario, where the two TX antennas have equal power and both streams have the same $\hat{\Delta}_\mathrm{a}$. The frequency-bin-wise SINR distribution is seen from the perspective of a single TX antenna. Fig. 6 considers a horizontally encoded 4×4 system. The streams have varying power levels and differing $\hat{\Delta}_{\mathrm{a},j}$ terms corresponding to different levels of *a priori* information arriving from the decoder.

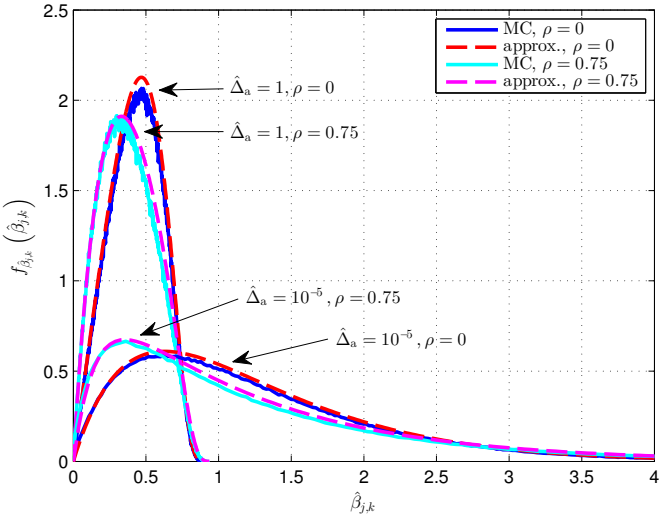

Fig. 5. MC simulated ($2 \cdot 10^6$ samples) and approximated frequency-bin and TX-antenna-wise effective SINR distributions at the equaliser output for a 2×2 MIMO channel at $P_\mathrm{tot}/\sigma_\eta^2 = 1$ dB. $P_j = 1/2$ and $\hat{\Delta}_{\mathrm{a},j} = \hat{\Delta}_\mathrm{a}$, $j = 1, 2$, while ρ was set to 0 and 0.75. ([73], © 2014 IEEE.)

In both cases, the PDFs drawn from (26) closely match the experimentally formed histograms.

It should be noted that the described method can be utilised to form the SINR PDFs for frequency flat SISO and uncorrelated SIMO channels. However, this latter method is slower since s_0 needs to be uniquely solved for each point in the considered SINR range.

4.2.2 Averaged effective SINR distribution

With horizontal encoding, it is necessary to consider the stream-wise effective SINRs, $\hat{\beta}_j$. According to the CLT, the mean of sufficiently many independent random variables approaches the Gaussian distribution, regardless of the distributions of the variables. Thus, $\hat{\beta}_j$ is obtained by averaging $\hat{\beta}_{j,k}$ over the frequency bins. A frequency diversity gain of L is attained [63, Sect. 3.4.2]. Although the number of RX antennas and propagation paths may not be high enough for the CLT to hold tightly, it provides a means for approximating the first and second moments of the distribution. Thus, it

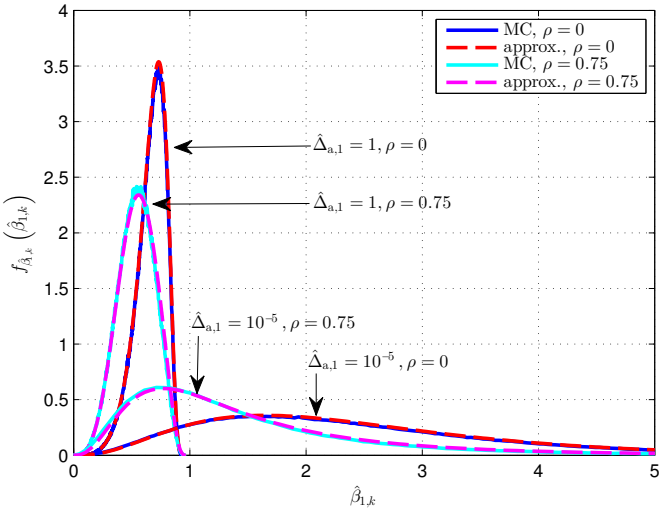

Fig. 6. MC simulated ($2 \cdot 10^6$ samples) and approximated frequency-bin and TX-antenna-wise effective SINR distributions at the equaliser output for a 4×4 MIMO channel at $P_{\text{tot}}/\sigma_\eta^2 = 5$ dB. The power of the considered stream, $P_1 = 0.30$. The power and residual interference energy terms of the interfering streams were $P_2 = 0.40$, $\hat{\Delta}_{\text{a},2} = 0.80$; $P_3 = 0.20$, $\hat{\Delta}_{\text{a},3} = 0.20$ and $P_4 = 0.10$, $\hat{\Delta}_{\text{a},4} = 1$. An uncorrelated and an equicorrelated case with $\rho = 0.75$ were considered. ([73], © 2014 IEEE.)

is assumed that $\hat{\beta}_j \sim \mathcal{N}\left(\mathrm{E}\left\{\hat{\beta}_{j,k}\right\}, \mathrm{var}\left(\hat{\beta}_{j,k}\right)/L\right)$, where $\mathrm{E}\left\{\hat{\beta}_{j,k}\right\}$ and $\mathrm{var}\left(\hat{\beta}_{j,k}\right)$ are obtained from (26) numerically.

With vertical encoding, $\hat{\beta}_{j,k}$ are averaged over the TX antennas and frequency bins. Furthermore, $\hat{\Delta}_{\text{a},j} = \hat{\Delta}_{\text{a}}$ and $P_j = N_{\text{T}}^{-1}$, $\forall j$. Thus, $\mathrm{E}\left\{\hat{\beta}_{j,k}\right\} = \mathrm{E}\left\{\hat{\beta}_k\right\}$, $\forall j$. If there is no spatial correlation, $\mathrm{E}\left\{\hat{\beta}_k\right\}$ has a closed form solution,

$$\mathrm{E}\left\{\hat{\beta}_k\right\} = \frac{\sigma_\eta^2}{4\hat{\Delta}_{\text{a}}^2}\mathcal{F}\left(\frac{N_{\text{R}}\hat{\Delta}_{\text{a}}}{N_{\text{T}}\sigma_\eta^2}, \frac{N_{\text{T}}}{N_{\text{R}}}\right), \tag{27}$$

where $\mathcal{F}(\kappa_1, \kappa_2) = \left(\sqrt{\kappa_1\left(1+\sqrt{\kappa_2}\right)^2+1} - \sqrt{\kappa_1\left(1-\sqrt{\kappa_2}\right)^2+1}\right)^2$. The derivation of (27) is presented in Appendix 4. For RX correlated channels, $\mathrm{E}\left\{\hat{\beta}_k\right\} = \mathrm{E}\left\{\hat{\beta}_{j,k}\right\}$, along with $\mathrm{var}\left(\hat{\beta}_{j,k}\right)$, is derived numerically from (26). In vertically encoded MIMO, averaging is done over the TX antennas as well as frequency bins. Thus, when the CLT is applied, $\hat{\beta} \sim \mathcal{N}\left(\mathrm{E}\left\{\hat{\beta}_k\right\}, \mathrm{var}\left(\hat{\beta}_{j,k}\right)/(N_{\text{T}}L)\right)$.

As can be seen from Figs. 5 and 6, RX correlation does not impact the accuracy of the PDFs. However, the PDFs become less symmetric in the presence of RX correlation,

particularly when $\hat{\Delta}_{\mathrm{a},1} \to 0$. Thus, correlation has a negative impact on the accuracy of $\hat{\beta}_j$ and $\hat{\beta}$, which are assumed to be Gaussian distributed. However, the results in Sect. 4.4 show that the proposed prediction method can withstand moderate RX correlation.

4.3 LLR variance distribution and FER prediction

The variance of the LLRs, $\hat{\sigma}^2_{\mathrm{a},j}$, can be derived from $\hat{\beta}_j$ [120],

$$\hat{\sigma}^2_{\mathrm{a},j} = \frac{4N_{\mathcal{M}}\hat{\beta}_j}{1 - \hat{\Delta}_{\mathrm{a},j}\hat{\beta}_j}, \tag{28}$$

where $N_{\mathcal{M}} = 2$ for real modulations, i.e. BPSK, and $N_{\mathcal{M}} = 1$ for complex modulations, i.e. QPSK and 8-PSK. Since the statistical distribution is considered, the transmission-wise index t has been dropped. The PDF of $\hat{\sigma}^2_{\mathrm{a},j}$ can be derived from $f_{\hat{\beta}_j}\left(\hat{\beta}_j\right)$,

$$f_{\hat{\sigma}^2_{\mathrm{a},j}}\left(\hat{\sigma}^2_{\mathrm{a},j}\right) \approx \frac{4N_{\mathcal{M}}}{(4N_{\mathcal{M}} + \hat{\Delta}_{\mathrm{a},j}\hat{\sigma}^2_{\mathrm{a},j})^2} \frac{1}{\sqrt{2\pi\frac{\mathrm{var}\left(\hat{\beta}_{j,k}\right)}{L}}} \exp\left(- \frac{\left(\frac{\hat{\sigma}^2_{\mathrm{a},j}}{4N_{\mathcal{M}}+\hat{\Delta}_{\mathrm{a},j}\hat{\sigma}^2_{\mathrm{a},j}} - \mathrm{E}\left\{\hat{\beta}_{j,k}\right\}\right)^2}{2\frac{\mathrm{var}\left(\hat{\beta}_{j,k}\right)}{L}} \right). \tag{29}$$

A detailed derivation of (29) is presented in Appendix 5. Once the approximate PDF of $\hat{\sigma}^2_{\mathrm{a},j}$ is known, its mean, $\mathrm{E}\left\{\hat{\sigma}^2_{\mathrm{a},j}\right\}$, and variance, $\mathrm{var}\left(\hat{\sigma}^2_{\mathrm{a},j}\right)$, can be obtained by numerical evaluation. For vertically encoded systems, $f_{\hat{\sigma}^2_{\mathrm{a}}}\left(\hat{\sigma}^2_{\mathrm{a}}\right)$ is derived from $f_{\hat{\beta}}\left(\hat{\beta}\right)$ the same way as in (29). The only difference is that $\mathrm{var}\left(\hat{\beta}_{j,k}/L\right)$ is replaced by $\mathrm{var}\left(\hat{\beta}_{j,k}/(N_{\mathrm{T}}L)\right)$.

When the first two moments of $\hat{\sigma}^2_{\mathrm{a},j}$ are known, familiar distributions can be used to approximate its PDF. It was empirically discovered that the Nakagami distribution [306], which is often chosen to model the fading in wireless multipath channels, e.g. [306, 307], is a reasonably close match of the measured LLR variance distribution at the demapper output.[16] This step is similar to the asymptotic moment matching proposed in [157] and [164], where the MMSE filter's output SINR distribution was approximated by the gamma and Gaussian distributions, respectively. Fig. 8 depicts a comparison of measured and approximated equaliser output LLR variance distributions for SISO and uncorrelated 1×2 SIMO channels at $P_{\mathrm{tot}}/\sigma^2_\eta = -2$ dB, while Fig. 8 features a similar comparison for uncorrelated 2×2 and 4×4 channels with QPSK at $P_{\mathrm{tot}}/\sigma^2_\eta = 1$ dB.

[16] In [70, 71], SISO and uncorrelated SIMO channels, respectively, with equal strength average path gains were assumed. In addition to the Nakagami-approximation, a mixture of the Nakagami and inverse Gaussian distributions was considered. Since the predictions provided by the Nakagami and mixture distributions were close to each other, only the Nakagami-approximation shall be considered in this thesis.

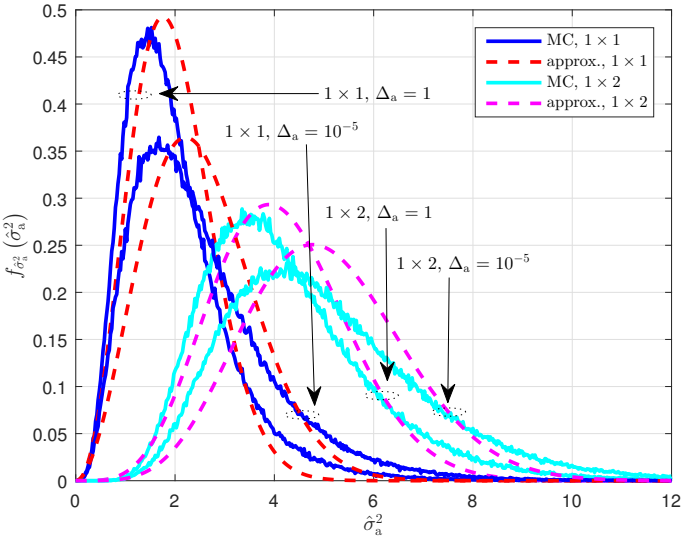

Fig. 7. MC simulated ($4 \cdot 10^5$ samples) and approximated Nakagami distributions of the variances of the equaliser output LLRs for SISO and uncorrelated $1{\times}2$ SIMO channels with QPSK at $P_{\mathrm{tot}}/\sigma_\eta^2 = -2$ dB.

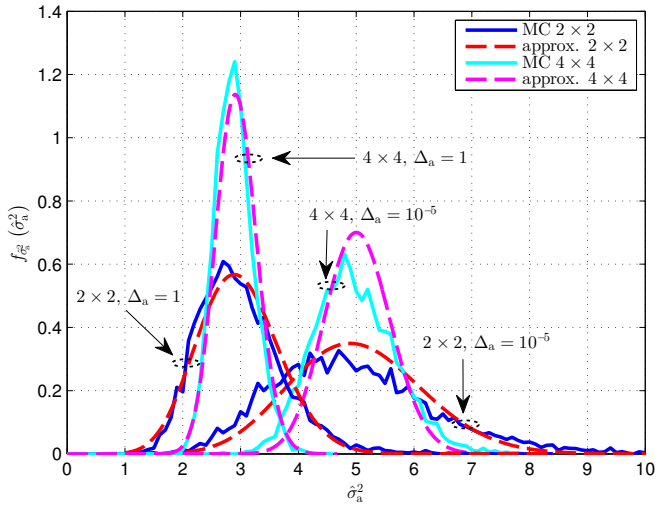

Fig. 8. MC simulated ($4 \cdot 10^5$ samples) and approximated Nakagami distributions of the variances of the equaliser output LLRs for uncorrelated 2×2 and 4×4 channels with QPSK. $P_{\mathrm{tot}}/\sigma_\eta^2 = 1$ dB, $P_j = 1/N_{\mathrm{T}}$ and $\hat{\Delta}_{\mathrm{a},j} = \hat{\Delta}_{\mathrm{a}}$, $\forall j$. (Modified from [73], © 2014 IEEE.)

By using $\tilde{\sigma}^2_{\mathrm{a},j} + \tilde{\epsilon}_{\mathrm{a},j}$ from (19) as the boundary value, the Nakagami distribution's CDF is used to estimate the probability that the equaliser and decoder charts of the jth stream intersect given any $\hat{\boldsymbol{I}}^{\mathrm{apr}}_{\mathrm{a}}$,

$$\mathcal{P}^{\epsilon}_{j}\left(\hat{\boldsymbol{I}}^{\mathrm{apr}}_{\mathrm{a}}\right) = \frac{\gamma\left(m, \frac{m}{\Omega}\left(\tilde{\sigma}^2_{\mathrm{a},j} + \tilde{\epsilon}_{\mathrm{a},j}\right)^2\right)}{\Gamma(m)}, \tag{30}$$

where the shape, m, and spread, Ω, parameters[17] are derived by using $\mathrm{E}\left\{\hat{\sigma}^2_{\mathrm{a},j}\right\}$ and $\mathrm{var}\left(\hat{\sigma}^2_{\mathrm{a},j}\right)$ obtained from (29), and $\gamma(\cdot,\cdot)$ denotes the lower incomplete gamma function[18]. The next step is to develop expressions for approximate FER in vertically and horizontally encoded systems [57].

4.3.1 FER approximation for vertically encoded transmission with RR-HARQ

For vertically encoded or SISO/SIMO systems, where the decoder operates on a single stream, the approximate FER,

$$\widetilde{\mathrm{FER}} = \max_{\hat{I}^{\mathrm{apr}}_{\mathrm{a}} \in [0,1)} \mathcal{P}^{\epsilon}\left(\hat{I}^{\mathrm{apr}}_{\mathrm{a}}\right). \tag{31}$$

The vertically encoded scenario is complemented by the inclusion of RR-HARQ. In block fading channels there is no correlation between bit-wise LLRs of successive retransmissions. Even in quasi-static channels, bit-wise correlation can be reduced by applying alternating interleaver patterns between time slots. By performing RR, as in (11), the convergence condition becomes

$$\hat{\sigma}^2_{\mathrm{a}}(w) + \sum_{t=1}^{w-1} \hat{\sigma}^2_{\mathrm{a},t}(t) \geq \tilde{\sigma}^2_{\mathrm{a}} + \tilde{\epsilon}_{\mathrm{a}}, \quad \forall \hat{\sigma}^2_{\mathrm{a}}(w)\,; w \geq 2, \tag{32}$$

where $\hat{\sigma}^2_{\mathrm{a}}(w)$ denotes the LLR variance at the equaliser output during the wth transmission of the packet, given equaliser *a priori* information $\hat{I}^{\mathrm{apr}}_{\mathrm{a}}$. $\hat{\sigma}^2_{\mathrm{a},t}(t)$ denotes the demapper output's LLR variance at the intersection of the equaliser and decoder charts for the tth transmission. Due to the slopes of the graphs (see Fig. 10), the intersection is

[17] $m = \frac{\left(\mathrm{E}\left\{\left(\hat{\sigma}^2_{\mathrm{a}}\right)^2\right\}\right)^2}{\mathrm{var}\left(\left(\hat{\sigma}^2_{\mathrm{a},j}\right)^2\right)}$, $\Omega = \mathrm{E}\left\{\left(\hat{\sigma}^2_{\mathrm{a},j}\right)^2\right\}$.

[18] $\gamma(\kappa_1, \kappa_2) = \int_0^{\kappa_2} z^{\kappa_1 - 1} \exp(-z)\, dz$.

likely to take place close to the left edge of the chart. Thus, (32) is approximated as

$$\hat{\sigma}_{\mathrm{a}}^2(w) + \sum_{t=1}^{w-1} \hat{\sigma}_0^2(t) \geq \tilde{\sigma}_{\mathrm{a}}^2 + \tilde{\epsilon}_{\mathrm{a}}, \quad \forall \hat{\sigma}_{\mathrm{a}}^2(w); w \geq 2, \tag{33}$$

where $\hat{\sigma}_0^2(t) = \left[J^{-1}\left(\hat{g}\left(\hat{I}_{\mathrm{a}}^{\mathrm{apr}} = 0; \breve{\boldsymbol{R}}^{\frac{1}{2}} \boldsymbol{H}(t) \breve{\boldsymbol{P}}^{\frac{1}{2}}\right)\right)\right]^2$. Since $\hat{\sigma}_{\mathrm{a}}^2(t)$ were assumed to be IID $\forall t$, the mean and variance of the combined LLR variances on the left-hand side of the inequality in (33),

$$\mathrm{E}\left\{\hat{\sigma}_{\mathrm{a,RR}_w}^2\right\} = \mathrm{E}\left\{\hat{\sigma}_{\mathrm{a}}^2\right\} + (w-1)\,\mathrm{E}\left\{\hat{\sigma}_0^2\right\}, \tag{34a}$$

$$\mathrm{var}\left(\hat{\sigma}_{\mathrm{a,RR}_w}^2\right) = \mathrm{var}\left(\hat{\sigma}_{\mathrm{a}}^2\right) + (w-1)\,\mathrm{var}\left(\hat{\sigma}_0^2\right), \tag{34b}$$

Figs. 9 and 10 depict the measured and predicted ergodic equaliser *a posteriori* information transfer charts for a spatially uncorrelated 1×4 SIMO channel and a 4×4 exponentially RX correlated ($\rho = 0.50$) 4×4 MIMO channel, respectively. The SNRs of the SIMO and MIMO channels were -9 dB and -2 dB, respectively. The Proakis-C channel model was used in both cases. The measured equaliser charts were obtained by MC simulations, where 1000 packets were transmitted and then retransmitted, with each one arriving through a unique channel realisation. The predicted LLR variances at the output of the equaliser were obtained from (34a), after which the J-function was used to transport them to the mutual information domain. The turbo decoder EXIT chart for the code rate $R_{\mathrm{c}} = 1/2$ is also included for reference.

It is worth noting that the equaliser charts in Fig. 10 have a steeper slope than those in Fig. 9. This is due to the fact that the MIMO channel introduces CAI, which can be cancelled out. In SISO and SIMO systems, the interference is entirely made up of ISI. Thus, MIMO systems gain more from SIC than SISO/SIMO systems. Although the ergodic equaliser charts do not reveal anything about the LLR variance distribution, they can be used to deduce that, at the considered SNRs and with $R_{\mathrm{c}} = 1/2$, two retransmissions are required before an FER of $1/2$, or slightly smaller, is attained.

For the more complex combining option from (12), where all previously received versions of the packet, along with the latest version, are separately equalised during each global iteration, the mean and variance of the summations on the left-hand side of (33) become

$$\mathrm{E}\left\{\hat{\sigma}_{\mathrm{a,RR}_w}^2\right\} = w\mathrm{E}\left\{\hat{\sigma}_{\mathrm{a}}^2\right\}, \tag{35a}$$

$$\mathrm{var}\left(\hat{\sigma}_{\mathrm{a,RR}_w}^2\right) = w\mathrm{var}\left(\hat{\sigma}_{\mathrm{a}}^2\right). \tag{35b}$$

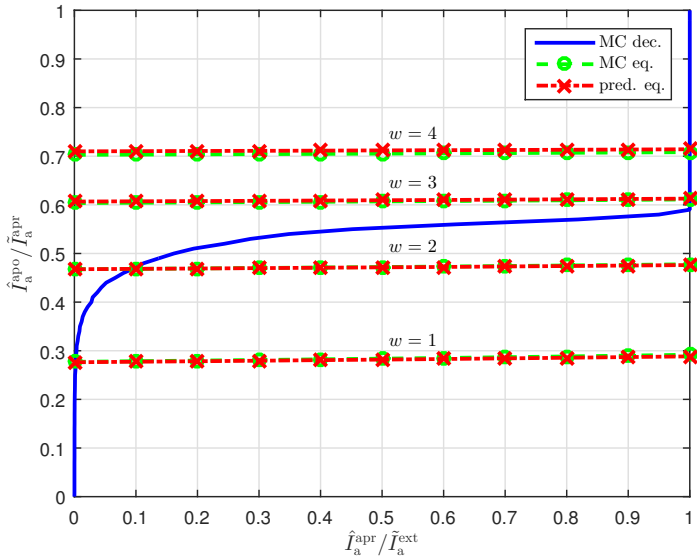

Fig. 9. The measured and predicted ergodic equaliser transfer charts of the initial transmission and three retransmissions for a spatially uncorrelated 1×4 Proakis-C multipath channel with QPSK at an SNR of -9 dB, and the turbo decoder EXIT chart for $R_{\mathrm{c}} = 1/2$.

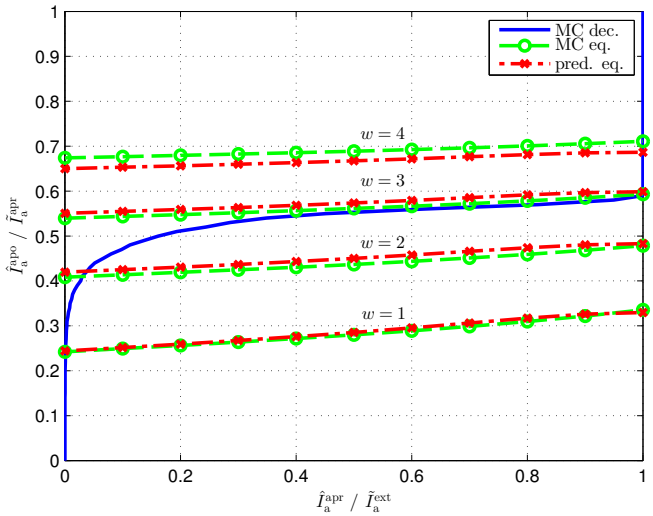

Fig. 10. The measured and predicted ergodic equaliser transfer charts of the initial transmission and three retransmissions for a 4×4 Proakis-C multipath channel with exponential RX correlation, $\rho = 0.50$, and QPSK, with SNR -2 dB, and the turbo decoder EXIT chart for $R_{\mathrm{c}} = 1/2$. ([73], © 2014 IEEE.)

The accumulation of the LLR variances in (34a), (34b), (35a) and (35b) can be traced back to the SNR accumulation, which was already demonstrated in [215].

4.3.2 FER approximation for horizontally encoded transmission

In the case of a horizontally encoded or an MU-MIMO transmission, the FER of a particular stream depends on the degree of cancellation of the parallel streams. In order to simplify the computations, only the extreme cases are considered, i.e. $\hat{\Delta}_{\mathrm{a},j'} = 1$ and $\hat{\Delta}_{\mathrm{a},j'} \to 0, \forall j' \neq j$. Assume the following definitions,

$$\dot{\mathcal{P}}_1^{\epsilon}\left(\hat{I}_{\mathrm{a},1}^{\mathrm{apr}} \,\middle|\, \hat{\boldsymbol{I}}_{\mathrm{a}}^{\mathrm{apr}} \backslash \hat{I}_{\mathrm{a},1}^{\mathrm{apr}}\right) = \max_{\hat{I}_{\mathrm{a},1}^{\mathrm{apr}} \in [0,1)} \mathcal{P}_1^{\epsilon}\left(\hat{I}_{\mathrm{a},1}^{\mathrm{apr}} \,\middle|\, \hat{\boldsymbol{I}}_{\mathrm{a}}^{\mathrm{apr}} \backslash \hat{I}_{\mathrm{a},1}^{\mathrm{apr}}\right), \tag{36a}$$

$$\ddot{\mathcal{P}}_j^{\epsilon}\left(\hat{I}_{\mathrm{a},1}^{\mathrm{apr}}, \hat{I}_{\mathrm{a},j}^{\mathrm{apr}} \,\middle|\, \hat{\boldsymbol{I}}_{\mathrm{a}}^{\mathrm{apr}} \backslash \left\{\hat{I}_{\mathrm{a},1}^{\mathrm{apr}}, \hat{I}_{\mathrm{a},j}^{\mathrm{apr}}\right\}\right) = \max_{\substack{\hat{I}_{\mathrm{a},1}^{\mathrm{apr}} \in [0,1) \\ \hat{I}_{\mathrm{a},j}^{\mathrm{apr}} \in [0,1)}} \mathcal{P}_j^{\epsilon}\left(\hat{I}_{\mathrm{a},1}^{\mathrm{apr}}, \hat{I}_{\mathrm{a},j}^{\mathrm{apr}} \,\middle|\, \hat{\boldsymbol{I}}_{\mathrm{a}}^{\mathrm{apr}} \backslash \left\{\hat{I}_{\mathrm{a},1}^{\mathrm{apr}}, \hat{I}_{\mathrm{a},j}^{\mathrm{apr}}\right\}\right). \tag{36b}$$

The FER is calculated by forming a trellis of all the possible outcomes the iterative receiver can produce. In the simplest case of two spatial streams, the approximate FER of the first stream,

$$\begin{aligned}\widetilde{\mathrm{FER}}_1 = &\left[1 - \ddot{\mathcal{P}}_2^{\epsilon}\left(\hat{I}_{\mathrm{a},1}^{\mathrm{apr}}, \hat{I}_{\mathrm{a},2}^{\mathrm{apr}}\right)\right] \dot{\mathcal{P}}_1^{\epsilon}\left(\hat{I}_{\mathrm{a},1}^{\mathrm{apr}} \,\middle|\, \hat{I}_{\mathrm{a},2}^{\mathrm{apr}} \to 1\right) + \\ &\ddot{\mathcal{P}}_2^{\epsilon}\left(\hat{I}_{\mathrm{a},1}^{\mathrm{apr}}, \hat{I}_{\mathrm{a},2}^{\mathrm{apr}}\right) \dot{\mathcal{P}}_1^{\epsilon}\left(\hat{I}_{\mathrm{a},1}^{\mathrm{apr}} \,\middle|\, \hat{I}_{\mathrm{a},2}^{\mathrm{apr}} = 0\right).\end{aligned} \tag{37}$$

For $\widetilde{\mathrm{FER}}_2$, the stream-wise indices are flipped. The approximate FER formulae for three and four parallel spatial streams can be found in Appendix 6.

4.4 Numerical results

Some fundamental parameters that were used throughout all the presented simulations, also in Sect. 5.3, are listed in Table 4. Ideal error detection was assumed, while the turbo decoder utilised the linear-log-MAP approximation [81].

4.4.1 SISO and uncorrelated SIMO channels

Figs. 11 and 12 consider uncorrelated Proakis-B[19] and Proakis-C SISO channels, respectively. In both cases, 8-PSK, $R_{\mathrm{c}} = 1/3$ and three retransmissions were assumed. In the predictions, the gamma distribution approximation from Sect. 4.2.1 was utilised

[19] The statistical average amplitudes of the impulse responses, $\boldsymbol{\xi} = [0.407, 0.815, 0.407]$ [193, Fig. 10.2-5(b)].

Table 4. Main simulation parameters (Modified from [73], © 2014 IEEE.)

Simulation parameter	Value
Multipath channel model	Proakis-B, Proakis-C
Modulation	BPSK, QPSK, 8-PSK
Mapping	Gray
DFT length, K	512
Channel code	3GPP turbo code [64]
Rate matching	3GPP rate matching [64]
Decoder iterations	6
Global iterations, N_d	6
ϵ, from (17)	0.02
Transmitted packets	10^5

to evaluate the effective SINR distribution at a random frequency bin. As was pointed out at the end of Sect. 4.2.1, the more general method that is used to approximate the effective SINR distributions of MIMO channels can also be used to approximate the SINR distributions of SISO and uncorrelated SIMO channels. However, the gamma distribution method is computationally faster. The two different RR-HARQ combining options from (11) and (12) are also considered. As the interference is solely comprised of ISI, noise is the dominant term in the effective SINR. Thus, there is relatively little gain to be had from the equalisation of all the transmitted blocks. The FER graph of the initial transmission is taken from the simpler MC simulation case, where the receiver equalises only the latest received packet. Since the differences between the schemes only become apparent with retransmissions, the FER graphs of the initial transmission would effectively overlap.

In Fig. 11 there is occasionally a 1 dB separation between the predicted and simulated FER graphs of the initial transmission, while in Fig. 12 the curves almost overlap. This is due to the difference in the number of separable channel taps. The Proakis-B channel model has three taps, while the Proakis-C model has five. When there are more channel taps, the frequency diversity increases and the CLT approximation made in Sect. 4.2.2 holds more tightly. Thus, from the prediction perspective, scenarios where there are only two or three separable channel taps are particularly difficult. For flat fading channels, the CLT need not be invoked. It can also be noted that the receiver performs slightly more effectively with the Proakis-C channel than with the Proakis-B channel. This gain, which for much of the time remains slightly below 1 dB, can be attributed to the increase in frequency diversity.

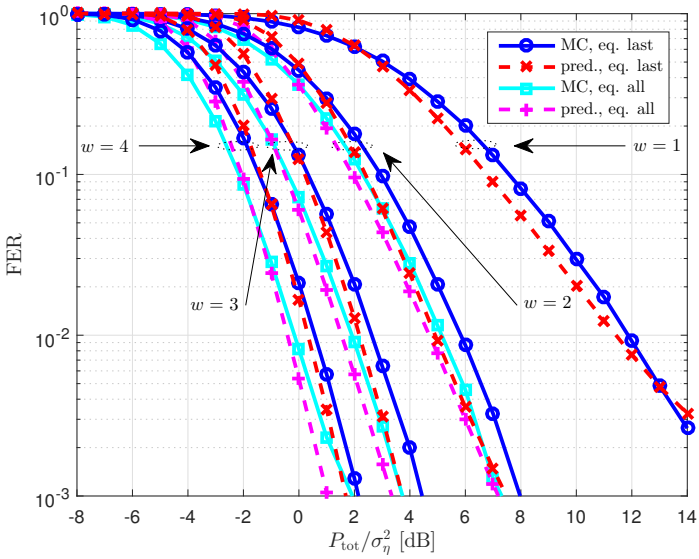

Fig. 11. The measured and predicted FERs of the initial transmission and three RR-HARQ retransmissions assuming the equalisation of only the latest transmitted packet or all the transmitted packets. An uncorrelated SISO Proakis-B channel with 8-PSK and $R_{\mathrm{c}} = 1/3$ was considered.

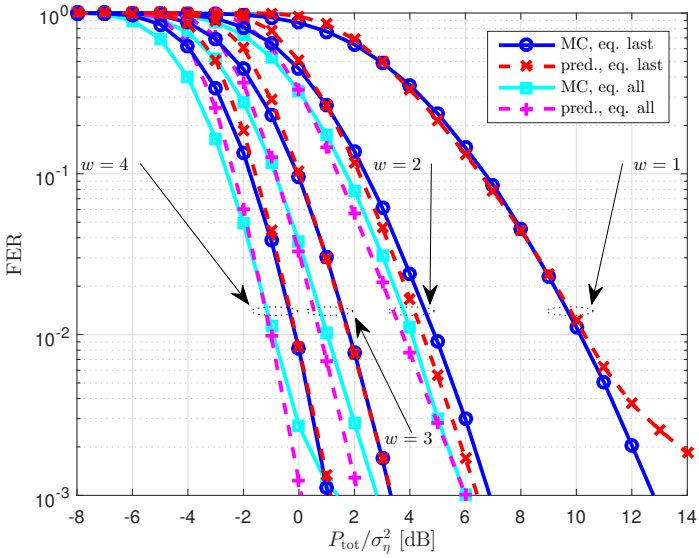

Fig. 12. The measured and predicted FERs of the initial transmission and three RR-HARQ retransmissions assuming the equalisation of only the latest transmitted packet or all the transmitted packets. An uncorrelated SISO Proakis-C channel with 8-PSK and $R_{\mathrm{c}} = 1/3$ was considered.

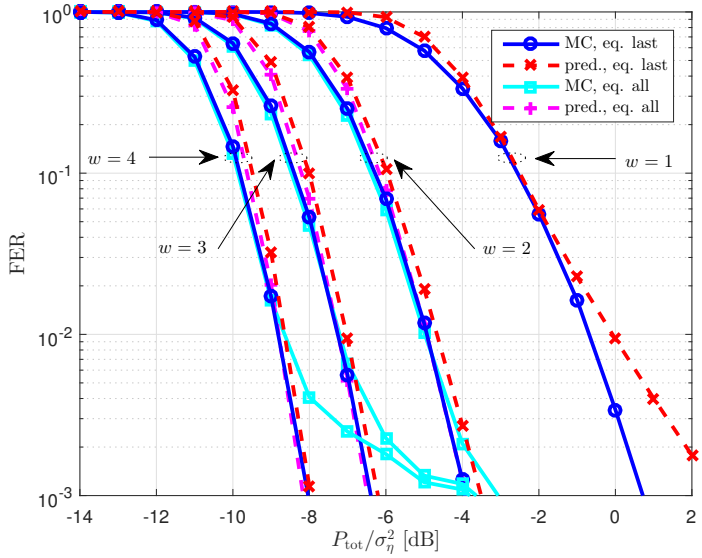

Fig. 13. The measured and predicted FERs of the initial transmission and three RR-HARQ retransmissions assuming the equalisation of only the latest transmitted packet or all the transmitted packets. An uncorrelated 1×4 Proakis-B SIMO channel with QPSK and $R_\mathrm{c} = 1/2$ was considered.

1×4 Proakis-B and Proakis-C SIMO channels, with QPSK, $R_\mathrm{c} = 1/2$ and three retransmissions, were considered in Figs. 13 and 14, respectively. In both figures, fairly large discrepancies can be observed between the measurements and predictions in the high FER region. In terms of SNR, the differences can be almost 1 dB. Nevertheless, the proposed method accurately predicts the positions of the turbo cliffs.

By comparing Figs. 11 and 12 to Figs. 13 and 14, one can examine the significance of the channel delay profile. In Fig. 11, which assumed a Proakis-B SISO channel, a 1 dB gap could be occasionally seen between the measured and predicted FER graphs of the initial transmission. In Fig. 12, which assumed a Proakis-C SISO channel, the corresponding graphs were closely matched. When four RX antennas are involved, the channel delay profile becomes less of a factor. In Fig. 13 the measured and predicted FER graphs start to diverge at 10^{-2}, but above that point the prediction has approximately the same level of accuracy as the prediction in Fig. 14. This can be traced back to the CLT approximation made in Sect. 4.2.2. It could already be seen from Fig. 4 that the effective SINR distributions have "more Gaussian" shapes when two RX antennas are involved. Thus, when the involved frequency-bin-wise effective SINR distributions are more Gaussian, the CLT approximation holds more tightly.

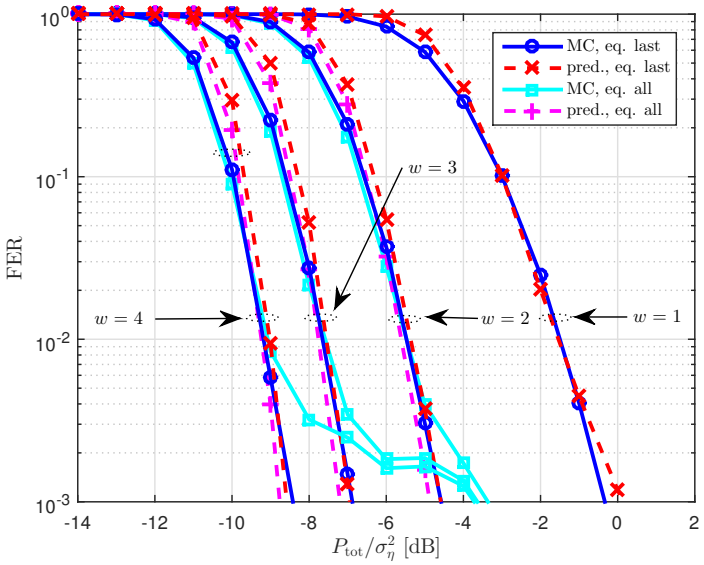

Fig. 14. The measured and predicted FERs of the initial transmission and three RR-HARQ retransmissions assuming the equalisation of only the latest transmitted packet or all the transmitted packets. An uncorrelated 1×4 Proakis-C SIMO channel with QPSK and $R_{\mathrm{c}} = 1/2$ was considered.

Like previously in the SISO case, the receiver benefits from a more frequency-selective channel. However, when spatial diversity is introduced, the impact of frequency diversity is reduced. This time, the added frequency diversity brings less than a 0.5 dB gain. As before, relatively little gain is to be had from the equalisation of all transmitted packets. In fact, the more complex equalisation scheme seems to suffer performance degradation at low FERs.

4.4.2 Vertically encoded MIMO transmission

A vertically encoded 2×2 scenario, with the Proakis-C channel, $\rho = 0.50$, 8-PSK, $R_{\mathrm{c}} = 1/3$ and three RR-HARQ retransmissions is considered in Fig. 15. Since a second TX antenna is introduced, the effective SINR PDF from (26) is utilised in the prediction. The inclusion of a second TX antenna also means that the interference is now composed of ISI and CAI. Hence, unlike in the case of a single TX antenna, the receiver experiences a noticeable, approximately 1 dB gain from the iterative equalisation of each transmitted packet. Like in the preceding section, the FER graph of the initial

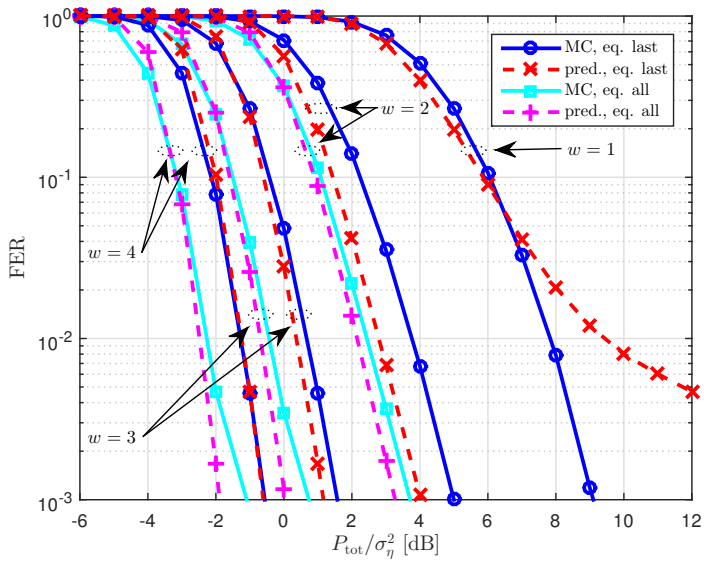

Fig. 15. The measured and predicted FERs of the initial transmission and three RR-HARQ retransmissions assuming the equalisation of only the latest transmitted packet or all the transmitted packets. A 2×2 Proakis-C channel with $\rho = 0.50$, 8-PSK and $R_{\mathrm{c}} = 1/3$ was considered. (Modified from [73], © 2014 IEEE.)

transmission is drawn from the simulation data involving the simpler RR-HARQ option, where only the latest version of the packet was equalised.

4.4.3 Horizontally encoded MIMO transmission

Fig. 16 depicts the FERs of a horizontally encoded scenario, where two TX antennas were employed and the Proakis-C channel model was assumed. The first stream employed $P_1 = 2/3$, 8-PSK and $R_{\mathrm{c},1} = 1/3$, while the second stream employed $P_2 = 1/3$, QPSK and $R_{\mathrm{c},2} = 1/2$. The FERs for $N_{\mathrm{R}} = 2$ and $N_{\mathrm{R}} = 3$ are depicted, and $\boldsymbol{R} = \boldsymbol{I}_{N_{\mathrm{R}}}$. The parameters are otherwise the same in Fig. 17, but exponential RX correlation, with $\rho = 0.70$, was introduced. For $N_{\mathrm{R}} = 2$, this is equivalent to equicorrelation. It can be inferred from Fig. 17 that the prediction method can take into account moderate RX correlation.

Figs. 18 and 19 depict the FERs of a horizontally encoded 4×4 system, where the Proakis-B and Proakis-C channel models were considered, respectively. In both cases, exponential RX correlation, with $\rho = 0.70$, was assumed. Different TX powers,

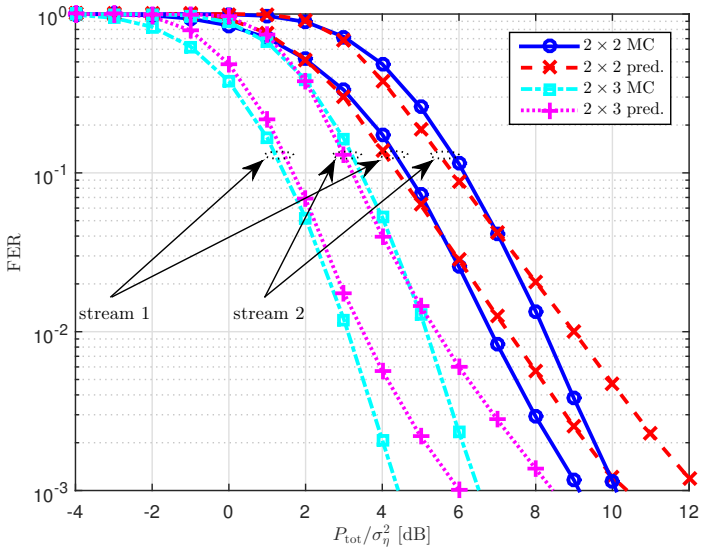

Fig. 16. The measured and predicted FERs of horizontally encoded transmission in uncorrelated 2×2 and 2×3 Proakis-C channels. Stream 1 employed $P_1 = 2/3$, 8-PSK and $R_{\mathrm{c},1} = 1/3$, while stream 2 employed $P_2 = 1/3$, QPSK and $R_{\mathrm{c},2} = 1/2$. (Modified from [73], © 2014 IEEE.)

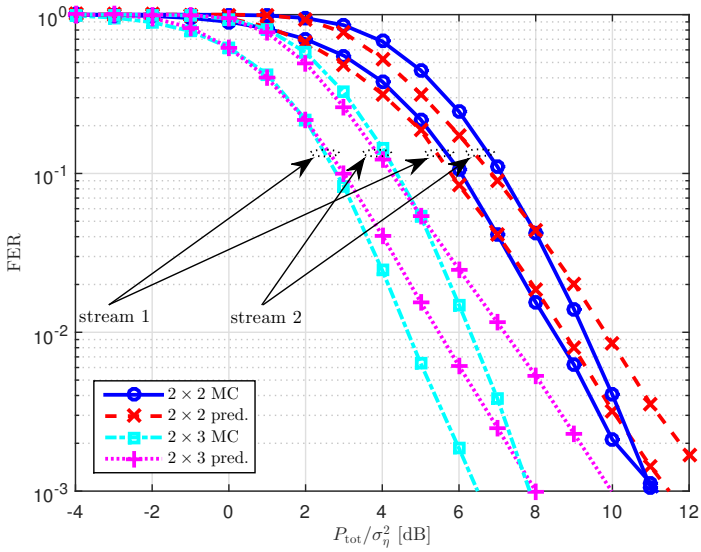

Fig. 17. The measured and predicted FERs of horizontally encoded transmission in exponentially RX correlated 2×2 and 2×3 Proakis-C channels, with $\rho = 0.70$. Stream 1 employed $P_1 = 2/3$, 8-PSK and $R_{\mathrm{c},1} = 1/3$, while stream 2 employed $P_2 = 1/3$, QPSK and $R_{\mathrm{c},2} = 1/2$. (Modified from [73], © 2014 IEEE.)

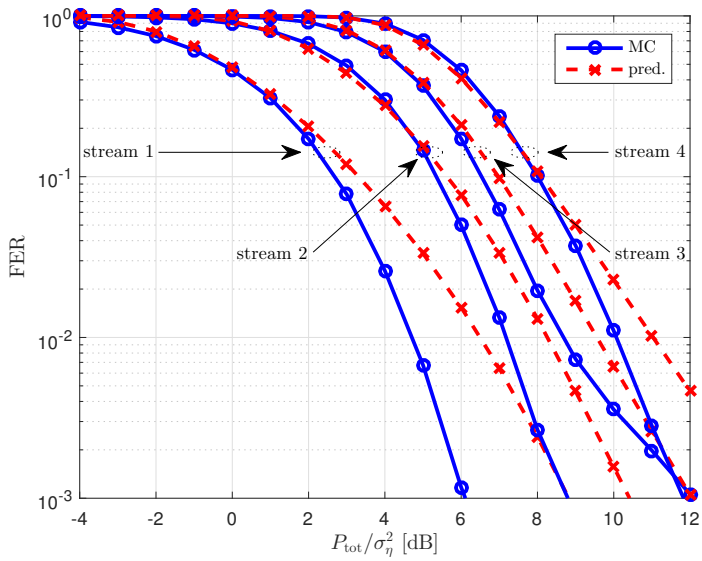

Fig. 18. The measured and predicted FERs of a horizontally encoded transmission in an exponentially RX correlated 4×4 **Proakis-B channel, with** $\rho = 0.70$**. Stream** 1 **employed** $P_1 = 0.20$**, BPSK and** $R_{\mathrm{c},1} = 1/3$**; stream** 2 **employed** $P_2 = 0.35$**, QPSK and** $R_{\mathrm{c},2} = 1/2$**; stream** 3 **employed** $P_3 = 0.30$**, 8-PSK and** $R_{\mathrm{c},3} = 2/5$**; while stream** 4 **employed** $P_4 = 0.15$**, QPSK and** $R_{\mathrm{c},4} = 3/5$**.**

code rates and modulations were assigned for each stream: $P_1 = 0.20$, BPSK and $R_{\mathrm{c},1} = 1/3$ for stream 1, $P_2 = 0.35$, QPSK and $R_{\mathrm{c},2} = 1/2$ for stream 2, $P_3 = 0.30$, 8-PSK and $R_{\mathrm{c},3} = 2/5$ for stream 3, and $P_4 = 0.15$, QPSK and $R_{\mathrm{c},4} = 3/5$ for stream 4. The stream-wise turbo cliffs occur at different SNR ranges. At high SNRs, the "weaker" streams benefit from the equaliser's ability to cancel out the interference caused by the "stronger" streams.[20] Therefore, the FER curves are relatively tightly grouped.

As was already noted in Sect. 4.4.1 with SISO channels (Figs. 11 and 12), the CLT approximation in the prediction procedure holds more tightly when the number of channel taps increases. In Fig. 19, the differences between the simulated and predicted curves remain smaller than 1 dB even with FERs as low as 10^{-2}. In Fig. 18, the simulated and predicted curves are closely matched at FER 10^{-1}. However, at 10^{-2}, the differences are more pronounced than in the Proakis-C scenario. For the first stream, the difference at this point is approximately 2 dB, and approximately 1 dB for the other streams. Like previously in the uncorrelated 1×4 scenario (Figs. 13 and 14), the frequency diversity

[20]The terms "weak" and "strong" refer to the receiver's capability of recovering the stream-wise data, which factors in the modulation and coding, in addition to the stream-wise power.

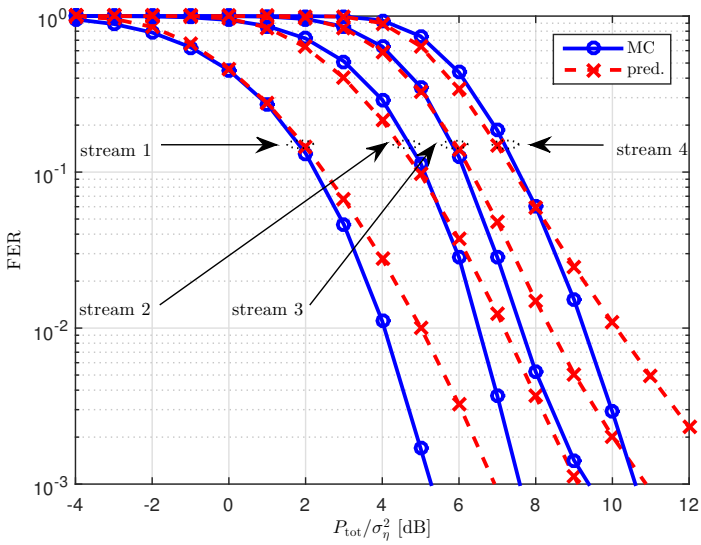

Fig. 19. The measured and predicted FERs of a horizontally encoded transmission in an exponentially RX correlated 4×4 **Proakis-C channel, with** $\rho = 0.70$**. Stream** 1 **employed** $P_1 = 0.20$**, BPSK and** $R_{\mathrm{c},1} = 1/3$**; stream** 2 **employed** $P_2 = 0.35$**, QPSK and** $R_{\mathrm{c},2} = 1/2$**; stream** 3 **employed** $P_3 = 0.30$**, 8-PSK and** $R_{\mathrm{c},3} = 2/5$**; while stream** 4 **employed** $P_4 = 0.15$**, QPSK and** $R_{\mathrm{c},4} = 3/5$**. (Modified from [73], © 2014 IEEE.)**

gain between the Proakis-B and Proakis-C channel models is usually slightly below 0.5 dB.

Fig. 20 assumes the Proakis-C channel model and the exact same stream-wise parameters as before, but in this case the receiver is linear and does not perform iterative SIC. Therefore, the FER curves are not as tightly grouped as in Fig 19. The performance of the strongest stream is approximately the same in both scenarios. The weakest streams are the biggest beneficiaries from SIC.

As was noted in Sect. 4.3.2, the FER prediction for horizontally encoded transmission does not take into account SIC—only the extreme cases of no cancellation and near full cancellation. Also, a prediction error for a single stream negatively impacts the prediction accuracy of the adjoining streams. Nevertheless, in Figs. 16, 17 and 19, which assumed the Proakis-C channel, there is a smaller than 1 dB difference between the predicted and MC simulation results even down to FER levels of 10^{-2}. It should also be noted that for SISO/SIMO and vertically encoded MIMO scenarios, such accuracy is sometimes maintained with FERs even below that point.

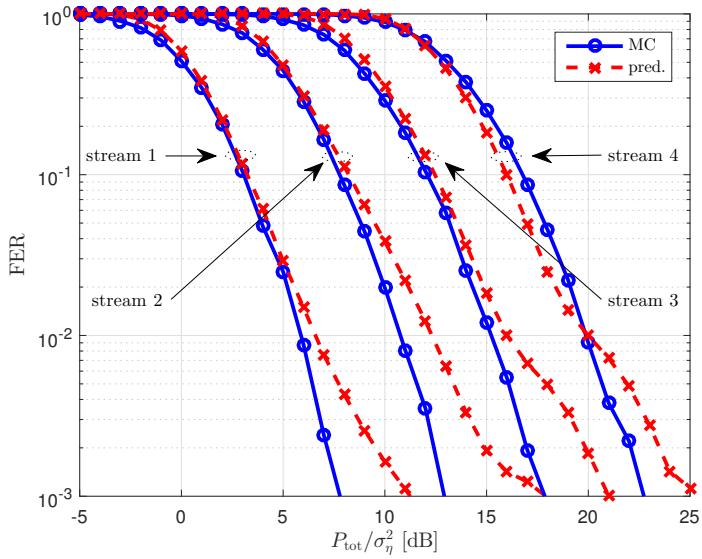

Fig. 20. The measured and predicted FERs of a horizontally encoded transmission in an exponentially RX correlated 4×4 **Proakis-C channel for a linear receiver, with** $\rho = 0.70$**. Stream** 1 **employed** $P_1 = 0.20$**, BPSK and** $R_{\text{c},1} = 1/3$**; stream** 2 **employed** $P_2 = 0.35$**, QPSK and** $R_{\text{c},2} = 1/2$**; stream** 3 **employed** $P_3 = 0.30$**, 8-PSK and** $R_{\text{c},3} = 2/5$**; while stream** 4 **employed** $P_4 = 0.15$**, QPSK and** $R_{\text{c},4} = 3/5$**. (Modified from [73], © 2014 IEEE.)**

4.5 Summary and discussion

This chapter has demonstrated how the mutual information transfer charts can be used to extend conventional system performance analysis from uncoded linear receivers to iterative receivers that employ FEC and HARQ techniques. By evaluating the SINR distribution at the output of an FD-SIC-MMSE equaliser, it is possible to approximate the LLR variance distribution at the input of a turbo decoder. By comparing that distribution to a fixed boundary value, which is set by the decoder's EXIT chart, an approximate FER is obtained. The scheme is robust and can be applied to horizontally and vertically encoded transmissions. In the case of horizontal encoding, the parallel streams may have different powers and employ different code rates and levels of PSK. This scenario is similar to an MU-MIMO set-up, assuming that the user-wise channels contain the same number of channel taps. Since the LLR distributions are considered on a stream-by-stream basis, the prediction method can take into account delay profiles with different numbers of taps. For vertically encoded transmissions, backward error control in the form of RR-HARQ was also considered.

The proposed prediction method shares no common operational blocks with the system simulation model. Only the computation of the decoder EXIT charts require MC computer simulations, but those can be performed off-line. Nevertheless, the prediction method can take into account several different parameters and still produce FER graphs that are close to the simulated graphs, even with FERs as low as 10^{-2}. Although simple RX correlation models were assumed, the equations in Appendix 3 demonstrate that the PDF of the effective SINR only requires the eigenvalues of the RX correlation matrix.

When a single RX antenna and few channel taps are assumed, the prediction method is susceptible to error. The predictions become more reliable when a second RX antenna is added or a more frequency-selective channel is considered. Numerical computer simulations suggest that the prediction method is reasonably accurate for a tapped delay line model with three separable taps. In general, the difference between the simulated and predicted FER curves is very small in the $P_{\text{tot}}/\sigma_\eta^2$ domain above FER levels of 10^{-1}. Even at 10^{-2}, the difference is usually smaller than 1 dB. At such low FERs, the difference would be almost negligible in terms of throughput. In the high FER region, the difference between the simulation and prediction can be larger than 10^{-1}. Due to the logarithmic scaling and the steepness of the turbo cliffs, the differences are not always evident. The differences are explained by the fact that the LLR variance distribution does not actually follow the Nakagami distribution, which is only a convenient approximation. The prediction method can take into account moderate RX correlation. With heavily correlated channels, the accuracy is decreased.

At high SNRs, above 10 dB, the means and variances of the considered distributions become very large. This makes it more difficult to numerically evaluate the associated integrals both quickly and accurately. An accurate numerical integration combines a wide integration interval with dense sampling, which quickly increases the number of computations. The reason why some of the predicted FER curves behave aberrantly at high SNRs is probably due to inaccurately evaluated integrals.

The proposed method is not advocated as a complete substitute for detailed MC computer simulations. The prediction method is computationally much faster than the detailed simulation model to which it was compared. Thus, in some cases the proposed semi-analytical performance prediction method can be a useful tool when analysing the behaviour of complex iterative receivers. While it took the MC simulator days, or even a couple of weeks with the RR-HARQ simulations, to produce results, it took the prediction method only hours, or seconds in the case of SISO and uncorrelated SIMO channels, to provide the corresponding results.

5 Link adaptation

The channel model, as described in Sect. 3.1, assumed that the channel coefficients remain constant within a transmitted block, but are independent between blocks. Therefore, instantaneous effective SINR would not provide reliable CSI. Hence, statistical LA schemes are needed. Sect. 4.1 established how the mutual information transfer charts can be used to predict the performance of an iterative receiver. In a change of perspective, the positions of the equaliser and decoder charts can be manipulated in such a manner that a target FER is obtained. Assuming a singular channel realisation, the equaliser chart's position is determined by the TX power and modulation, while the decoder chart's position depends only on the applied code rate and is independent of the channel realisation.

Similarly to Sects. 4.3.1 and 4.3.2, this chapter develops LA schemes for vertically and horizontally encoded systems. Two schemes are presented for both scenarios: in TX power adaptation, the modulation and code rate are fixed, while the AMC schemes assume fixed TX power. Combining AMC with TX power adaptation is perfectly feasible, but as was pointed out in [203], relatively little spectral efficiency is lost with fixed TX power or rate. For vertically encoded systems, the TX power optimisation and AMC methods are complemented by adaptive RR-HARQ and IR-HARQ schemes, respectively. Since numerical evaluations are required in the derivation of the approximate LLR variance distribution at the equaliser output, the optimisation needs to be performed iteratively. Therefore, it is impossible to determine an exact target FER. Thus, a target FER region is defined, whose upper and lower limits are denoted by $\overline{\mathrm{FER}}_{\mathrm{U}}$ and $\overline{\mathrm{FER}}_{\mathrm{L}}$, respectively.

For MIMO transmissions, due to the shapes of the transfer charts, the probability of intersection is usually at its maximum between $\tilde{I}_{\mathrm{a}}^{\mathrm{ext}} \in [0.25, 0.4]$ (see Figs. 3 and 10). In order to reduce the number of computations during the adaptation process, the FER will be approximated at a single point. An experimentally determined value, $\hat{I}_{\mathrm{opt}}^{\mathrm{apr}} = \tilde{I}_{\mathrm{opt}}^{\mathrm{ext}} = 0.35$, is used. However, the intersection probability is not always at its maximum at this point. When also taking into consideration the potential mismatch between the prediction and MC computer simulations, the proposed LA methods occasionally produce FERs that are above the target. With SISO and SIMO transmissions, the received signal does not suffer from CAI. As was illustrated in Figs. 9 and 10, the

benefit from SIC is smaller than with multiple TX antennas. Hence, the equaliser charts have a smaller slope and the probability of an intersection is at its maximum at the right edge of the chart. Thus, when adapting the transmission parameters for SISO and SIMO systems, point $\hat{I}_{\mathrm{opt}}^{\mathrm{apr}} = \tilde{I}_{\mathrm{opt}}^{\mathrm{ext}} \rightarrow 1$ will be considered. The matching SIC coefficients, $\hat{\Delta}_{\mathrm{opt}}$, are determined in the same manner as in the beginning of Sect. 4.2.1.

5.1 Vertically encoded systems

LA is a relatively simple process for vertically encoded and SISO/SIMO systems. A single equaliser chart and a single decoder chart need to be considered. The transmitter determines how many antennas shall be employed. TX power is distributed evenly across the active antennas, denoted by $N_{\mathrm{T}}^{\mathrm{act}} \leq N_{\mathrm{T}}$. The TX power control and AMC schemes are complemented by adaptive RR-HARQ and IR-HARQ strategies, respectively. The proposed adaptive HARQ schemes do not target a particular PDP.

Since the receiver does not know the original bit sequence, it cannot use (14) to calculate the level of mutual information from the LLRs. However, if the LLRs are IID for all bit positions, mutual information can be calculated from the absolute LLR values without using histograms [308]. As was pointed out in Sect. 4.1, for 8-PSK the LLR distributions are not identical for all bit positions. For such cases, the method in [308] would require the forming of histograms for statistically different bit positions.

The proposed feedback will still use absolute LLRs, but it will overcome the need of forming histograms by using modulation-wise LUTs. Although this is only an issue for 8-PSK, an LUT is also made for BPSK/QPSK. The receiver measures the average of the absolute demapped LLRs after the first instance of equalisation, $\mathrm{avg}\left(\left|\boldsymbol{\mathcal{L}}^{\mathrm{eo},w,1}\right|\right)$.[21] A more accurate reflection of the channel quality is obtained when there is no *a priori* information from the decoder. If the receiver is unable to recover the original packet, it finds $\hat{\sigma}_{\mathrm{fb}}^2$ that matches $\mathrm{avg}\left(\left|\boldsymbol{\mathcal{L}}^{\mathrm{eo},w,1}\right|\right)$ from the LUT. The value of $\hat{\sigma}_{\mathrm{fb}}^2$, when transported to the mutual information domain through the use of the J-function, approximately determines the position of the equaliser chart for that particular channel realisation. It is assumed that the feedback channel does not induce errors. Since the successive channel realisations are temporally uncorrelated, feedback delay is inconsequential. The transmitter then utilises $\hat{\sigma}_{\mathrm{fb}}^2$ to optimise the power of the retransmitted packet and the

[21] In [282], a similar reliability metric was averaged from the absolute values of information-bit-wise *a posteriori* LLRs of a MAP decoder that operated on convolutionally encoded codewords. Based on the metric, a "virtual" code rate and upper and lower bounds for FER were obtained semi-analytically.

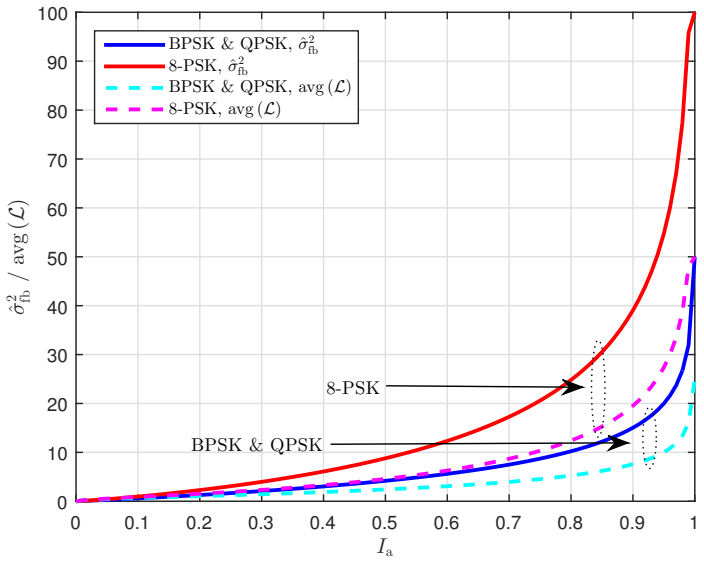

Fig. 21. The LLR variance, $\hat{\sigma}^2_{\text{fb}}$, and the average of the absolute LLRs, $\text{avg}\,(|\mathcal{L}|)$, with respect to mutual information value I_{a}.

number of additional parity bits for RR-HARQ and IR-HARQ, respectively. Fig. 21 presents the $\hat{\sigma}^2_{\text{fb}}$ and avg $(|\mathcal{L}|)$ pairings for a given I_{a}.

The proposed adaptive HARQ techniques assume that all the HARQ packets related to the original packet are equalised at each global iteration, as described in [117]. For the RR-HARQ case, the summation was given in (12). The reasoning behind this strategy is due to the fact that the initial transmission is always the most important one. First, consider the RR-HARQ scenario. Assuming that $\overline{\text{FER}}_{\text{U}} < 1/2$ and that the transmitter can afford to scale back its TX power from the maximum, the initial version of the packet has the best effective SINR at the equaliser output. This also means that the interference level is higher for the initial transmission than for the retransmissions, where TX power is further reduced and noise dominates the effective SINR. Thus, the initial version of the packet gains more from SIC than the retransmissions.

With the IR-HARQ scheme, the initial packet already contains all the information bits. Subsequent IR transmissions are reserved for additional parity bits that were initially punctured. By equalising the initial packet during each global iteration of subsequent IR transmissions, the quality of the information bits entering the decoder is enhanced. If only the latest packet was equalised, only the quality of a small fraction of the parity bit LLRs would be enhanced.

5.1.1 Power adaptation and RR-HARQ for vertically encoded systems

In the proposed TX power adaptation scheme, the modulation and code rate are fixed. Therefore, the position of the decoder's EXIT chart is stationary. The matching decoder LLR variance is determined from the decoder EXIT charts, i.e. $\tilde{\sigma}^2_{\text{opt}} + \tilde{\epsilon}_{\text{opt}} = \left[J^{-1}\left(\tilde{g}^{-1}\left(\tilde{I}^{\text{ext}}_{\text{opt}} = 0.35\right) + \epsilon\right)\right]^2$. Since the exact channel realisation is not known in advance, the goal is to manipulate the equaliser chart's distribution through TX power adaptation such that $\overline{\text{FER}}_{\text{L}} < \widetilde{\text{FER}} < \overline{\text{FER}}_{\text{U}}$. The transmitter can adjust the number of active TX antennas, $N_{\text{T}}^{\text{act}}$, and the level of applied TX power, P_{opt}. The maximum TX power $P_{\max} = \sum_{j=1}^{N_{\text{T}}^{\text{act}}} P_{\max,j} = 1$. For vertically encoded systems, $P_{\max,j} = 1/N_{\text{T}}^{\text{act}}$, $j = 1, \ldots, N_{\text{T}}^{\text{act}}$.

Procedure A1: TX power control for vertically encoded systems

A1-1 **Determining the number of active TX antennas:** The transmitter executes the FER prediction procedure described in Sects. 4.2 and 4.3 assuming the appropriate modulation order and code rate while going through $N_{\text{T}}^{\text{act}} = 1, \ldots, N_{\text{T}}$, active TX antennas to see whether it can reach the target FER. The antenna-wise TX power allocation is $P_j = 1/N_{\text{T}}^{\text{act}}$, $j = 1, \ldots, N_{\text{T}}^{\text{act}}$. If the transmitter cannot reach the target FER with $N_{\text{T}}^{\text{act}} = 1$, it skips the rest of Procedure A1 and transmits with $N_{\text{T}}^{\text{act}} = 1$ and $P_1 = P_{\max}$. If the target FER is reached, the transmitter picks the largest $N_{\text{T}}^{\text{act}}$ with which it managed to attain the target and executes the remaining steps of Procedure A1.

A1-2 **Rough SNR optimisation:** By combining (27) and (28) and adding a scalable power, P_{opt},

$$\frac{\tilde{\sigma}_{\text{a}}^2}{4N_{\mathcal{M}} + \hat{\Delta}_{\text{opt}}\tilde{\sigma}_{\text{a}}^2} = \frac{\sigma_\eta^2}{4\hat{\Delta}_{\text{opt}}^2 P_{\text{opt}}} \mathcal{F}\left(\frac{N_{\text{R}}\hat{\Delta}_{\text{opt}} P_{\text{opt}}}{N_{\text{T}}^{\text{act}}\sigma_\eta^2}, \frac{N_{\text{T}}^{\text{act}}}{N_{\text{R}}}\right). \tag{38}$$

Since (27) gives the mean SINR of an uncorrelated channel, the FER for an uncorrelated channel with an SNR of $P_{\text{opt}}/\sigma_\eta^2$, where P_{opt} satisfies (38), is approximately 1/2.

A1-3 **Fine SNR optimisation:** Starting with P_{opt} obtained in Step A1-2, the FER prediction procedure from Sects. 4.2 and 4.3 is repeated and P_{opt} is iteratively adjusted until the target FER region is reached.

A1-4 **Power adaptation:** The transmitter adjusts the antenna-wise power,

$$P_j = \frac{\min\left(P_{\max}, P_{\text{opt}}\right)}{N_{\text{T}}^{\text{act}}}, \quad j = 1, \ldots, N_{\text{T}}^{\text{act}}. \tag{39}$$

For fading channels with Gaussian noise, without channel-coefficient-wise CSIT and perfect CSIR, constant power allocation is capacity-wise the optimal strategy [309]. Since the assumed CSIT is time- and space-invariant, all new packets shall be transmitted with constant power. If the wth version of the packet is received unsuccessfully, the following adaptive RR-HARQ scheme is initiated.

Procedure A2: TX power control for RR-HARQ retransmissions

A2-1 **Feedback from the receiver:** Feedback from the wth transmission, $\hat{\sigma}^2_{\text{fb},w}$, derived from $\left(N_{\text{T}}^{\text{act}} K \log_2(M)\right)^{-1} \sum_{n=1}^{N_{\text{T}}^{\text{act}} K \log_2(M)} \left|\mathcal{L}_n^{\text{eo},w,1} + \sum_{u=1}^{w-1} \mathcal{L}_n^{\text{eo},u,N_d(w-u)+1}\right|$ through the use of the LUT (see Fig. 21), is sent to the transmitter. Note that the feedback computation discards the positions of the punctured parity bits, unlike (12). When $w = 1$, the sum term does not exist.

A2-2 **Determining the power of the retransmitted packets:** The asymptotic effective SINR formula (27) is applied again,

$$\frac{\tilde{\sigma}^2_{\text{opt}} + \tilde{\epsilon}_{\text{opt}} - \hat{\sigma}^2_{\text{fb},w}}{4N_{\mathcal{M}} + \hat{\Delta}_{\text{opt}}\left(\tilde{\sigma}^2_{\text{opt}} + \tilde{\epsilon}_{\text{opt}} - \hat{\sigma}^2_{\text{fb},w}\right)} = \frac{\sigma_\eta^2}{4\hat{\Delta}^2_{\text{opt}} P_{\text{RR}}^{(w+1)}} \mathcal{F}\left(\frac{N_{\text{R}} \hat{\Delta}_{\text{opt}} P_{\text{RR}}^{(w+1)}}{N_{\text{T}}^{\text{act}} \sigma_\eta^2}, \frac{N_{\text{T}}^{\text{act}}}{N_{\text{R}}}\right). \tag{40}$$

The TX power allocated to the $(w+1)$th transmission, i.e. the wth retransmission, is found by solving (40). It is possible that $\hat{\sigma}^2_{\text{fb},w} > \tilde{\sigma}^2_{\text{opt}} + \tilde{\epsilon}_{\text{opt}}$, which leads to $P_{\text{RR}}^{(w+1)} < 0$. Since the decoder deals with finite-length code words, it cannot always exploit the gap, even with $\epsilon > 0$. Therefore, the antenna-wise TX power of the $(w+1)$th transmission of the packet,

$$P_{\text{RR},j}^{(w+1)} = \frac{\max\left(Q_{P_{\text{opt}}}^{\min} P_{\text{opt}}, P_{\text{RR}}^{(w+1)}\right)}{N_{\text{T}}^{\text{act}}}, \quad j = 1, \ldots, N_{\text{T}}^{\text{act}}, \tag{41}$$

where $Q_{P_{\text{opt}}}^{\min} \in (0, 1]$ denotes the minimum ratio of P_{opt} that is to be allocated for the retransmitted packets.

The soft symbols, $\tilde{\boldsymbol{x}}$, which are produced when the (re)punctured and (re)interleaved decoder output LLRs are soft mapped, reduce the interference from each version of the

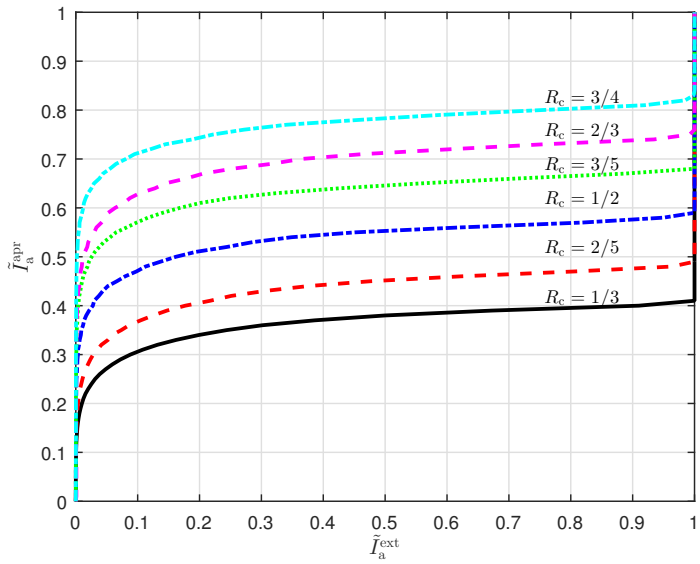

Fig. 22. MC simulated 3GPP turbo decoder EXIT charts for various code rates. The puncturing was performed by the 3GPP rate matching algorithm. 6 decoding iterations were assumed.

transmitted packet in equalisation. With the proposed RR-HARQ TX power adaptation scheme, the FER of each retransmission is expected to be approximately half of the FER of the preceding transmission, assuming that there is no spatial correlation.

5.1.2 Adaptive modulation and coding and IR-HARQ for vertically encoded systems

The AMC scheme adjusts the decoder chart's position in order to reach the target FER. The transmitter has an LUT of decoder EXIT charts for different code rates, see Fig. 22. Two modulation-dependent equaliser output LLR variance distributions are considered.

Procedure B1: AMC for vertically encoded systems

B1-1 **Determining the number of active TX antennas:** The transmitter executes the FER prediction procedure described in Sects. 4.2 and 4.3 assuming the lowest available modulation order and minimum code rate, $R_c^{\min}$, while going through $N_T^{act} = 1, \ldots, N_T$, active TX antennas to see whether it can reach the target FER. The antenna-wise TX power allocation is $P_j = 1/N_T^{act}$, $j = 1, \ldots, N_T^{act}$. If

the transmitter cannot reach the target FER with $N_{\mathrm{T}}^{\mathrm{act}} = 1$, it skips the rest of Procedure B1 and transmits using the lowest available modulation order and code rate. If the target FER is reached, the transmitter picks the largest $N_{\mathrm{T}}^{\mathrm{act}}$ with which it attained the target and executes the remaining steps of Procedure B1.

B1-2 **Adaptation of the modulation-wise decoder EXIT chart positions:** The LLR variance distributions are obtained by utilising the SINR distribution developed in Step B1-1 for $N_{\mathrm{T}}^{\mathrm{act}}$ and (28). Since $N_{\mathcal{M}} = 2$ for BPSK and $N_{\mathcal{M}} = 1$ for QPSK and 8-PSK, two different LLR distributions need to be derived, as can be witnessed from (29). After a slight simplification of (31),

$$\widetilde{\mathrm{FER}} = \frac{\gamma\left(m, \frac{m}{\Omega}\left(\tilde{\sigma}^2_{\mathrm{opt}} + \tilde{\epsilon}_{\mathrm{opt}}\right)^2\right)}{\Gamma(m)}. \tag{42}$$

The transmitter iteratively adjusts $\tilde{\sigma}^2_{\mathrm{opt}} + \tilde{\epsilon}_{\mathrm{opt}}$ for both possible LLR variance distributions until the target FER region is reached.

B1-3 **Determining the modulation-wise code rates:** Using the modulation-wise approximate J-function from (15a), unique decoder EXIT chart positions are obtained for each modulation, i.e. $\tilde{I}^{\mathrm{ext}}_{\mathrm{opt}} + \epsilon = J\left(\sqrt{\tilde{\sigma}^2_{\mathrm{opt}} + \tilde{\epsilon}_{\mathrm{opt}}}\right)$. The obtained modulation-wise mutual information values, $\tilde{I}^{\mathrm{ext}}_{\mathrm{opt}}$, are compared to the code-rate-wise values that are stored in the LUT. The optimal code rates are obtained by interpolation between the different code-rate-wise points in the LUT. Thus, the process of going from the LLR variance to the code rate can be viewed as $R_{\mathrm{c}}^{\mathrm{opt}} = g_{R_{\mathrm{c}}}\left(\tilde{\sigma}^2_{\mathrm{opt}}\right)$, where $g_{R_{\mathrm{c}}}(\cdot)$ maps an LLR variance input to a code rate.

B1-4 **Selection of the optimal MCS:** It is possible that $\tilde{I}^{\mathrm{ext}}_{\mathrm{opt}}$ falls below the EXIT chart point of the minimum code rate for some of the modulations. Such modulations are discarded. If there is more than one MCS that is able to provide an FER that falls within the target region, the highest possible modulation is chosen, thereby defining the optimal modulation order, M^{opt}. This is due to the observation that the decoder EXIT charts of highly punctured code rates lose some of their accuracy. This can be related back to the findings in [102], where it was noticed that the performance of a turbo decoder suffered as a consequence of puncturing when $R_{\mathrm{c}} > 2/3$. The convolutional component codes become very weak.

B1-5 **Obtaining the proper code rate:** The puncturing pattern is determined by the 3GPP rate matching scheme [64].

The AMC method for vertically encoded and SISO/SIMO systems is complemented by a rate adaptation IR-HARQ scheme, which maintains M^{opt} from Step B1-4.

Procedure B2: Code rate adaptation for IR-HARQ transmissions

B2-1 **Feedback from the receiver:** The adaptive IR-HARQ scheme uses the same feedback method as the adaptive RR-HARQ scheme in Step A2-1.

B2-2 **Code rate adaptation for the first retransmission:** Similarly to Step A2-2, it is possible that $R_c^{fb} = g_{R_c}\left(\hat{\sigma}_{fb}^2\right) > R_c^{opt}$. It is also possible that R_c^{fb} is only slightly smaller than R_c^{opt}. In such a case, the transmitter may try to send only a handful of additional parity bits. When the length of the original sequence is thousands of bits, the addition of a couple of dozen sparsely scattered parity bits does not significantly aid the decoder. Thus, once the additional parity bits of the first IR transmission ,or the second transmission related to the original packet, have arrived, the code rate at the receiver,

$$R_c^{IR,2} = \max\left(\min\left(R_c^{fb}, R_c^{opt} - Q_{R_c^{opt}}^{min}\right), R_c^{min}\right), \tag{43}$$

where $Q_{R_c^{opt}}^{min}$ denotes a predetermined minimum decrease from the original optimised code rate R_c^{opt}. If $\min\left(R_c^{fb}, R_c^{opt} - Q_{R_c^{opt}}^{min}\right) < R_c^{min}$, all the remaining punctured parity bits are transmitted, i.e. $R_c^{IR,2} = R_c^{min}$.

B2-3 **Selection of additional parity bits:** The 3GPP rate matching algorithm picks the requisite number of IR parity bits from the set of remaining punctured bits.

If the first IR transmission does not produce a correctly decoded frame, the same number of additional parity bits are sent during a second IR transmission, if possible.[22] If the first two IR transmissions are unsuccessful, the remaining parity bits are transmitted during a third IR transmission, assuming that such bits remain to be sent, i.e. $R_c^{IR,4} = R_c^{min}$. At the receiver, the initial packet and the IR packets are equalised separately, after which the received bits are interspersed to their proper positions before decoding.

5.2 Horizontally encoded systems

In the case of horizontally encoded systems, multiple equaliser and decoder charts need to be considered. Furthermore, the interference from the parallel streams influences the positions of the equaliser charts. Nevertheless, LA can be extended for such systems by using the FER prediction method described in Sect. 4.3.2 and Appendix 6. Sects. 5.2.1

[22] If $1/R_c^{IR,2} - 1/R_c^{opt} > 1/R_c^{min} - 1/R_c^{IR,2}$, there will not be the same number of parity bits to be sent. In such a case, all the remaining punctured parity bits are transmitted, i.e. $R_c^{IR,3} = R_c^{min}$ at the receiver.

and 5.2.2 propose iterative TX power adaptation and AMC schemes for horizontally encoded systems with $N_{\mathrm{T}} = 3$. The proposed LA methods can be expanded for $N_{\mathrm{T}} > 3$. As before in Sect 5.1, the transmitter can freely determine the number of active TX antennas, $N_{\mathrm{T}}^{\mathrm{act}}$. However, there are two notable differences compared to the vertical LA schemes: Firstly, the transmitter cannot reallocate TX power between antennas. Secondly, there are no complementing adaptive HARQ schemes.

At various steps of the following procedures, alternative options are available. In such situations, "⇒" indicates an exit from the procedure, while "⇓" indicates that the procedure is carried on to the next step.

5.2.1 Power adaptation for horizontally encoded systems

It would be very time-consuming to accurately adjust the TX powers of parallel spatial streams individually, since a change in the TX power of a single stream has an impact on the SINRs of the parallel streams. Therefore, the proposed TX power adaptation procedure fixes the power ratios of the parallel streams by considering the stream-wise modulation orders and code rates, M_j and $R_{\mathrm{c},j}$, respectively, with $j = 1, \ldots, N_{\mathrm{T}}$. Thus, the stream-wise TX powers are adjusted jointly. It is assumed that the transmitter can allocate the same amount of power for each antenna, i.e. $P_{\max,j} = 1/N_{\mathrm{T}}$, $j = 1, \ldots, N_{\mathrm{T}}$, regardless of $N_{\mathrm{T}}^{\mathrm{act}}$. Thus, $P_{\max} = \sum_{j=1}^{N_{\mathrm{T}}} P_{\max,j} = 1$. Let $P_{\mathrm{opt},j}^{\left(N_{\mathrm{T}}^{\mathrm{act}}\right)}$ denote the optimised TX power of the jth stream, when $N_{\mathrm{T}}^{\mathrm{act}}$ antennas are used for transmission.

Procedure C: TX power control for horizontally encoded systems

C-1 **TX power adaptation for SIMO channels:** Procedure A1 is applied to evaluate the optimal TX powers for each MCS in a SIMO scenario. The transmitter sorts the streams in an ascending order based on the optimised TX powers, i.e. $P_{\mathrm{opt},1}^{(1)} < \cdots < P_{\mathrm{opt},N_{\mathrm{T}}}^{(1)}$.

C-2 **TX power adaptation for two antennas:** If $P_{\mathrm{opt},1}^{(1)} < P_{\max,1}$ and the stream-wise channel codes are of equal strength[23], the transmitter determines the preliminary powers for the two considered streams,

$$P_{\mathrm{opt},j}^{(2)} = \frac{\log_2\left(M_j\right) R_{\mathrm{c},j}}{\log_2\left(M_1\right) R_{\mathrm{c},1}} P_{\mathrm{opt},1}^{(1)}, \quad j = 1, 2. \tag{44}$$

[23] If the stream-wise coding gains differ significantly, (44) and (45) would need to reflect that, e.g. by defining the TX power ratios for $P_{\mathrm{opt},j}^{\left(N_{\mathrm{T}}^{\mathrm{act}}\right)}$ from the ratios of $P_{\mathrm{opt},1}^{(1)}, \ldots, P_{\mathrm{opt},N_{\mathrm{T}}}^{(1)}$, i.e. $P_{\mathrm{opt},j}^{\left(N_{\mathrm{T}}^{\mathrm{act}}\right)} / P_{\mathrm{opt},1}^{\left(N_{\mathrm{T}}^{\mathrm{act}}\right)} = P_{\mathrm{opt},j}^{(1)} / P_{\mathrm{opt},1}^{(1)}$, $j \geq 2$.

The transmitter applies (37) to approximate the FERs of streams 1 and 2. $P^{(2)}_{\text{opt},j}$ are adjusted iteratively until $\overline{\text{FER}}_\text{L} < \max\left(\widetilde{\text{FER}}_1, \widetilde{\text{FER}}_2\right) < \overline{\text{FER}}_\text{U}$. The ratio $P^{(2)}_{\text{opt},2}/P^{(2)}_{\text{opt},1}$ remains fixed throughout the iterations.

⇒ If $P^{(2)}_{\text{opt},2} > P_{\text{max},2}$, only stream 1 transmits data with power $P^{(1)}_{\text{opt},1}$.

⇓ Otherwise, proceed to Step C-3.

C-3 **TX power adaptation for three antennas:** If $P^{(2)}_{\text{opt},2} < P_{\text{max},2}$, the preliminary stream-wise powers,

$$P^{(3)}_{\text{opt},j} = \frac{\log_2\left(M_j\right) R_{\text{c},j}}{\log_2\left(M_1\right) R_{\text{c},1}} P^{(1)}_{\text{opt},1}, \quad j = 1,2,3. \tag{45}$$

The transmitter applies (87) to approximate the FER for three TX antennas. $P^{(3)}_{\text{opt},j}$ are iteratively adjusted until $\overline{\text{FER}}_\text{L} < \max_{j=1,2,3}\left(\widetilde{\text{FER}}_j\right) < \overline{\text{FER}}_\text{U}$. Again, the ratios of $P^{(3)}_{\text{opt},j}$ remain fixed $\forall\, j$.

⇒ If $P^{(3)}_{\text{opt},3} > P_{\text{max},3}$, only streams 1 and 2 are employed, with allocated powers $P^{(2)}_{\text{opt},j}$, $j = 1,2$.

⇒ Otherwise, all three antennas are used to transmit data with allocated powers $P^{(3)}_{\text{opt},j}$, $j = 1,2,3$.

The process can be extended for $N_\text{T} > 3$ by carrying on from Step C-3 in a similar fashion. The described iterative power adaptation process is significantly more complex than the vertically encoded case in Procedure A1. Therefore, it is advisable to determine a wider target FER range, e.g. by reducing $\overline{\text{FER}}_\text{L}$.

5.2.2 Adaptive modulation and coding for horizontally encoded systems

Before proceeding to the actual horizontal AMC scheme, the stream-wise TX powers are arranged in a descending order, i.e. $P_1 > \cdots > P_{N_\text{T}}$ and $P_\text{tot} = 1$. Another limiting FER value, namely $\overline{\text{FER}}_\text{H}$, is defined for this AMC scheme: when $\widetilde{\text{FER}}_{j-1} < \overline{\text{FER}}_\text{U}$, the jth stream is used for transmission only if $\widetilde{\text{FER}}_j < \overline{\text{FER}}_\text{H}$, with $\overline{\text{FER}}_\text{H} \geq \overline{\text{FER}}_\text{U}$, $j \geq 2$.

Procedure D: AMC for horizontally encoded systems

D-1 **FER prediction for the strongest stream in a SIMO channel:** The transmitter applies the FER prediction method from Sect. 4.3.1 to evaluate whether the strongest stream, with P_1, can reach the target FER with the lowest available modulation order (here BPSK) and $R^{\text{opt}}_{\text{c},1} = R^{\min}_\text{c}$.

$\Rightarrow$ If $\widetilde{\mathrm{FER}}_1 > \overline{\mathrm{FER}}_\mathrm{U}$, only the strongest stream is used for transmission with BPSK and $R_{\mathrm{c},1}^{\mathrm{opt}} = R_\mathrm{c}^{\min}$.

$\Downarrow$ Otherwise, proceed to Step D-2.

D-2 **FER prediction for the two strongest streams:** The transmitter allocates BPSK and $R_{\mathrm{c},2}^{\mathrm{opt}} = R_\mathrm{c}^{\min}$ to the second strongest stream. By modifying (37),

$$\widetilde{\mathrm{FER}}_2 = \left[1 - \overline{\mathrm{FER}}_\mathrm{U}\right] \mathcal{P}_2^\epsilon \left(\hat{I}_{\mathrm{opt},2}^{\mathrm{apr}} \,\middle|\, \hat{I}_{\mathrm{a},1}^{\mathrm{apr}} \to 1\right) + \overline{\mathrm{FER}}_\mathrm{U} \mathcal{P}_2^\epsilon \left(\hat{I}_{\mathrm{opt},2}^{\mathrm{apr}} \,\middle|\, \hat{I}_{\mathrm{a},1}^{\mathrm{apr}} = 0\right). \tag{46}$$

$\Rightarrow$ If $\widetilde{\mathrm{FER}}_2 > \overline{\mathrm{FER}}_\mathrm{H}$, M_1^{opt} and $R_{\mathrm{c},1}^{\mathrm{opt}}$ are obtained by performing Procedure B1 for a single TX antenna.

$\Rightarrow$ If $\overline{\mathrm{FER}}_\mathrm{U} < \widetilde{\mathrm{FER}}_2 < \overline{\mathrm{FER}}_\mathrm{H}$, M_1^{opt} and $R_{\mathrm{c},1}^{\mathrm{opt}}$ are adjusted such that

$$\widetilde{\mathrm{FER}}_1 = \left[1 - \widetilde{\mathrm{FER}}_2\right] \mathcal{P}_1^\epsilon \left(\hat{I}_{\mathrm{opt},1}^{\mathrm{apr}} \,\middle|\, \hat{I}_{\mathrm{a},2}^{\mathrm{apr}} \to 1\right) + \widetilde{\mathrm{FER}}_2 \mathcal{P}_1^\epsilon \left(\hat{I}_{\mathrm{opt},1}^{\mathrm{apr}} \,\middle|\, \hat{I}_{\mathrm{a},2}^{\mathrm{apr}} = 0\right), \tag{47}$$

satisfies $\overline{\mathrm{FER}}_\mathrm{L} < \widetilde{\mathrm{FER}}_1 < \overline{\mathrm{FER}}_\mathrm{U}$. Since P_j, $j = 1, 2$, remain constant, Procedure B1 can be applied on a stream-wise basis. Stream 2 is modulated with BPSK and $R_{\mathrm{c},2} = R_\mathrm{c}^{\min}$.

$\Downarrow$ Otherwise, proceed to Step D-3.

D-3 **FER prediction for the three strongest streams:** The transmitter allocates BPSK and $R_\mathrm{c}^{\min}$ to the third strongest stream. By utilising (87), its approximate FER

$$\begin{aligned}
\widetilde{\mathrm{FER}}_3 = &\left[1 - \overline{\mathrm{FER}}_\mathrm{U}\right] \cdot \\
&\left[\left[1 - \overline{\mathrm{FER}}_\mathrm{U}\right] \mathcal{P}_3^\epsilon \left(\hat{I}_{\mathrm{opt},3}^{\mathrm{apr}} \,\middle|\, \hat{I}_{\mathrm{opt},1}^{\mathrm{apr}} \to 1, \hat{I}_{\mathrm{opt},2}^{\mathrm{apr}} \to 1\right) + \right. \\
&\left. \overline{\mathrm{FER}}_\mathrm{U} \mathcal{P}_3^\epsilon \left(\hat{I}_{\mathrm{opt},3}^{\mathrm{apr}} \,\middle|\, \hat{I}_{\mathrm{opt},1}^{\mathrm{apr}} \to 1, \hat{I}_{\mathrm{opt},2}^{\mathrm{apr}} = 0\right)\right] + \\
&\overline{\mathrm{FER}}_\mathrm{U} \left[\left[1 - \overline{\mathrm{FER}}_\mathrm{U}\right] \cdot \right. \\
&\left[\left[1 - \overline{\mathrm{FER}}_\mathrm{U}\right] \mathcal{P}_3^\epsilon \left(\hat{I}_{\mathrm{opt},3}^{\mathrm{apr}} \,\middle|\, \hat{I}_{\mathrm{opt},1}^{\mathrm{apr}} \to 1, \hat{I}_{\mathrm{opt},2}^{\mathrm{apr}} \to 1\right) + \right. \\
&\left. \overline{\mathrm{FER}}_\mathrm{U} \mathcal{P}_3^\epsilon \left(\hat{I}_{\mathrm{opt},3}^{\mathrm{apr}} \,\middle|\, \hat{I}_{\mathrm{opt},1}^{\mathrm{apr}} = 0, \hat{I}_{\mathrm{opt},2}^{\mathrm{apr}} \to 1\right)\right] + \\
&\left. \overline{\mathrm{FER}}_\mathrm{U} \mathcal{P}_3^\epsilon \left(\hat{I}_{\mathrm{opt},3}^{\mathrm{apr}} \,\middle|\, \hat{I}_{\mathrm{opt},1}^{\mathrm{apr}} = 0, \hat{I}_{\mathrm{opt},2}^{\mathrm{apr}} = 0\right)\right].
\end{aligned} \tag{48}$$

$\Rightarrow$ If $\widetilde{\mathrm{FER}}_3 > \overline{\mathrm{FER}}_\mathrm{H}$, stream 3 does not transmit, while M_j^{opt} and $R_{\mathrm{c},j}^{\mathrm{opt}}$, $j = 1, 2$, are adjusted on a stream-wise basis such that

$$\widetilde{\mathrm{FER}}_j = \left[1 - \overline{\mathrm{FER}}_\mathrm{U}\right] \mathcal{P}_j^\epsilon \left(\hat{I}_{\mathrm{opt},j}^{\mathrm{apr}} \,\middle|\, \hat{I}_{\mathrm{a},j'}^{\mathrm{apr}} \to 1\right) + \overline{\mathrm{FER}}_\mathrm{U} \mathcal{P}_j^\epsilon \left(\hat{I}_{\mathrm{opt},j}^{\mathrm{apr}} \,\middle|\, \hat{I}_{\mathrm{a},j'}^{\mathrm{apr}} = 0\right), \tag{49}$$

satisfies $\overline{\mathrm{FER}}_\mathrm{L} < \widetilde{\mathrm{FER}}_j < \overline{\mathrm{FER}}_\mathrm{U}$, with $j' = 1, 2$, $j' \neq j$. Procedure B1 is used to determine M_j^{opt} and $R_{\mathrm{c},j}^{\mathrm{opt}}$.

⇒ If $\overline{\mathrm{FER}}_{\mathrm{U}} < \widetilde{\mathrm{FER}}_3 < \overline{\mathrm{FER}}_{\mathrm{H}}$, M_j^{opt} and $R_{\mathrm{c},j}^{\mathrm{opt}}$, $j = 1, 2$, are optimised, while the third stream employs BPSK and $R_{\mathrm{c},3}^{\mathrm{opt}} = R_{\mathrm{c}}^{\mathrm{min}}$. Thus, for $j = 1, 2$, the stream-wise approximated FERs,

$$\begin{aligned}\widetilde{\mathrm{FER}}_j = &\Big[1 - \overline{\mathrm{FER}}_{\mathrm{U}}\Big] \cdot \\ &\Big[\Big[1 - \widetilde{\mathrm{FER}}_3\Big] \mathcal{P}_j^{\epsilon}\left(\hat{I}_{\mathrm{opt},j}^{\mathrm{apr}} \,\middle|\, \hat{I}_{\mathrm{opt},j'}^{\mathrm{apr}} \to 1, \hat{I}_{\mathrm{opt},3}^{\mathrm{apr}} \to 1\right) + \\ &\widetilde{\mathrm{FER}}_3 \mathcal{P}_j^{\epsilon}\left(\hat{I}_{\mathrm{opt},j}^{\mathrm{apr}} \,\middle|\, \hat{I}_{\mathrm{opt},j'}^{\mathrm{apr}} \to 1, \hat{I}_{\mathrm{opt},3}^{\mathrm{apr}} = 0\right)\Big] + \\ &\overline{\mathrm{FER}}_{\mathrm{U}} \Big[\Big[1 - \widetilde{\mathrm{FER}}_3\Big] \cdot \\ &\Big[\Big[1 - \overline{\mathrm{FER}}_{\mathrm{U}}\Big] \mathcal{P}_j^{\epsilon}\left(\hat{I}_{\mathrm{opt},j}^{\mathrm{apr}} \,\middle|\, \hat{I}_{\mathrm{opt},j'}^{\mathrm{apr}} \to 1, \hat{I}_{\mathrm{opt},3}^{\mathrm{apr}} \to 1\right) + \\ &\overline{\mathrm{FER}}_{\mathrm{U}} \mathcal{P}_j^{\epsilon}\left(\hat{I}_{\mathrm{opt},j}^{\mathrm{apr}} \,\middle|\, \hat{I}_{\mathrm{opt},j'}^{\mathrm{apr}} = 0, \hat{I}_{\mathrm{opt},3}^{\mathrm{apr}} \to 1\right)\Big] + \\ &\widetilde{\mathrm{FER}}_3 \mathcal{P}_j^{\epsilon}\left(\hat{I}_{\mathrm{opt},j}^{\mathrm{apr}} \,\middle|\, \hat{I}_{\mathrm{opt},j'}^{\mathrm{apr}} = 0, \hat{I}_{\mathrm{opt},3}^{\mathrm{apr}} = 0\right)\Big],\end{aligned} \tag{50}$$

where $j' = 1, 2$ and $j' \neq j$. The stream-wise M_j^{opt} and $R_{\mathrm{c},j}^{\mathrm{opt}}$ are obtained by performing Procedure B1 such that $\overline{\mathrm{FER}}_{\mathrm{L}} < \widetilde{\mathrm{FER}}_j < \overline{\mathrm{FER}}_{\mathrm{U}}$, $j = 1, 2$, is satisfied.

⇒ If $\widetilde{\mathrm{FER}}_3 < \overline{\mathrm{FER}}_{\mathrm{U}}$, AMC can be performed on all three streams. Procedure B1 finds M_j^{opt} and $R_{\mathrm{c},j}^{\mathrm{opt}}$ for each stream $j = 1, 2, 3$, such that (48) is satisfied. Only the indexing needs to be changed for $j = 1, 2$.

As before with Procedure C, the horizontal AMC scheme can be extended from Step D-3 in a straightforward manner to allow $N_{\mathrm{T}} > 3$.

5.3 Numerical results

The adaptive HARQ results in this section assume that the receiver equalises the initial packet and subsequent HARQ packets separately during each global iteration. The reasoning for this was explained in Sect. 5.1. This requires that the received signal vectors and channel coefficients are stored into a memory. The main simulation parameters are largely the same as those in Table 4, although only the Proakis-C channel model shall be considered here. Since it was assumed in Sect. 4.4 that the convergence tunnel gap value $\epsilon = 0.02$, the same default value is maintained here for consistency. In the vertically encoded scenarios, for comparative purposes, a larger value, $\epsilon = 0.03$, shall also be used. Throughout the simulations, the upper limit of the target FER region, $\overline{\mathrm{FER}}_{\mathrm{U}} = 10^{-1}$. It was discovered in [310] that with IR-HARQ and a wide range of parameters, such target FER leads to near-optimal goodput, i.e. long-term average

successful throughput. The same $\overline{\mathrm{FER}}_{\mathrm{U}}$ is retained for the horizontal LA schemes, even though they do not employ HARQ.

5.3.1 Adaptive TX power control and RR-HARQ for vertically encoded systems

The performance of the adaptive TX power control and RR-HARQ scheme for vertically encoded systems from Sect. 5.1.1 is studied in Fig. 23. An uncorrelated 3×3 channel was assumed, with QPSK, $R_{\mathrm{c}} = 1/2$ and $\epsilon = 0.02$. Along with $\overline{\mathrm{FER}}_{\mathrm{U}} = 10^{-1}$, other LA-related parameters $\overline{\mathrm{FER}}_{\mathrm{L}} = 9 \cdot 10^{-2}$ and $Q_{P_{\mathrm{opt}}}^{\mathrm{min}} = 10^{-2}$. The threshold, where the transmitter can start to reduce its power, lies between -2 dB and -1 dB. Between -1 dB and 1 dB, where a single TX antenna is employed, the FER remains between $1.2 \cdot 10^{-1}$ and $1.3 \cdot 10^{-1}$. When a second TX antenna is introduced at 2 dB, the FER remains between $1.3 \cdot 10^{-1}$ and $1.4 \cdot 10^{-1}$. At 5 dB, all three TX antennas are employed and the FER again steadily hovers between $1.2 \cdot 10^{-1}$ and $1.3 \cdot 10^{-1}$.

There is some variation in the FERs of the retransmissions. When a single TX antenna or all three of them are employed, the FERs of the three retransmissions lie around $8 \cdot 10^{-2}$, $4 \cdot 10^{-2}$ and $2 \cdot 10^{-2}$. For $N_{\mathrm{T}}^{\mathrm{act}} = 2$, the corresponding FERs are approximately $7 \cdot 10^{-2}$, $2 \cdot 10^{-2}$ and 10^{-2}. Although the FERs of the first optimised retransmission are slightly larger than half of the initial transmission, which was the prediction in Sect 5.1.1 for uncorrelated channels, subsequent retransmissions approximately halve the FERs of the previous retransmissions. This can be partially attributed to feedback that gave an optimistic approximation of the quality of the initial transmission. By choosing a larger value for $Q_{P_{\mathrm{opt}}}^{\mathrm{min}}$, the FERs of the first retransmission could be reduced.

Fig. 24 features a comparison of the $P_{\mathrm{opt}}/P_{\mathrm{max}}$ ratio for the initial transmission and the $\mathrm{avg}\left(P_{\mathrm{RR}}^{(w+1)}\right)/P_{\mathrm{max}}$ ratios for the three retransmissions, where $w = 1, 2, 3$. The most notable discontinuity points can be observed at -1 dB, 2 dB and 5 dB. At those points, the transmitter first reduces its power for the initial transmission and introduces the second and third antennas, respectively. It can also be noted that the powers of the retransmissions are already being pared down before the TX power of the initial transmission is first scaled down. Procedure B2 does not consider whether the initial transmission can attain the target FER; it merely tries to reduce power consumption during the retransmissions.

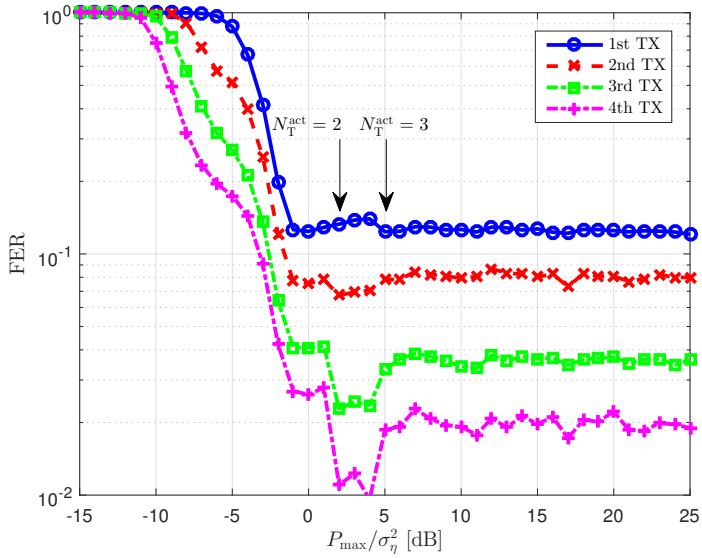

Fig. 23. The FERs of the initial transmission and three optimised RR-HARQ retransmissions, with $Q_{P_{\mathrm{opt}}}^{\min} = 10^{-2}$. An uncorrelated 3×3 Proakis-C channel with vertically encoded spatial multiplexing, QPSK, $R_{\mathrm{c}} = 1/2$ and $\epsilon = 0.02$ was assumed.

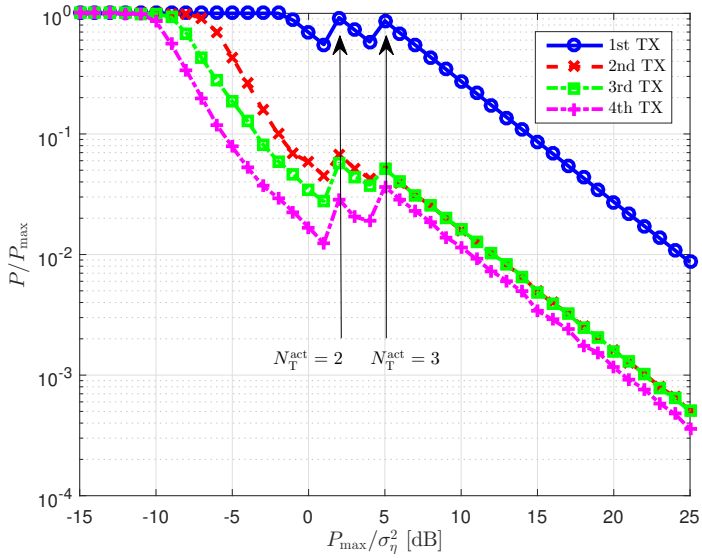

Fig. 24. $P_{\mathrm{opt}}/P_{\max}$ for the initial transmission and $\mathrm{avg}\left(P_{\mathrm{RR}}^{(w+1)}\right)/P_{\max}$, $w = 1, 2, 3$, i.e. the ratios of the average powers of the three optimised RR-HARQ retransmissions to the maximum TX power, with $Q_{P_{\mathrm{opt}}}^{\min} = 10^{-2}$. An uncorrelated 3×3 Proakis-C channel with vertically encoded spatial multiplexing, QPSK, $R_{\mathrm{c}} = 1/2$ and $\epsilon = 0.02$ was assumed.

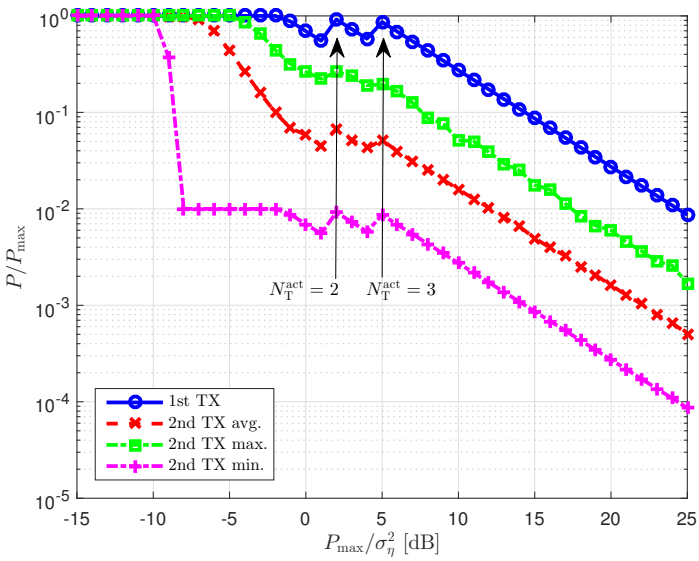

Fig. 25. $P_{\mathrm{opt}}/P_{\max}$ **for the initial transmission, and** $\mathrm{avg}\left(P_{\mathrm{RR}}^{(2)}\right)/P_{\max}$, $\max\left(P_{\mathrm{RR}}^{(2)}\right)/P_{\max}$ **and** $\min\left(P_{\mathrm{RR}}^{(2)}\right)/P_{\max}$**, i.e. the ratios of the average, maximum and minimum powers, respectively, of the first optimised RR-HARQ retransmission, to the maximum TX power. The minimum ratio is determined by** $Q_{P_{\mathrm{opt}}}^{\min} = 10^{-2}$**. An uncorrelated** 3×3 **Proakis-C channel with vertically encoded spatial multiplexing, QPSK,** $R_{\mathrm{c}} = 1/2$ **and** $\epsilon = 0.02$ **was assumed.**

The average power of the first retransmission is compared to its maximum and minimum powers in Fig. 25. After −4 dB, the maximum power ratio is roughly four times the average power ratio, while after the TX power reduction threshold point at −1 dB, the minimum power ratio is approximately one sixth of the average power ratio.

Figs. 26 and 27 illustrate how a small increase in the convergence tunnel gap requirement, from $\epsilon = 0.02$ to $\epsilon = 0.03$, impacts the FER and the $P_{\mathrm{opt}}/P_{\max}$ ratio, respectively. When $\epsilon = 0.03$, and $N_{\mathrm{T}}^{\mathrm{act}} = 1$ or $N_{\mathrm{T}}^{\mathrm{act}} = 2$, the FER of the initial transmission lies between $1.1 \cdot 10^{-1}$ and $1.2 \cdot 10^{-1}$, while for $N_{\mathrm{T}}^{\mathrm{act}} = 3$, the FER is slightly below the target of 10^{-1}. As can be seen from Fig. 27, the difference is minuscule in terms of applied TX power—the $P_{\mathrm{opt}}/P_{\max}$ graphs almost overlap.

5.3.2 AMC and adaptive IR-HARQ for vertically encoded systems

Fig. 28 examines the performance of the AMC scheme from Sect. 5.1.2 in an equicorrelated 3×5 channel with $\rho = 0.50$. $\overline{\mathrm{FER}}_{\mathrm{L}} = 9.9 \cdot 10^{-2}$, the allowed maximum code rate, $R_{\mathrm{c}}^{\max} = 9/10$ and $\epsilon = 0.02$. The adaptive IR-HARQ scheme from Procedure B2

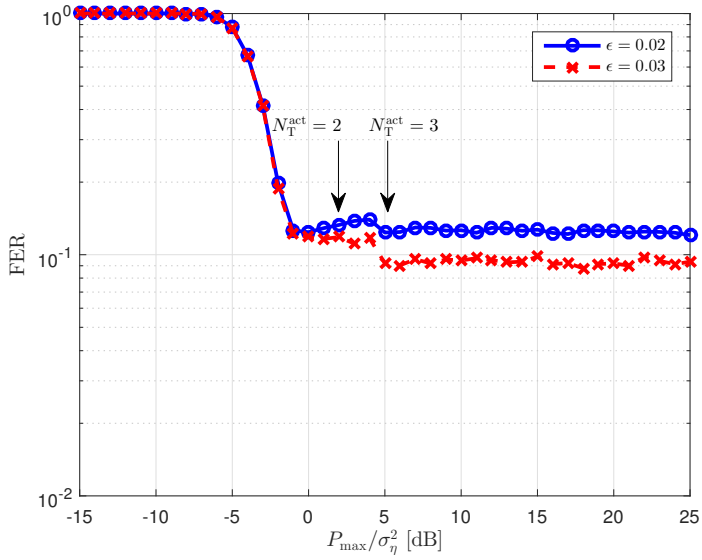

Fig. 26. The FERs of the initial transmission with convergence tunnel gap values $\epsilon = 0.02$ and $\epsilon = 0.03$. An uncorrelated 3×3 Proakis-C channel with vertically encoded spatial multiplexing, QPSK and $R_{\mathrm{c}} = 1/2$ was assumed.

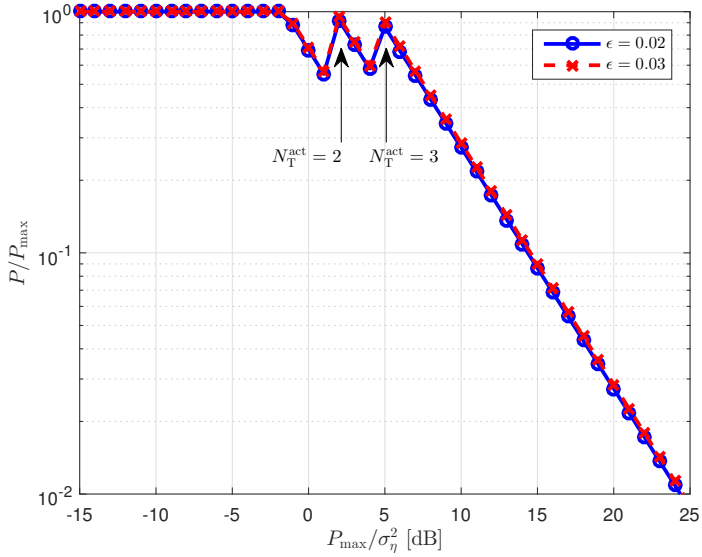

Fig. 27. $P_{\mathrm{opt}}/P_{\max}$ with convergence tunnel gap values $\epsilon = 0.02$ and $\epsilon = 0.03$. An uncorrelated 3×3 Proakis-C channel with vertically encoded spatial multiplexing, QPSK and $R_{\mathrm{c}} = 1/2$ was assumed.

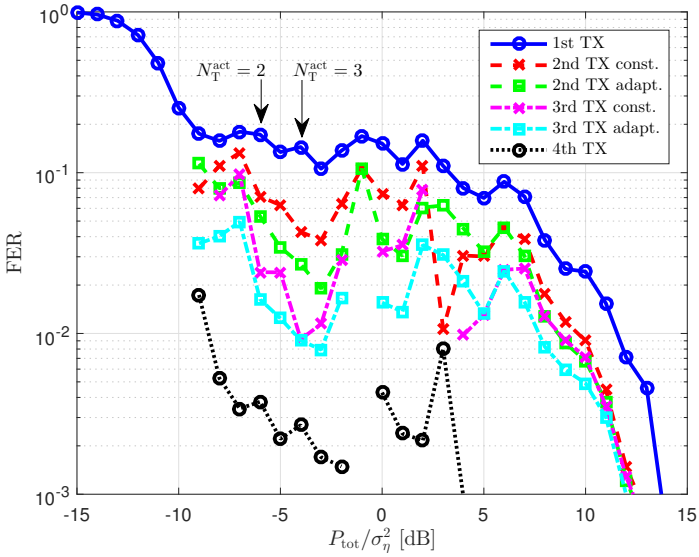

Fig. 28. The FERs of the initial and optimised IR-HARQ transmissions for an equicorrelated 3×5 Proakis-C channel with vertically encoded spatial multiplexing, $\rho = 0.50$ and $\epsilon = 0.02$. The adaptive IR-HARQ scheme from Sect. 5.1.2, with $Q_{R_{\mathrm{c}}^{\mathrm{opt}}}^{\mathrm{min}} = 10^{-2}$, is compared to a non-adaptive scheme, where the first and second IR transmission always decrease $R_{\mathrm{c}}^{\mathrm{opt}}$ by 0.02.

is compared to a non-adaptive IR-HARQ scheme, where the code rate is reduced by a constant margin during the first IR transmissions. Similarly to Procedure B2, the second IR transmission sends the same number of additional parity bits as the first one, assuming that sufficiently many punctured parity bits remain. The FER of the initial transmission is taken from the adaptive IR-HARQ simulation, but since both cases applied Procedure B1 to select the optimal modulation and initial code rate, the graphs would practically overlap. Between -9 dB and 7 dB, the FER of the initial transmission remains between $7 \cdot 10^{-2}$ and $1.8 \cdot 10^{-1}$. Since the code rate is discrete, it cannot be adjusted as smoothly as P_{opt} in the TX power adaptation scheme. Hence, the FER graph of the initial transmission does not reach a constant level like the one in Fig. 23.

Even though the packet sizes of the IR transmissions are smaller than those of the initial transmission, the same channel delay profile, Proakis-C, is assumed. This implies that the frequency bandwidth remains constant. If localised SC-FDMA was assumed for the initial transmission, this would mean that the distributed transmission mode was applied to the IR packets. If the distributed mode was already employed with the initial transmission, it would mean that the distance between employed subcarriers would be

increased for the IR transmissions. This is mainly due to the rigidity of the simulation model. If the localised SC-FDMA mode was assumed for the initial transmission as well as for the IR transmissions, different delay profiles would need to be generated for different packet sizes. However, even in the IR mode, the receiver's performance is mainly defined by the initial packet, since it contains all the information bits. Thus, the performance of the adaptive IR-HARQ scheme from Procedure B2 can be compared to the non-adaptive IR-HARQ scheme.

For the adaptive IR-HARQ scheme, the minimum code rate decrease of an IR transmission, $Q^{\min}_{R_c^{\text{opt}}} = 0.01$. The first IR transmission of the non-adaptive scheme reduces the code rate by 0.02. The same number of additional parity bits are transmitted during a second IR transmission, if required. If a third IR transmission is necessary and possible, all the remaining parity bits are transmitted. Although the adaptive scheme does not enhance the performance of the decoder, it does produce smaller FERs than the non-adaptive scheme. The adaptive scheme merely tries to optimise the number of additional parity bits in the first IR transmission. At −1 dB, $R_c^{\text{opt}} - R_c^{\min} < Q^{\min}_{R_c^{\text{opt}}}$. Thus, $R_c^{\text{IR},2} = R_c^{\min}$, which means that there are no parity bits left for further IR transmissions. A notable difference in the performances of the two schemes is witnessed at −9 dB and at 3 dB. The "constant code rate decrease" scheme transmits all the remaining parity bits in its first and only IR transmission. These are the only points in Fig. 28 where the FER of the first IR transmission of the adaptive scheme is larger than that of the non-adaptive scheme. However, the FERs of the second and third IR transmissions of the adaptive scheme are smaller than the FER of the first IR transmission of the non-adaptive scheme, which already sent its remaining parity bits. The difference is quite small in terms of FER, but it can be attributed to the time diversity that is gained by transmitting the parity bits in different time slots.

Fig. 29 illustrates how M^{opt} and R_c^{opt} of the initial transmission and $\text{avg}\left(R_c^{\text{IR},w}\right)$, $w = 2, 3$, of the first two IR transmissions are altered. Since $R_c^{\text{IR},4} = R_c^{\min} = 1/3$, it is not displayed. BPSK, QPSK and 8-PSK are distinguished by the solid, dashed and dash-dotted lines, respectively. The transmitter first adapts the code rate at −9 dB, the number of active TX antennas at −6 dB and the modulation at −1 dB. At −2 dB, the average code rate for the second IR transmission is slightly higher than for the first, which is feasible. When $R_c^{\text{IR},2} < Q^{\min}_{R_c^{\text{opt}}} R_c^{\text{opt}}$, more parity bits are transmitted and the probability that a second IR transmission is needed is reduced.

Fig. 30 displays the average, maximum and minimum code rates of the first IR transmission, i.e. $\text{avg}\left(R_c^{\text{IR},2}\right)$, $\max\left(R_c^{\text{IR},2}\right)$ and $\min\left(R_c^{\text{IR},2}\right)$, respectively. Regardless of the

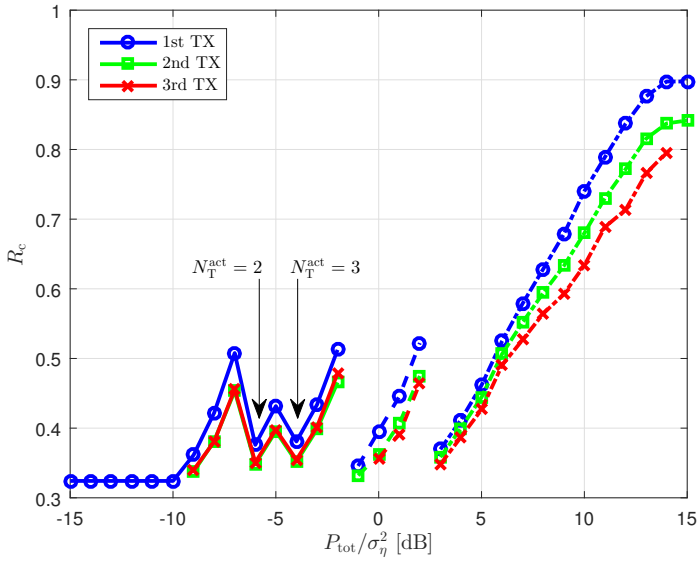

Fig. 29. The modulations, the optimised code rates for the initial transmission, $R_{\mathrm{c}}^{\mathrm{opt}}$, and averages of the optimised code rates of the first two IR-HARQ transmissions, $\mathrm{avg}\left(R_{\mathrm{c}}^{\mathrm{IR},w}\right)$, $w = 2, 3$, in an equicorrelated 3×5 Proakis-C channel with vertically encoded spatial multiplexing, $\rho = 0.50$ and $\epsilon = 0.02$. The solid, dashed and dash-dotted lines denote BPSK, QPSK and 8-PSK, respectively.

number of involved TX antennas and employed modulation, $\mathrm{avg}\left(R_{\mathrm{c}}^{\mathrm{IR},2}\right)$ remains close to $\max\left(R_{\mathrm{c}}^{\mathrm{IR},2}\right) = R_{\mathrm{c}}^{\mathrm{opt}} - Q_{R_{\mathrm{c}}^{\mathrm{opt}}}^{\mathrm{min}}$. This can be interpreted to mean that when $\overline{\mathrm{FER}}_{\mathrm{U}} = 10^{-1}$, the realised equaliser chart is rarely significantly below the decoder EXIT chart. A slight decrease of code rate is usually sufficient to push the decoder chart below the equaliser chart. Nevertheless, $\min\left(R_{\mathrm{c}}^{\mathrm{IR},2}\right)$ graph illustrates that when the channel is poor for the initial packet, a significant increase in the number of available parity bits is sometimes necessary.

Fig. 31 features a comparison of the FERs of the initial transmission with $\epsilon = 0.02$ and $\epsilon = 0.03$. When $\epsilon = 0.03$, the FER remains below $1.25 \cdot 10^{-1}$ after -5 dB. Fig. 32 illustrates how small the difference between $\epsilon = 0.02$ and $\epsilon = 0.03$ is in terms of code rate.

5.3.3 Adaptive TX power control for horizontally encoded systems

Fig. 33 depicts the FERs of three parallel streams transmitted through an equicorrelated 3×4 channel, with $\rho = 0.50$ and $\epsilon = 0.02$. The adaptive TX power control scheme from

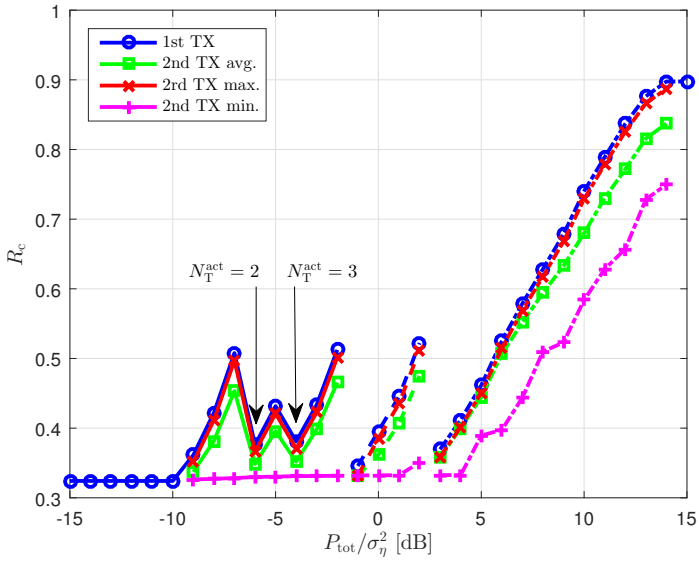

Fig. 30. The modulations, the optimised code rate for the initial transmission and the average, maximum and minimum code rates of the first IR transmission, i.e. $\mathrm{avg}\left(R_{\mathrm{c}}^{\mathrm{IR},2}\right)$, $\max\left(R_{\mathrm{c}}^{\mathrm{IR},2}\right)$ **and** $\min\left(R_{\mathrm{c}}^{\mathrm{IR},2}\right)$, **respectively, in an equicorrelated** 3×5 **Proakis-C channel with vertically encoded spatial multiplexing,** $\rho = 0.50$ **and** $\epsilon = 0.02$**. The solid, dashed and dash-dotted lines denote BPSK, QPSK and 8-PSK, respectively.**

Sect. 5.2.1 was applied, with $\overline{\mathrm{FER}}_{\mathrm{L}} = 5 \cdot 10^{-2}$. Since iterative TX power optimisation for horizontally encoded systems is computationally demanding, the gap between $\overline{\mathrm{FER}}_{\mathrm{U}}$ and $\overline{\mathrm{FER}}_{\mathrm{L}}$ is larger than with the other considered LA techniques. The stream-wise MCSs are BPSK and $R_{\mathrm{c},1} = 1/3$ for stream 1, QPSK and $R_{\mathrm{c},2} = 1/3$ for stream 2, and QPSK and $R_{\mathrm{c},3} = 1/2$ for stream 3. Since $P_{\max,j} = 1/N_{\mathrm{T}}$, $j = 1, 2, 3$, regardless of the number of active TX antennas, $N_{\mathrm{T}}^{\mathrm{act}}$, the streams are arranged in an ascending order based on their optimised TX powers for a SIMO scenario, i.e. $P_{\mathrm{opt},1}^{(1)} < P_{\mathrm{opt},2}^{(1)} < P_{\mathrm{opt},3}^{(1)}$.[24] TX power is allocated to streams 2 and 3 only when they are able to reach the target FER. Once $P_{\mathrm{opt},1}^{(1)} < P_{\max,1}$, at -3 dB, the FER of the first stream lies between $8.7 \cdot 10^{-2}$ and $1.13 \cdot 10^{-1}$, regardless of the number of interfering streams. The FERs of the second and third streams remain between $8.2 \cdot 10^{-2}$ and $9.5 \cdot 10^{-2}$, and $7.2 \cdot 10^{-2}$ and $7.5 \cdot 10^{-2}$, respectively, even though Procedure C nominally required that only $\overline{\mathrm{FER}}_{\mathrm{L}} < \max_{j=1,2,3}\left(\widetilde{\mathrm{FER}}_j\right) < \overline{\mathrm{FER}}_{\mathrm{U}}$.

[24] This is the same order as their transmission rates, i.e. $\log_2(M_1) R_{\mathrm{c},1} < \log_2(M_2) R_{\mathrm{c},2} < \log_2(M_3) R_{\mathrm{c},3}$. However, with other modulation and code rate combinations, the two orders are not automatically the same.

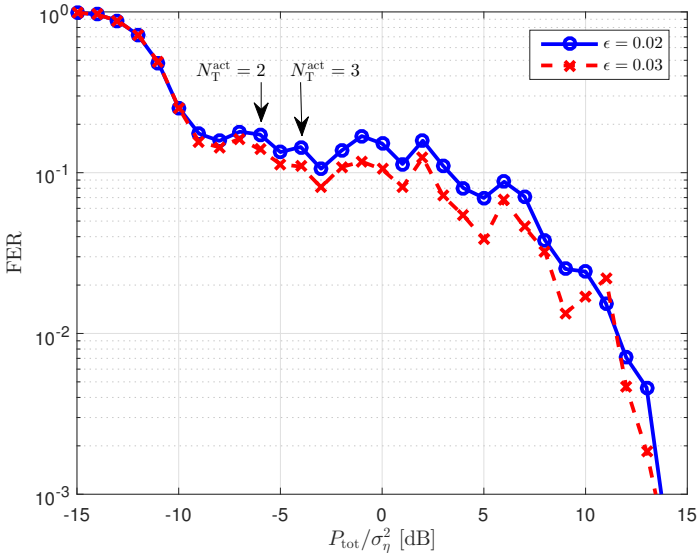

Fig. 31. The FERs of the initial transmission for an equicorrelated 3×5 Proakis-C channel with vertically encoded spatial multiplexing and $\rho = 0.50$. Two different convergence tunnel gap values, $\epsilon = 0.02$ and $\epsilon = 0.03$, were assumed.

The stream-wise $P_{\mathrm{opt},j}^{(N_{\mathrm{T}}^{\mathrm{act}})}/P_{\mathrm{max},j}$ are depicted in Fig. 34. The activation of the second stream at 1 dB has a barely noticeable impact on the optimised-to-maximum power ratio of the first stream, i.e. $P_{\mathrm{opt},1}^{(2)} \approx P_{\mathrm{opt},1}^{(1)}$. Since the first stream does very little to adjust its TX power, its FER in Fig. 33 goes above $\overline{\mathrm{FER}}_{\mathrm{U}}$ once the second stream is activated. However, after the activation of the third stream at 3 dB, the first two streams do not scale down their TX powers as much as they would do when $N_{\mathrm{T}}^{\mathrm{act}} = 2$, i.e. $P_{\mathrm{opt},j}^{(3)} > P_{\mathrm{opt},j}^{(2)}$, $j = 1, 2$.

5.3.4 AMC for horizontally encoded systems

The AMC scheme for horizontally encoded systems, described in Sect. 5.2.2, is put to the test in Fig. 35, where $\overline{\mathrm{FER}}_{\mathrm{L}} = 9.9 \cdot 10^{-2}$ and $\overline{\mathrm{FER}}_{\mathrm{H}} = 5 \cdot 10^{-1}$. An uncorrelated 3×3 channel is considered and the stream-wise powers were $P_1 = 1/2$, $P_2 = 1/3$ and $P_3 = 1/6$. The transmitter does not reallocate unused TX power to transmitting antennas. Each antenna uses all of its available TX power, P_j, or none at all. The second and third streams only transmit when their $\widetilde{\mathrm{FER}}_j < \overline{\mathrm{FER}}_{\mathrm{H}}$, $j = 2, 3$. Between $P_{\mathrm{tot}}/\sigma_\eta^2$ values -6 dB and 9 dB, and -2 dB and 9 dB, the FERs of streams 1 and 2, respectively, remain

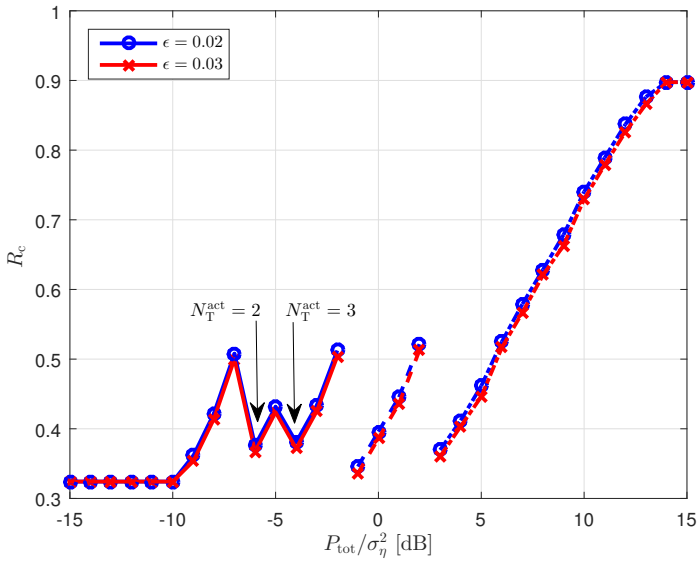

Fig. 32. The modulations and adapted initial code rates for an equicorrelated 3×5 Proakis-C channel with vertically encoded spatial multiplexing and $\rho = 0.50$. Two different convergence tunnel gap values, $\epsilon = 0.02$ and $\epsilon = 0.03$, were assumed. The solid, dashed and dash-dotted lines denote BPSK, QPSK and 8-PSK, respectively.

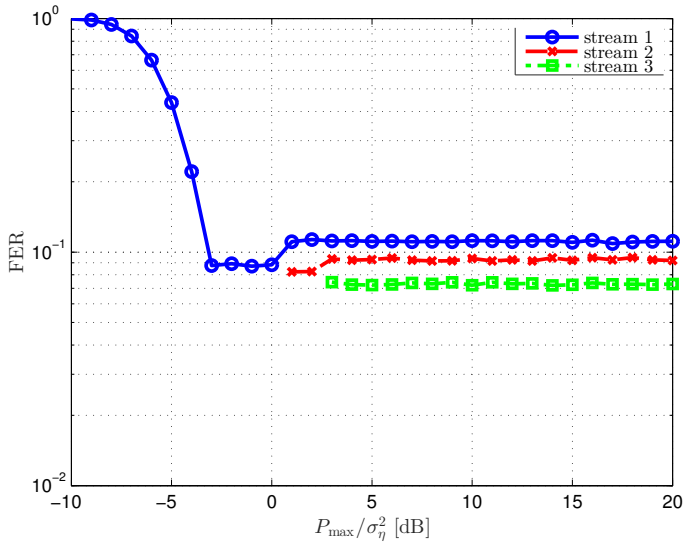

Fig. 33. FERs for three horizontally encoded parallel streams in an equicorrelated 3×4 Proakis-C channel, where $\rho = 0.50$ and $\epsilon = 0.02$. Stream 1 employed BPSK and $R_{\mathrm{c},1} = 1/3$, stream 2 employed QPSK and $R_{\mathrm{c},2} = 1/3$, while stream 3 employed QPSK and $R_{\mathrm{c},3} = 1/2$. $P_{\mathrm{max},j} = 1/N_{\mathrm{T}}$, $\forall j$.

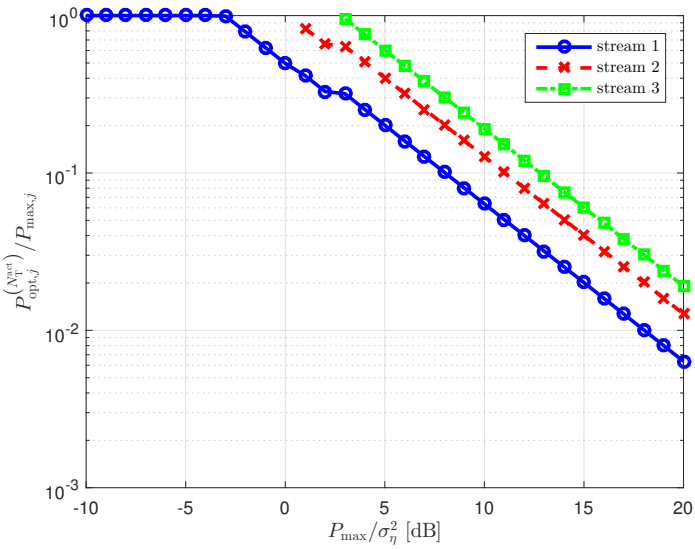

Fig. 34. $P_{\text{opt},j}^{\left(N_{\text{T}}^{\text{act}}\right)}/P_{\max,j}$ **for three horizontally encoded parallel streams in an equicorrelated** 3×4 **Proakis-C channel, where** $\rho = 0.50$ **and** $\epsilon = 0.02$**. Stream** 1 **employed BPSK and** $R_{\text{c},1} = 1/3$**, stream** 2 **employed QPSK and** $R_{\text{c},2} = 1/3$**, while stream** 3 **employed QPSK and** $R_{\text{c},3} = 1/2$**.** $P_{\max,j} = 1/N_{\text{T}}$**,** $\forall\, j$**.**

between $6.7 \cdot 10^{-2}$ and $1.25 \cdot 10^{-1}$. The FER of the third stream stays between $1.17 \cdot 10^{-1}$ and $1.75 \cdot 10^{-1}$ in the $P_{\text{tot}}/\sigma_\eta^2$ region between 1 dB and 9 dB.

As can be witnessed from Fig. 36, around 10 dB, $R_{\text{c},1}^{\text{opt}}$ and $R_{\text{c},2}^{\text{opt}}$ approach 2/3. At the same time, the FERs of all three streams in Fig. 35 increase. As was mentioned in Step B1-4 in Sect. 5.1.2, it was observed that the decoder EXIT charts become less reliable around $R_{\text{c}} = 2/3$. When streams 1 and 2 reach $R_{\text{c}}^{\max}$ in the vicinity of 15 dB, the FERs of all three streams in Fig. 35 drop. An expansion of the proposed AMC schemes, both vertical and horizontal, to 16-QAM and other higher order modulations would allow the transmitter to use more moderate code rates, i.e. below 2/3, as suggested by [102].

An interesting observation can be made when the optimised code rates of the horizontal AMC scheme are compared to the optimised code rates of the initial transmission in the vertical AMC scheme. When the transmitter increases the number of active TX antennas, or switches to QPSK or 8-PSK in Fig. 29, the optimised code rates are fairly close to $R_{\text{c}}^{\min} = 1/3$. When modulations are switched in Fig. 36, the optimised

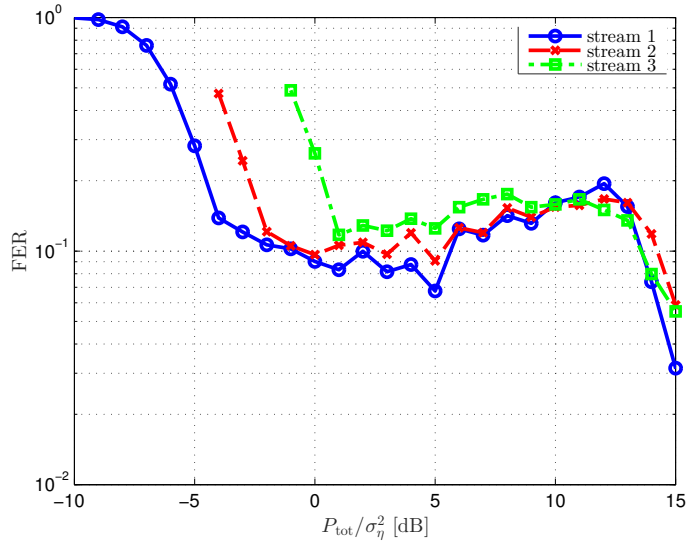

Fig. 35. The FERs for three horizontally encoded parallel streams in an uncorrelated 3×3 Proakis-C channel, with $\epsilon = 0.02$. The stream-wise powers were $P_1 = 1/2$, $P_2 = 1/3$ and $P_3 = 1/6$.

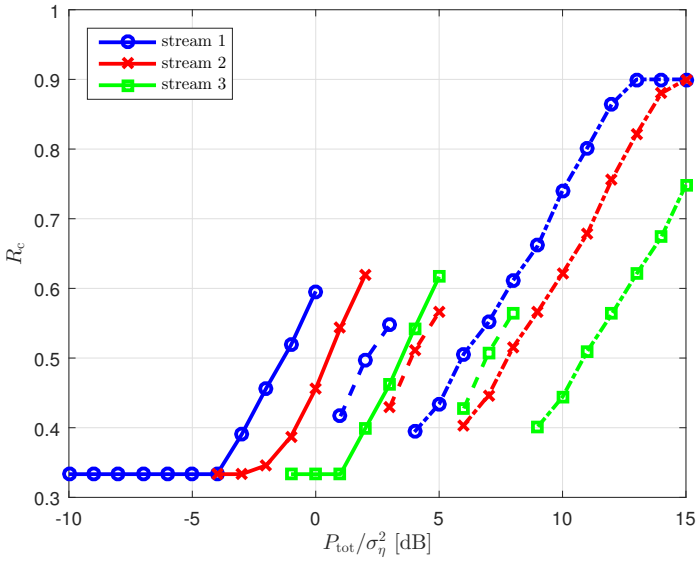

Fig. 36. The adapted modulations and code rates, $R_{\mathrm{c},j}^{\mathrm{opt}}$, for three horizontally encoded parallel streams in an uncorrelated 3×3 Proakis-C channel, with $\epsilon = 0.02$. The stream-wise powers were $P_1 = 1/2$, $P_2 = 1/3$ and $P_3 = 1/6$. The solid, dashed and dash-dotted lines denote BPSK, QPSK and 8-PSK, respectively.

code rates for all three streams are initially close to $2/5$. Thus, with QPSK and 8-PSK, the lowest code rates are avoided altogether.

5.4 Summary and discussion

Four different LA schemes that seek to obtain a target FER have been proposed and tested. Using the performance prediction method developed in Chap. 4, the transmitter iteratively adjusts either the TX power or determines an optimal MCS. The TX power adaptation scheme assumes a fixed MCS and seeks to "optimise" the channel realisation dependent equaliser transfer chart distribution. When fixed TX power is assumed, the AMC scheme is applied. The modulation order influences the distribution of the equaliser chart, while the code rate determines the position of the fixed decoder chart.

In the vertically encoded scenario, the transmitter can adaptively determine the number of active TX antennas, between which TX power is split evenly. The vertically encoded TX power control and AMC schemes are complemented by adaptive RR-HARQ and IR-HARQ schemes, respectively. The receiver provides feedback by transmitting a measured average of the absolutes of the demapped LLRs. The transmitter then uses this parameter to determine the channel quality of the initial transmission. Although the horizontal LA schemes did not consider HARQ, an interesting observation made in [311] is pointed out: when an error event occurred in a 4×4 uncorrelated spatially multiplexed MIMO system, more than 70% of the time only one or two of the four spatial streams actually contained errors. Employing HARQ with horizontally encoded spatial multiplexing would increase the number of ACK/NACK messages, but it would also lead to more efficient channel usage.

The TX power control schemes can attain the target FER once a threshold SNR value, where the transmitter can afford to reduce its TX power, is reached. Even the proposed adaptive horizontal TX power control scheme, where the interference arising from the independent parallel data streams needs to be taken into account, can produce FERs close to the target. Assuming BPSK, QPSK and 8-PSK, the AMC schemes were able to produce FERs close to the target over a 10 dB SNR range. The proposed iterative LA methods considered a singular point on the horizontal axes of the mutual information transfer charts. This was done with the purpose of reducing computational complexity. If more points were considered, the FER would remain closer to the target, while complexity would increase.

As was discussed in Sect. 2.4, regardless of the nominal CQI/LQM, it is usually linked to effective SNR/SINR in one way or another. Here the distribution of the effective SINR was used to approximate the FER. The channel model from Sect. 3.1 assumes that the channel coefficients remain constant for the duration of a transmitted packet, but are independent between packets. Thus, even with perfect receiver feedback, instantaneous effective SINR or even more detailed CSI would not help the transmitter. If sufficiently reliable SINR statistics were to be attained by measurements, a fairly large number of packets would need to be transmitted. During this learning phase, the transmission parameters could not be properly adapted. The proposed schemes require knowledge of only fundamental channel attributes, i.e. spatial channel dimensions, noise variance, the number of separable propagation paths and the eigenvalues of the RX correlation matrix. Different noise variance estimation methods have been proposed [312–317]. Even in FDD, the forward and reverse links often share the same fading distribution [176], which can help the transmitter to approximate the number of separable propagation paths.

As was illustrated in Fig. 20, the proposed LA methods could also be applied to linear receivers. Furthermore, when the transmitter determines the number of active streams or selects a suitable MCS, it need not rely on channel-specific CQI/LQM switching thresholds.

6 Conclusion

6.1 Summary and discussion

Much progress has been made since Shannon laid the groundwork by formulating the limits for error-free communication. Advances at various communication layers have allowed more efficient exploitation of the limited capacity. Many of the introduced advancements have become implementable thanks to the huge expansion of computational capacity brought by hardware development. Due to the inherent complexity of such structures and algorithms, it has become increasingly difficult to provide accurate analytical characterisation of even elementary blocks that are essential to modern communication systems. Yet, such analytical methods are very useful, since exhaustive MC simulations are often very time-consuming.

This thesis builds on prior evaluation methods that are used to approximate the behaviour of separate blocks within a communication architecture. This is accomplished by developing novel semi-analytical procedures that can be used to predict the statistical performance of a complete wireless communication system that accommodates modern breakthroughs: spatially multiplexed transmission, powerful channel coding techniques and iterative receiver processing. The transmission parameters can be adjusted flexibly. Some offline MC simulations are required to characterise the decoder's behaviour. Since the prediction method avoids all real time simulations, it can provide comparable results in a much shorter time than detailed MC simulations. Based on this robust prediction method, LA techniques that do not require instantaneous CSI were also proposed. This is a relevant design problem for rapidly changing environments, such as mobile radio channels. The adaptive TX power control and AMC schemes take into account the specific properties of the considered FD-SIC-MMSE equaliser. This is in line with the performance optimisation guidelines proposed in [68], which state that equalisation, coding and modulation should be viewed within a unified framework.

The semi-analytical performance prediction method was developed for SC-FDMA uplink scenarios. First, a condition for a successful convergence was given and a bijective connection between mutual information and LLR variance was established. It was also examined how the noise variance and instantaneous channel realisation influence the position of the FD-SIC-MMSE equaliser's mutual information transfer chart. The decoder EXIT chart is detached from the actual channel realisation, being only

dependent on the selected code rate. The following step was to study how the channel's statistical properties influence the distribution of the effective SINR at the output of the equaliser. A gamma-distribution-based method was developed for SISO and spatially uncorrelated SIMO channels, while a more robust method [167] was adapted to evaluate the effective SINR distribution of RX correlated MIMO channels. The MIMO channel distribution prediction method can also be used with SISO and uncorrelated SIMO channels, but the gamma-distribution-based method is computationally faster. The distribution of the LLR variance can be derived directly from the distribution of the effective SINR.

The core contribution of this thesis is built around the discovery that the demapper output's LLR variance distribution and the decoder's EXIT chart can be utilised to predict the performance of the receiver. Using the bijective connection between LLR variance and mutual information, it is possible to approximate the probability that the equaliser of random channel realisation intersects the fixed decoder chart at any given point along the chart. Based on the maximum of such probabilities, the FER can be predicted for SISO/SIMO channels and vertically encoded MIMO systems, as well as for horizontally encoded and MU-MIMO systems, where each stream has its own TX power, modulation and code rate. The predicted and MC simulated results were closely matched under multiple scenarios.

The proposed performance prediction method is not advocated as a complete replacement for detailed MC simulations, which will always be needed. However, the prediction method can produce comparable results in a much shorter time than the simulation model. With SISO and uncorrelated SIMO channels, it only takes seconds to produce results. It takes a longer time to compute the results for MIMO channels. This is due to the fact that in order to form the SINR distribution, it is necessary to solve a saddle point value at each considered point along the SINR axis. RX correlation also has an impact on the duration of the prediction. For uncorrelated channels, the prediction is faster than for correlated channels. If the RX correlation matrix has multiple different eigenvalues, as is the case with exponential correlation, the prediction is slower than in the case where there are few unique eigenvalues (always two, when equicorrelation is assumed). Regardless of correlation, the prediction method produces results for vertically encoded systems within a couple of hours. The addition of RR-HARQ does not increase the duration. In the case of horizontally encoded transmission, the prediction tool needs to take into account the parallel streams, which may or may not be cancelled out. With the addition of each TX antenna, the prediction duration is roughly

doubled. This still compares favourably to the MC simulations, which took days to complete. When RR-HARQ was involved, the MC simulations could take a couple of weeks. Furthermore, the prediction tool can be streamlined in order to reduce the number of unnecessary computations.

It is necessary to point out three potentially problematic aspects in the proposed performance prediction method. The iterative receiver utilises the decoder's *a posteriori* LLRs in the soft bit-to-symbol conversion. However, the information and parity bit LLRs at the output of a turbo decoder have distinct Gaussian distributions. As a consequence, their joint distribution is not Gaussian. The equaliser nevertheless assumes that the soft symbol estimates that it uses in SIC are formed from Gaussian IID LLRs, which leads to suboptimal performance. Mutual information transfer charts are built around the premise that the associated distributions are Gaussian. Therefore, a decoder *a posteriori* transfer chart drawn from the non-Gaussian joint distribution of the information and parity bit LLRs could not adequately capture the receiver's (possible) convergence. It was discovered that an EXIT chart drawn solely from the information bit LLRs could sufficiently accurately capture the convergence trajectory.

A second noteworthy issue arises in the CLT approximation of the SINR's distribution across the frequency bandwidth. There would be no need for such an approximation in flat fading or ISI-free channels, but with a finite number of separable channel taps and RX antennas, the CLT approximation cannot be expected to hold tightly. Thirdly, the Nakagami distribution, which is used to emulate the LLR variance, is merely a convenient approximation. Despite these approximations, the results illustrate that the proposed prediction method is robust enough to be useful even with SISO and 2×2 MIMO channels, and with three channel taps.

A second novel contribution was the development of LA techniques that exploit the described performance prediction method. By iteratively adjusting TX power or code rate in conjunction with modulation, a target FER could be attained. Beyond a threshold point, where the transmitter can afford to drop its power, adaptive TX power control schemes designed for vertically and horizontally encoded systems produce near-constant FERs. Vertical and horizontal AMC schemes produced FERs close to the target over an approximately 10 dB SNR span. The vertically encoded TX power control and AMC techniques were complemented by adaptive RR-HARQ and IR-HARQ methods, respectively, which utilised a mean of the absolute LLRs collected at the equaliser output to optimise the TX power of the retransmitted packet and the number of additional

IR parity bits, respectively. The transmitter can also adaptively select the appropriate number of active antennas.

The LA scheme would be particularly effective with rapidly changing channels, where the receiver feedback does not allow the transmitter to adjust its TX parameters quickly enough. The LA schemes do not require, nor would they directly benefit from, instantaneous CSIT. Since only fundamental channel parameters, i.e. channel dimensions, noise variance, the number of separable propagation paths and the eigenvalues of the RX correlation matrix, are needed to approximate the equaliser output's effective SINR distribution, statistical LA can be performed without channel measurements. In 5G networks, where the role of the base stations may be reduced in intra-cell communications, the proposed method could possibly provide a way to perform effective device-to-device LA with low feedback requirement. However, in its current form, the proposed scheme is arguably prohibitively complex from the implementation perspective and would require further work.

6.2 Future work

There are some long-standing research problems related to iterative processing. An analytical framework, which would accurately formalise or quantify the differences that arise from the use of *a posteriori* and extrinsic information in iterative receiver processing, is still lacking. The success of EXIT charts and related convergence tracking tools is based on the assumption that the associated bit and symbol sequences can be represented as Gaussian densities, which in turn are defined by a single parameter. The soft demapped bits of higher order modulations, i.e. QAM, do not fall into Gaussian densities. Furthermore, even if the input LLR distributions were Gaussian, powerful modern decoders typically produce distorted output LLR distributions. The phenomenon is not restricted to turbo decoding. During the preparation of this thesis, it was noted that a sum product algorithm that operated on WiMAX standard LDPC codes also produced non-Gaussian output LLR distributions. Thus, any robust convergence tracking tool that could take into account non-Gaussian distributions would be highly valuable.

Obviously, there are numerous potential avenues for research that relate directly to the proposed performance prediction method and LA algorithms. The robustness of the proposed method should be further studied by considering different FEC techniques, such as convolutional, LDPC and RA codes. In general, codes that can be described by factor graphs and decoded by belief propagation algorithms would merit consideration.

It would also be possible to assign different FEC techniques to different streams/users in horizontally encoded / MU-MIMO scenarios. The SINR distributions of ZF filters were already developed in [167]. Another issue would be to study how accurate the LLR variance distribution's Nakagami-approximation would be with different channel delay profiles.

It was mentioned in [167] that by combining its results with those from [318], the SINR PDFs could be expanded for frequency-selective MIMO channels. The proposed frequency-selective SINR distributions could not be applied within the context of this thesis, because SC-FDMA systems suffer from ISI. This necessitated the use of the CLT approximation in the derivation of the frequency-selective SINR distribution. However, in the case of OFDMA systems, where the subchannels are frequency flat, a highly accurate SINR distribution can be derived. This also means that for OFDMA, a highly accurate LLR variance distribution could be obtained (for BPSK and QPSK) and used instead of the Nakagami-approximation.

An obvious and practically relevant topic for future work would be an expansion for 16-QAM and other higher order modulations, since they are included in modern wireless communication standards. The 16-QAM coefficients for the approximate J-function can be found in [120, 298]. During the preparation of this thesis, it was noticed that the prediction method could not reach the same level of accuracy with 16-QAM as with the lower order modulations. This can be attributed to the observation that the distributions of demapped LLRs significantly deviate from the Gaussian distribution that is assumed in conjunction with EXIT charts. A possible solution would be to form decoder EXIT charts, where the input LLR distributions follow the observed demapped 16-QAM LLR distributions instead of the ideal Gaussian distribution.

It was assumed that the turbo decoder's constituent decoders exchange extrinsic information only between each other. If there were alternative activation schedules, where the constituent decoders could exchange information between themselves and the equaliser (or detector), the convergence analysis would be transported from a two-dimensional plane to a three-dimensional space. The performance prediction method would still be applicable, since the EXIT surfaces of both constituent decoders are independent of the channel realisation, meaning that their positions would remain fixed. The evaluation of the intersection probability would take place in two dimensions across the equaliser's (or detector's) surface, whose position is determined by the channel realisation.

Another practical research topic would be the inclusion of a channel estimator. In [149], the convergence of an iterative receiver, which included a least-squares channel estimator, was studied through EXIT analysis. With three iterative components, the convergence analysis would again be done in three dimensions. The decoder's and channel estimator's surfaces are independent, while the equaliser (or detector) surface's position is determined by the channel realisation.

The performance prediction method has already illustrated considerable flexibility and superior speed in comparison to a traditional MC simulator. Some of the proposed future research topics are quite feasible, although admittedly arduous. Although a strict MU scenario was not considered in example cases, the horizontally encoded transmission mode is very close to it. The average powers of the tap delay profiles were identical, but this was only due to the rigidity of the channel simulator. If the performance predictions can exhibit similar dependability with additional features, it would be interesting to see how the prediction tool, or some of its detached features, would fare against system level simulators, which can be notoriously slow. As such, the prediction method, or its detached features, could help bridge the gap between the link and system levels.

The proposed LA algorithms are iterative and thereby arguably prohibitively complex from the implementation perspective. Therefore, it would be sensible to examine ways to reduce their computational complexity. One such possibility would relate to the receiver's predictable error correcting capability that is independent of the chosen modulation. In AWGN channels, the coded BER and FER curves of different MCSs have very similar shapes [192, 217, 218, 220, 319]. This does not necessarily hold for frequency-selective fading channels. Interpreting the ETSI-A channel simulation results from [319], it seems that the code rate determines the shape of the FER graphs, while modulation, effectively the bit-to-noise ratio, determines their positions on the SNR axis. This observation could possibly be exploited when performing LA for SISO/SIMO or vertically encoded MIMO systems in spatially uncorrelated channels. If a few FER graphs for different code rates were computed off-line, the transmitter could adjust either its TX power or MCS rapidly. The rough TX power adaptation in Step A1-2 in Sect. 5.1.1 produces an FER of approximately $1/2$. If the transmitter knew the shape of the FER curve, it would know how much it should adjust its power from that initial estimate to reach the target FER. If the transmitter had a set of FER graphs for different code rates and a particular modulation, it could approximate what MCS would reach the target FER and offer optimal throughput, given a particular SNR value. This approach

would not be compatible with horizontally encoded or MU-MIMO systems, where the SIC influences the shapes of the FER graphs.

The combination of horizontally encoded spatial multiplexing and HARQ may lead to more efficient channel usage [311], since HARQ transmissions are only required on a stream-wise basis. The proposed horizontal LA schemes only seek to attain the target FER for a singular transmission of a packet. It would be interesting to see what would happen to the system performance if the adaptive HARQ schemes that were developed for the vertically encoded scenario were applied in the horizontally encoded scenario. With the adaptive RR-HARQ scheme, the power levels of the parallel streams would vary. This, along with the altered decoder EXIT charts associated with the IR transmissions, makes the system performance unpredictable. Since the adaptive RR-HARQ scheme would reduce the average CAI and the adaptive IR-HARQ scheme would instantaneously lower the decoder EXIT charts, the stream-wise FERs of the initial transmissions would probably be lower than in the studied pure FEC case.

A major issue arises from the observation that even a limited feedback from the receiver that provides the transmitter with a CQI/LQM can potentially enable near optimal LA [176, 177]. If the computational complexity was reduced to a reasonable level, it would be worthwhile to study how the proposed LA techniques can be applied under imperfect CSIT. Currently, it would be highly impractical to iteratively adapt the appropriate TX parameters for each channel realisation.

References

1. Noble DE (1962) The history of land-mobile radio communications. Proceedings of the IRE 50(5): 1405–1414.
2. Chandran N & Valenti MC (2001) Three generations of cellular wireless systems. IEEE Potentials 20(1): 32–35.
3. Kucar AD (1991) Mobile radio: An overview. IEEE Communications Magazine 29(11): 72–85.
4. Furuskär A, Mazur S, Müller F & Olofsson H (1999) EDGE: Enhanced data rates for GSM and TDMA/136 evolution. IEEE Personal Communications Magazine 6(3): 56–66.
5. Dahlman E, Parkvall S, Sköld J & Beming P (2008) 3G Evolution: HSPA and LTE for Mobile Broadband. Academic Press, Oxford, UK, second edition.
6. Holma H & Toskala A (2010) WCDMA for UMTS: HSPA Evolution and LTE. John Wiley & Sons Ltd, Chichester, UK, fifth edition.
7. Forney GD (1970) Convolutional codes I: Algebraic structure. IEEE Transactions on Information Theory 16(6): 720–738.
8. Berrou C & Glavieux A (1996) Near optimum error correcting coding and decoding: Turbo-codes. IEEE Transactions on Communications 44(10): 1261–1271.
9. Holma H & Toskala A (2011) LTE for UMTS: Evolution to LTE-Advanced. John Wiley & Sons Ltd, Chichester, UK, second edition.
10. IEEE Computer Society and the IEEE Microwave Theory and Techniques Society (2005) IEEE standard for local and metropolitan area networks; Part 16: Air interface for fixed and mobile broadband wireless access systems; Amendment 2: Physical and medium access control layers for combined fixed and mobile operation in licensed bands; and corrigendum 1. IEEE Std 802.16e-2005, IEEE.
11. Dahlman E, Parkvall S & Sköld J (2011) 4G: LTE/LTE-advanced for Mobile Broadband. Academic Press, Kidlington, UK.
12. IEEE Computer Society and the IEEE Microwave Theory and Techniques Society (2011) IEEE standard for local and metropolitan area networks part 16: Air interface for fixed and mobile broadband wireless access systems; Amendment 3: Advanced air interface. IEEE Std 802.16m-2011, IEEE.
13. Pi Z & Khan F (2011) An introduction to millimeter-wave mobile broadband systems. IEEE Communications Magazine 49(6): 101–107.
14. Rappaport TS, Sun S, Mayzus R, Zhao H, Azar Y, Wang K, Wong GN, Schulz JK, Samini M & Gutierrez F (2013) Millimeter wave mobile communications for 5G cellular: It will work! IEEE Access 1: 335–349.
15. Demesthicas P, Georgakopoulos A, Karvounas D, Tsagkaris K, Stavroulaki V, Lu J, Xiong C & Yao J (2013) 5G on the horizon: Key challenges for the radio-access network. IEEE Vehicular Technology Magazine 8(3): 47–53.
16. Boccardi F, Heath RW, Lozano A, Marzetta TL & Popovski P (2014) Five disruptive technology directions for 5G. IEEE Communications Magazine 52(2): 74–80.
17. Bhushan N, Li J, Malladi D, Gilmore R, Brenner D, Damjanovic A, Sukhavasi RT, Patel C & Geirhofer S (2014) Network densification: The dominant theme for wireless evolution into 5G. IEEE Communications Magazine 52(5): 82–89.

18. Bangerter B, Talwar S, Arefi R & Stewart K (2014) Networks and devices for the 5G era. IEEE Communications Magazine 52(2): 90–96.
19. Wang CX, Haider F, Gao X, You XH, Yang Y, Yuan D, Aggoune HM, Haas H, Fletcher S & Hepsaydir E (2014) Cellular architecture and key technologies for 5G wireless communication networks. IEEE Communications Magazine 52(2): 122–130.
20. Osseiran A, Boccardi F, Braun V, Kusume K, Marsch P, Maternia M, Queseth O, Schellmann M, Schotten H, Taoka H, Tullberg H, Uusitalo MA, Timus B & Fallgren M (2014) Scenarios for 5G mobile and wireless communications: The vision of the METIS project. IEEE Communications Magazine 52(5): 26–35.
21. Chen S & Zhao J (2014) The requirements, challenges, and technologies for 5G of terrestrial mobile telecommunication. IEEE Communications Magazine 52(5): 36–43.
22. Jungnickel V, Manolakis K, Zirwas W, Panzner B, Braun V, Lossow M, Sternad M, Apelfröjd R & Svensson T (2014) The role of small cells, coordinated multipoint, and massive MIMO in 5G. IEEE Communications Magazine 52(5): 44–51.
23. Rost P, Bernardos CJ, De Domenico A, Di Girolamo M, Lalam M, Maeder A, Sabella D & Wübben D (2014) Cloud technologies for flexible 5G radio access networks. IEEE Communications Magazine 52(5): 68–76.
24. Tehrani MN, Uysal M & Yanikomeroglu H (2014) Device-to-device communication in 5G cellular networks: Challenges, solutions, and future directions. IEEE Communications Magazine 52(5): 86–92.
25. Hu R & Qian Y (2014) An energy efficient and spectrum efficient wireless heterogeneous network framework for 5G systems. IEEE Communications Magazine 52(5): 94–101.
26. Andrews JG, Buzzi S, Choi W, Hanly SV, Lozano A, Soong ACK & Zhang JC (2014) What will 5G be? IEEE Journal on Selected Areas in Communications 32(6): 1065–1082.
27. Wübben D, Rost P, Bartelt J, Lalam M, Savin V, Gorgoglione M, Dekorsy A & Fettweis G (2014) Benefits and impact of cloud computing on 5G signal processing: Flexible centralization through cloud-RAN. IEEE Signal Processing Magazine 31(6): 35–44.
28. Marzetta TL (2010) Noncooperative cellular wireless with unlimited numbers of base station antennas. IEEE Transactions on Wireless Communications 9(11): 3590–3600.
29. Rusek F, Persson D, Lau BK, Larsson EG, Marzetta TL, Edfors O & Tufvesson F (2013) Scaling up MIMO: Opportunities and challenges with very large arrays. IEEE Signal Processing Magazine 30(1): 40–60.
30. Hoydis J, ten Brink S & Debbah M (2013) Massive MIMO in the UL/DL of cellular networks: How many antennas do we need? IEEE Journal on Selected Areas in Communications 31(2): 160–171.
31. Larsson EG, Edfors O, Tufvesson F & Marzetta TL (2014) Massive MIMO for next generation wireless systems. IEEE Communications Magazine 52(2): 186–195.
32. Chandrasekar V, Andrews JG & Gatherer A (2008) Femtocell networks: A survey. IEEE Communications Magazine 46(9): 59–67.
33. Chang RW & Gibby RA (1968) A theoretical study of performance of an orthogonal multiplexing data transmission scheme. IEEE Transactions on Communications 16(4): 529–540.
34. Weinstein SB & Ebert PM (1971) Data transmission by frequency-division multiplexing using the discrete Fourier transform. IEEE Transactions on Communications 19(5): 628–634.

35. Berardinelli G, Maestro Ruiz de Temiño LA, Frattasi S, Rahman MI & Mogensen P (2008) OFDMA vs. SC-FDMA: Performance comparison in local area IMT-A scenarios. IEEE Communications Magazine 15(5): 64–72.
36. Cox C (2012) An Introduction to LTE: LTE, LTE-Advanced, SAE and 4G Mobile Communications. John Wiley & Sons Ltd., Chichester, UK.
37. Winters JH (1987) On the capacity of radio communication systems with diversity in a Rayleigh fading environment. IEEE Journal on Selected Areas in Communications 5(5): 871–878.
38. Winters JH, Salz J & Gitlin RD (1994) The impact of antenna diversity on the capacity of wireless communication systems. IEEE Journal on Selected Areas in Communications 42(2/3/4): 1740–1751.
39. Foschini GJ & Gans MJ (1998) On limits of wireless communications in a fading environment when using multiple antennas. Wireless Personal Communications, Kluwer Academic Publishers 6(3): 311–335.
40. Telatar E (1999) Capacity of multi-antenna Gaussian channels. European Transactions on Telecommunications 10(6): 585–595.
41. Alamouti S (1998) A simple transmit diversity technique for wireless communications. IEEE Journal on Selected Areas in Communications 16(8): 1451–1458.
42. Tarokh V, Jafarkhani H & Calderbank AR (1999) Space–time block codes from orthogonal designs. IEEE Transactions on Information Theory 45(5): 1456–1467.
43. Tarokh V, Jafarkhani H & Calderbank AR (1999) Space–time block coding for wireless communications: Performance results. IEEE Journal on Selected Areas in Communications 17(3): 451–460.
44. Tarokh V, Seshadri N & Calderbank AR (1998) Space–time codes for high data rate wireless communication: Performance criterion and code construction. IEEE Transactions on Information Theory 44(2): 744–765.
45. Tarokh V, Naguib A, Seshadri N & Calderbank AR (1999) Space–time codes for high data rate wireless communication: Performance criteria in the presence of channel estimation errors, mobility and multiple paths. IEEE Transactions on Communications 47(2): 199–207.
46. El Gamal H, Hammons AR, Liu Y, Fitz MP & Takeshita OY (2003) On the design of space–time and space–frequency codes for MIMO frequency-selective fading channels. IEEE Transactions on Information Theory 49(9): 2277–2292.
47. Bauch G (1999) Concatenation of space-time block codes and "turbo"-TCM. In: Proceedings of the IEEE International Conference on Communications, volume 2, pp. 1202–1206. Vancouver, BC, Canada.
48. Lin X & Blum RS (2000) Improved space–time codes using serial concatenation. IEEE Communications Letters 4(7): 221–223.
49. Stefanov A & Duman TM (2001) Turbo-coded modulation for systems with transmit and receive antenna diversity over block fading channels: System model, decoding approaches, and practical considerations. IEEE Journal on Selected Areas in Communications 19(5): 958–968.
50. Liu Y, Fitz MP & Takeshita OY (2001) Full rate space–time turbo codes. IEEE Journal on Selected Areas in Communications 19(5): 969–980.
51. Cui D & Haimovich AM (2001) Performance of parallel concatenated space–time codes. IEEE Communications Letters 5(6): 236–238.

52. Firmanto W, Vucetic B, Yuan J & Chen Z (2002) Space-time turbo trellis coded modulation for wireless data communications. EURASIP Journal on Applied Signal Processing 2002(5): 459–470.
53. Bahceci I & Duman TM (2002) Combined turbo coding and unitary space-time modulation. IEEE Transactions on Communications 50(8): 1244–1249.
54. Tujkovic D (2003) Space-Time Turbo Coded Modulation for Wireless Communication Systems. Number C184 in Acta Universitatis Ouluensis, D.Sc. (Tech.) thesis. University of Oulu, Oulu, Finland.
55. Hong Y, Yuan J, Chen Z & Vucetic B (2004) Space–time turbo trellis codes for two, three, and four transmit antennas. IEEE Transactions on Vehicular Technology 53(2): 318–328.
56. Foschini G (1996) Layered space-time architecture for wireless communication in a fading environment when using multi-element antennas. Bell Labs Technical Journal 1(2): 41–59.
57. Li X, Huang H, Foschini GJ & Valenzuela RA (2000) Effects of iterative detection and decoding on the performance of BLAST. In: Proceedings of the IEEE Global Telecommunication Conference, volume 2, pp. 1061–1066. San Francisco, CA, USA.
58. Zheng L & Tse DNC (2003) Diversity and multiplexing: A fundamental tradeoff in multiple-antenna channels. IEEE Transactions on Information Theory 49(5): 1073–1096.
59. Lozano A & Jindal N (2010) Transmit diversity vs. spatial multiplexing in modern MIMO systems. IEEE Transactions on Wireless Communications 9(1): 186–197.
60. Gesbert D, Shafi M, Shiu D, Smith PJ & Naguib A (2003) From theory to practice: An overview of MIMO space–time coded wireless systems. IEEE Journal on Selected Areas in Communications 21(3): 281–302.
61. Paulraj AJ, Gore DA, Nabar RU & Bölcskei H (2004) An overview of MIMO communications—a key to gigabit wireless. Proceedings of the IEEE 92(2): 198–218.
62. Mietzner J, Schober R, Lampe L, Gerstacker WH & Hoeher PA (2009) Multiple-antenna techniques for wireless communications—a comprehensive literature survey. IEEE Communications Surveys & Tutorials 11(2): 87–105.
63. Tse D & Viswanath P (2005) Fundamentals of wireless communication. Cambridge University Press, Cambridge, UK.
64. 3rd Generation Partnership Project (3GPP) Technical Specification Group Radio Access Network (2016) Multiplexing and channel coding. TS 36.212 v13.0.0, 3rd Generation Partnership Project (3GPP).
65. Benelli G (1985) An ARQ scheme with memory and soft error detectors. IEEE Transactions on Communications 33(3): 285–288.
66. Chase D (1985) Code combining—a maximum-likelihood decoding approach for combining an arbitrary number of noisy packets. IEEE Transactions on Communications 33(5): 385–393.
67. Larsson P, Rasmussen LK & Skoglund M (2014) Throughput analysis of ARQ schemes in Gaussian block fading channels. IEEE Transactions on Communications 62(7): 2569–2588.
68. Biglieri E, Proakis J & Shamai S (1998) Fading channels: Information theoretic and communications aspects. IEEE Transactions on Information Theory 44(6): 2619–2692.
69. Mandelbaum DM (1974) An adaptive-feedback coding scheme using incremental redundancy. IEEE Transactions on Information Theory 20(3): 388–389.
70. Huusko J, Karjalainen J & Juntti M (2010) Statistical performance prediction method for an iterative receiver with Chase combining. In: Proceedings of the International Symposium on Turbo Codes and Iterative Information Processing, pp. 349–353. Brest, France.

71. Huusko J, Karjalainen J & Juntti M (2010) On performance prediction of an iterative multi-antenna receiver. In: Proceedings of the Annual Asilomar Conference on Signals, Systems and Computers, pp. 741–745. Pacific Grove, CA, USA.
72. Huusko J, Pyhtilä J & Juntti M (2014) On predicting the performance of an iterative MIMO MMSE receiver with vertical encoding. In: Proceedings of the IEEE Global Telecommunication Conference, pp. 1510–1515. Austin, TX, USA.
73. Huusko J, Pyhtilä J & Juntti M (2014) A semi-analytical performance prediction method for an iterative MIMO MMSE receiver with forward and backward error control. IEEE Transactions on Communications 62(12): 4198–4210.
74. Huusko J, Pyhtilä J & Juntti M (2015) Utilizing the statistical properties of a MIMO channel in transmission optimization. In: Proceedings of the International ITG Conference on Systems, Communications and Coding, pp. 1–6. Hamburg, Germany.
75. Shannon CE (1948) A mathematical theory of communications. The Bell System Technical Journal 27: 379–423, 623–656.
76. Viterbi AJ (1967) Error bounds for convolutional codes and an asymptotically optimum decoding algorithm. IEEE Transactions on Information Theory 13(2): 260–269.
77. Viterbi AJ (1971) Convolutional codes and their performance in communication systems. IEEE Transactions on Communication Technology 19(5): 751–772.
78. Bahl LR, Cocke J, Jelinek F & Raviv J (1974) Optimal decoding of linear codes for minimizing symbol error rate. IEEE Transactions on Information Theory 20(2): 284–287.
79. Benedetto S, Montorsi G, Divsalar D & Pollara F (1996) A soft-input soft-output maximum a posteriori (MAP) module to decode parallel and serial concatenated codes. TDA Progress Report 42-127, Jet Propulsion Laboratory, Pasadena, CA, USA.
80. Robertson P, Hoeher P & Villebrun E (1997) Optimal and sub-optimal maximum a posteriori algorithms suitable for turbo decoding. European Transactions on Telecommunications 8(2): 119–125.
81. Valenti MC & Sun J (2001) The UMTS turbo code and an efficient decoder implementation suitable for software-defined radios. International Journal of Wireless Information Networks 8(4): 203–215.
82. Benedetto S & Montorsi G (1996) Unveiling turbo codes: Some results on parallel concatenated coding schemes. IEEE Transactions on Information Theory 42(2): 409–428.
83. Perez LC, Seghers J & Costello DJ (1996) A distance spectrum interpretation of turbo codes. IEEE Transactions on Information Theory 42(6): 1698–1709.
84. Benedetto S & Montorsi G (1996) Design of parallel concatenated convolutional codes. IEEE Transactions on Communications 44(5): 591–600.
85. Hagenauer J (1997) The turbo principle: Tutorial introduction and state of the art. In: Proceedings of the International Symposium on Turbo Codes and Related Topics, pp. 1–11. Brest, France.
86. Zehavi E (1992) 8-PSK trellis codes for a Rayleigh channel. IEEE Transactions on Communications 40(5): 873–884.
87. Caire G, Taricco G & Biglieri E (1998) Bit-interleaved coded modulation. IEEE Transactions on Information Theory 44(3): 927–946.
88. Ungerboeck G (1982) Channel coding with multilevel/phase signals. IEEE Transactions on Information Theory 28(1): 55–67.
89. Le Goff S, Glavieux A & Berrou C (1994) Turbo-codes and high spectral efficiency modulation. In: Proceedings of the IEEE International Conference on Communications,

volume 2, pp. 645–649. New Orleans, LA, USA.
90. Benedetto S, Divsalar D, Montorsi G & Pollara F (1998) Serial concatenation of interleaved codes: Performance analysis, design, and iterative decoding. IEEE Transactions on Information Theory 44(3): 909–926.
91. Gallager RG (1963) Low-Density Parity-Check Codes. MIT Press, Cambridge, MA, USA.
92. Tanner RM (1981) A recursive approach to low complexity codes. IEEE Transactions on Information Theory 27(5): 533–547.
93. MacKay DJC & Neal RM (1996) Near Shannon limit peroformance of low density parity check codes. IEE Electronics Letters 32(18): 1645–1646.
94. Richardson TJ & Urbanke RL (2001) Capacity of low-density parity-check codes under message-passing decoding. IEEE Transactions on Information Theory 47(2): 599–618.
95. Richardson TJ, Shokrollahi MA & Urbanke RL (2001) Design of capacity-approaching irregular low-density parity-check codes. IEEE Transactions on Information Theory 47(2): 619–637.
96. Chung SY, Forney GD, Richardson TJ & Urbanke R (2001) On the design of low-density parity-check codes within 0.0045 dB of the Shannon limit. IEEE Communications Letters 5(2): 58–60.
97. Hou J, Siegel PH & Milstein LB (2001) Performance analysis and code optimization of low density parity-check codes on Rayleigh fading channels. IEEE Journal on Selected Areas in Communications 19(5): 924–934.
98. Divsalar D, Jin H & McEliece RJ (1998) Coding theorems for "turbo-like" codes. In: Proceedings of the Annual Allerton Conference on Communications, Control, and Computing, pp. 201–210. Monticello, IL, USA.
99. Jin H, Khandekar A & McEliece R (2000) Irregular repeat–accumulate codes. In: Proceedings of the International Symposium on Turbo Codes and Related Topics, pp. 1–8. Brest, France.
100. McEliece RJ, MacKay DJC & Cheng JF (1998) Turbo decoding as an instance of Pearl's "belief propagation" algorithm. IEEE Journal on Selected Areas in Communications 16(2): 140–152.
101. Hagenauer J & Hoeher P (1989) A Viterbi algorithm with soft-decision outputs and its applications. In: Proceedings of the IEEE Global Telecommunication Conference, volume 3, pp. 1680–1686. Dallas, TX, USA.
102. Hagenauer J, Offer E & Papke L (1996) Iterative decoding of binary block and convolutional codes. IEEE Transactions on Information Theory 42(2): 429–445.
103. Wiberg N, Loeliger HA & Kötter R (1995) Codes and iterative decoding on general graphs. European Transactions on Telecommunications 6(5): 513–525.
104. Kschischang FR, Frey BJ & Loeliger HA (2001) Factor graphs and the sum-product algorithm. IEEE Transactions on Information Theory 47(2): 498–519.
105. Douillard C, Jézéquel M, Berrou C, Picart A, Didier P & Glavieux A (1995) Iterative correction of intersymbol interference: Turbo-equalization. European Transactions on Telecommunications 6(5): 507–511.
106. Tüchler M, Singer AC & Koetter R (2002) Minimum mean squared error equalization using *a priori* information. IEEE Transactions on Signal Processing 50(3): 673–683.
107. Tüchler M, Koetter R & Singer AC (2002) Turbo equalization: Principles and new results. IEEE Transactions on Communications 50(5): 754–767.

108. Otnes R & Tüchler M (2002) EXIT chart analysis applied to adaptive turbo equalization. In: Proceedings of the Nordic Signal Processing Symposium. On Hurtigruten (Tromsø–Trondheim), Norway.
109. Dejonghe A & Vandendorpe L (2004) Bit-interleaved turbo equalization over static frequency-selective channels: Constellation mapping impact. IEEE Transactions on Communications 52(12): 2061–2065.
110. Xiao P, Carrasco R & Wassell I (2006) EXIT chart analysis of space-time turbo equalizer. In: Proceedings of the IEEE Information Theory Workshop, pp. 631–635. Punta del Este, Uruguay.
111. Lou H & Xiao C (2011) Soft-decision feedback turbo equalization for multilevel modulations. IEEE Transactions on Signal Processing 59(1): 186–195.
112. Polprasert C & Ritcey JA (2012) Performance analysis of the bit-interleaved coded modulation using turbo equalization with single carrier frequency domain equalization over fast fading channels. Signal Processing, Elsevier Publishing Company 92(12): 3026–3031.
113. Lee SJ, Singer AC & Shanbhag NR (2005) Linear turbo equalization analysis via BER transfer and EXIT charts. IEEE Transactions on Signal Processing 53(8): 2883–2897.
114. Ramon V, Herzet C & Vandendorpe L (2007) A semi-analytical method for predicting the performance and convergence behavior of a multiuser turbo-equalizer/demapper. IEEE Transactions on Signal Processing 55(3): 1104–1117.
115. Yuan X, Guo Q, Wang X & Ping L (2008) Evolution analysis of low-cost iterative equalization in coded linear systems with cyclic prefixes. IEEE Journal on Selected Areas in Communications 26(2): 301–310.
116. Sellami N, Roumy A & Fijalkow I (2008) A proof of convergence of the MAP turbo-detector to the AWGN case. IEEE Transactions on Signal Processing 56(4): 1548–1561.
117. Assimi AN, Poulliat C & Fijalkow I (2008) Packet combining for turbo-diversity in HARQ systems with integrated turbo-equalization. In: Proceedings of the International Symposium on Turbo Codes and Related Topics, pp. 61–66. Lausanne, Switzerland.
118. Narayanan KR, Wang X & Yue G (2005) Estimating the PDF of the SIC-MMSE equalizer output and its applications in designing LDPC codes with turbo equalization. IEEE Transactions on Wireless Communications 4(1): 278–287.
119. Laot C, Le Bidan R & Leroux D (2005) Low-complexity MMSE turbo equalization: A possible solution for EDGE. IEEE Transactions on Wireless Communications 4(3): 965–974.
120. Kansanen K & Matsumoto T (2007) An analytical method for MMSE MIMO turbo equalizer EXIT chart computation. IEEE Transactions on Wireless Communications 6(1): 59–63.
121. Karjalainen J, Veselinović N, Kansanen K & Matsumoto T (2007) Iterative frequency domain joint-over-antenna detection in multiuser MIMO. IEEE Transactions on Wireless Communications 6(10): 3620–3631.
122. Sabbaghian M & Falconer DD (2009) An analytical approach for finite block length performance analysis of turbo frequency-domain equalization. IEEE Transactions on Vehicular Technology 58(3): 1292–1301.
123. Assimi AN, Poulliat C & Fijalkow I (2008) Distance distribution for turbo-equalized systems over static frequency selective channels. In: Proceedings of the IEEE International Conference on Acoustics, Speech, and Signal Processing, pp. 2949–2952. Las Vegas, NV, USA.

124. Richardson T (2000) The geometry of turbo-decoding dynamics. IEEE Transactions on Information Theory 46(1): 9–23.
125. Agrawal D & Vardy A (2001) The turbo decoding algorithm and its phase trajectories. IEEE Transactions on Information Theory 47(2): 699–722.
126. Rusmevichientong P & Van Roy B (2001) An analysis of belief propagation on the turbo decoding graph with Gaussian densities. IEEE Transactions on Information Theory 47(2): 745–765.
127. Duan L & Rimoldi B (2001) The iterative turbo decoding algorithm has fixed points. IEEE Transactions on Information Theory 47(7): 2993–2995.
128. Ikeda S, Tanaka T & Amari SI (2004) Information geometry of turbo and low-density parity-check codes. IEEE Transactions on Information Theory 50(6): 1097–1114.
129. Yedidia JS, Freeman WT & Weiss Y (2005) Constructing free energy approximations and generalized belief propagation algorithms. IEEE Transactions on Information Theory 51(7): 2282–2312.
130. Walsh JM, Regalia PA & Johnson CR (2006) Turbo decoding as iterative constrained maximum-likelihood sequence detection. IEEE Transactions on Information Theory 52(12): 5426–5437.
131. Reid AC, Gulliver TA & Taylor DP (2001) Convergence and errors in turbo-decoding. IEEE Transactions on Communications 49(12): 2045–2051.
132. Fu M (2005) Stochastic analysis of turbo decoding. IEEE Transactions on Information Theory 51(1): 81–100.
133. Wiberg N (1996) Codes and Decoding on General Graphs. Number 440 in Linköping Studies in Science and Technology, Ph.D. thesis. Department of Electrical Engineering, Linköping University, Linköping, Sweden.
134. El Gamal H & Hammons AR (2001) Analyzing the turbo decoder using the Gaussian approximation. IEEE Transactions on Information Theory 47(2): 671–686.
135. Divsalar D, Dolinar S & Pollara F (2001) Iterative turbo decoder analysis based on density evolution. IEEE Journal on Selected Areas in Communications 19(5): 891–907.
136. Lee JW & Blahut RE (2007) Convergence analysis and BER performance of finite-length turbo codes. IEEE Transactions on Communications 55(5): 1033–1043.
137. Narayanan KR (2001) Effect of precoding on the convergence of turbo equalization for partial response channels. IEEE Journal on Selected Areas in Communications 19(4): 686–698.
138. ten Brink S (2001) Convergence behavior of iteratively decoded parallel concatenated codes. IEEE Transactions on Communications 49(10): 1727–1737.
139. Chung SY, Richardson TJ & Urbanke RL (2001) Analysis of sum-product decoding of low-density parity-check codes using a Gaussian approximation. IEEE Transactions on Information Theory 47(2): 657–670.
140. Hermosilla C & Szczeciński L (2003) EXIT charts for turbo receivers in MIMO systems. In: Proceedings of the International Symposium on Signal Processing and Its Applications, volume 1, pp. 209–212. Paris, France.
141. Li K & Wang X (2005) EXIT chart analysis of turbo multiuser detection. IEEE Transactions on Wireless Communications 4(1): 300–311.
142. Hermosilla C & Szczeciński L (2005) Performance evaluation of linear turbo receivers using analytical extrinsic information transfer functions. EURASIP Journal on Applied Signal Processing 2005(6): 892–905.

143. Visoz R, Berthet AO & Lalam M (2010) Semi-analytical performance prediction methods for iterative MMSE-IC multiuser MIMO joint decoding. IEEE Transactions on Communications 58(9): 2576–2589.
144. Hermosilla C & Szczeciński L (2006) Adaptive modulation and coding for turbo receivers in space-time BICM. In: Proceedings of the IEEE Wireless Communications and Networking Conference, volume 3, pp. 1293–1298. Las Vegas, NV, USA.
145. Ibi S, Matsumoto T, Thomä R, Sampei S & Morinaga N (2007) EXIT chart-aided adaptive coding for multilevel BICM with turbo equalization in frequency-selective MIMO channels. IEEE Transactions on Vehicular Technology 56(6): 3757–3769.
146. Ning B, Visoz R & Berthet AO (2011) Semi-analytical performance prediction method for iterative MMSE-IC detection and semi-blind channel estimation. In: Proceedings of the IEEE Vehicular Technology Conference, pp. 1–5. Yokohama, Japan.
147. Valenti MC & Cheng S (2005) Iterative demodulation and decoding of turbo-coded M-ary noncoherent orthogonal modulation. IEEE Journal on Selected Areas in Communications 23(9): 1739–1747.
148. Karjalainen J, Codreanu M, Tölli A, Juntti M & Matsumoto T (2011) EXIT chart-based power allocation for iterative frequency domain MIMO detector. IEEE Transactions on Signal Processing 59(4): 1624–1641.
149. Ylioinas J, Karjalainen J, Juntti M & Piirainen O (2013) Scheduling of the activations in iterative detection, decoding, and channel estimation for MIMO-OFDM. IEEE Transactions on Communications 61(2): 638–647.
150. Bhattad K & Naraynan KR (2007) An MSE-based transfer chart for analyzing iterative decoding schemes using a Gaussian approximation. IEEE Transactions on Information Theory 53(1): 22–38.
151. Ibing A & Boche H (2010) On predicting convergence of iterative MIMO detection-decoding with concatenated codes. IEEE Transactions on Vehicular Technology 59(8): 4134–4139.
152. Poor HV & Verdú S (1997) Probability of error in MMSE multiuser detection. IEEE Transactions on Information Theory 43(3): 858–871.
153. Zhang J, Chong EKP & Tse DNC (2001) Output MAI distributions of linear MMSE multiuser receivers in DS-CDMA systems. IEEE Transactions on Information Theory 47(3): 1128–1144.
154. Tse DNC & Zeitouni O (2000) Linear multiuser receivers in random environments. IEEE Transactions on Information Theory 46(1): 171–188.
155. Guo D, Verdú S & Rasmussen LK (2002) Asymptotic normality of linear multiuser receiver outputs. IEEE Transactions on Information Theory 48(12): 3080–3095.
156. Böhnke R & Kammeyer KD (2006) SINR analysis for V-BLAST with ordered MMSE-SIC detection. In: Proceedings of the International Wireless Communications and Mobile Computing Conference, pp. 623–628. Vancouver, BC, Canada.
157. Li P, Paul D, Narasimhan R & Cioffi J (2006) On the distribution of SINR for MMSE MIMO receiver and performance analysis. IEEE Transactions on Information Theory 52(1): 271–286.
158. Kammoun A, Kharouf M, Hachem W & Najim J (2009) BER and outage probability approximations for LMMSE detectors on correlated MIMO channels. IEEE Transactions on Information Theory 55(10): 4386–4397.
159. Hong L & Garcia Armada A (2011) Bit error rate performance of MIMO MMSE receivers in correlated Rayleigh flat-fading channels. IEEE Transactions on Vehicular Technology

60(1): 313–317.
160. Ma J, Zhang YJ, Su X & Yao Y (2008) On capacity of wireless ad hoc networks with MIMO MMSE receivers. IEEE Transactions on Wireless Communications 7(12): 5493–5503.
161. Kim N, Lee Y & Park H (2008) Performance analysis of MIMO system with linear MMSE receiver. IEEE Transactions on Wireless Communications 7(11): 4474–4478.
162. Kim W, Kim N, Chung HK & Lee H (2013) SINR distribution for MIMO MMSE receivers in transmit-correlated Rayleigh channels: SER performance and high-SNR power allocation. IEEE Transactions on Vehicular Technology 62(8): 4083–4087.
163. Liang YC, Pan G & Bai ZD (2007) Asymptotic performance of MMSE receivers for large systems using random matrix theory. IEEE Transactions on Information Theory 53(11): 4173–4190.
164. Kammoun A, Kharouf M, Hachem W & Najim J (2009) A central limit theorem for the SINR at the LMMSE estimator output for large-dimensional signals. IEEE Transactions on Information Theory 55(11): 5048–5063.
165. Kumar KR, Caire G & Moustakas AL (2009) Asymptotic performance of linear receivers in MIMO fading channels. IEEE Transactions on Information Theory 55(10): 4398–4418.
166. Jiang Y, Varanasi MK & Li J (2011) Performance analysis of ZF and MMSE equalizers for MIMO systems: An in-depth study of the high SNR regime. IEEE Transactions on Information Theory 57(4): 2008–2026.
167. Moustakas AL & Kazakopoulos P (2013) SINR statistics of correlated MIMO linear receivers. IEEE Transactions on Information Theory 59(10): 6490–6500.
168. Lin Z, Sørensen TB & Mogensen PE (2007) Downlink SINR distribution of linearly precoded multiuser MIMO systems. IEEE Communications Letters 11(11): 850–852.
169. Wang H, You X, Jiang B & Gao X (2008) Performance analysis of frequency domain equalization in SC-FDMA systems. In: Proceedings of the IEEE International Conference on Communications, pp. 4342–4347. Beijing, China.
170. Mielczarek B & Svensson A (2005) Modeling fading channel-estimation errors in pilot-symbol-assisted systems, with application to turbo codes. IEEE Transactions on Communications 53(11): 1822–1832.
171. Martinez A, Guillén i Fàbregas A & Caire G (2006) Error probability analysis of bit-interleaved coded modulation. IEEE Transactions on Information Theory 52(1): 262–271.
172. Martinez A, Guillén i Fàbregas A & Caire G (2007) A closed-form approximation for the error probability of BPSK fading channels. IEEE Transactions on Wireless Communications 6(6): 2051–2054.
173. Alvarado A, Szczecinski L, Feick R & Ahumada L (2009) Distribution of L-values in Gray-mapped M^2-QAM: Closed-form approximations and applications. IEEE Transactions on Communications 57(7): 2071–2079.
174. Hayes J (1968) Adaptive feedback communications. IEEE Transactions on Communications 16(1): 29–34.
175. Srinivasan R (1981) Feedback communications over fading channels. IEEE Transactions on Communications 29(1): 50–57.
176. Love DJ, Heath RW, Lau VKN, Gesbert D, Rao BD & Andrews M (2008) An overview of limited feedback in wireless communication systems. IEEE Journal on Selected Areas in Communications 26(8): 1341–1365.
177. Love DJ, Heath RW, Santipach W & Honig ML (2004) What is the value of limited feedback for MIMO channels? IEEE Communications Magazine 42(10): 54–59.

178. Catreux S, Erceg V, Gesbert D & Heath RW (2002) Adaptive modulation and MIMO coding for broadband wireless data networks. IEEE Communications Magazine 40(6): 108–115.
179. Falahati S, Svensson A, Ekman T & Sternad M (2004) Adaptive modulation systems for predicted wireless channels. IEEE Transactions on Communications 52(2): 307–316.
180. Paris JF, Aguayo-Torres MC & Entrambasaguas JT (2004) Impact of channel estimation error on adaptive modulation performance in flat fading. IEEE Transactions on Communications 52(5): 716–720.
181. Zhou S & Giannakis GB (2004) How accurate channel prediction needs to be for transmit-beamforming with adaptive modulation over Rayleigh MIMO channels? IEEE Transactions on Wireless Communications 3(4): 1285–1294.
182. Zhou S & Giannakis GB (2004) Adaptive modulation for multiantenna transmissions with channel mean feedback. IEEE Transactions on Wireless Communications 3(5): 1626–1636.
183. Xia P, Zhou S & Giannakis GB (2005) Multiantenna adaptive modulation with beamforming based on bandwidth-constrained feedback. IEEE Transactions on Communications 53(3): 526–536.
184. Paris JF & Goldsmith AJ (2006) Adaptive modulation for MIMO multiplexing under average BER constraints and imperfect CSI. In: Proceedings of the IEEE International Conference on Communications, volume 3, pp. 1318–1325. Istanbul, Turkey.
185. Ekpenyong AE & Huang YF (2006) Feedback-detection strategies for adaptive modulation systems. IEEE Transactions on Communications 54(10): 1735–1740.
186. Fernández-Plazaola U, Martos-Naya E, Paris JF & Goldsmith AJ (2010) Adaptive modulation for MIMO systems with channel prediction errors. IEEE Transactions on Wireless Communications 9(8): 2516–2527.
187. Kang JW, Jang M, Kim SH & Kim DI (2014) Outage analysis of multi-antenna rate adaptive systems with outdated feedback. IEEE Transactions on Wireless Communications 13(10): 5453–5466.
188. Nanda S & Rege KM (1998) Frame error rates for convolutional codes on fading channels and the concept of effective E_b/N_0. IEEE Transactions on Vehicular Technology 47(4): 1245–1250.
189. Brueninghaus K, Astély D, Sälzer T, Visuri S, Alexiou A, Karger S & Seraji GA (2005) Link performance models for system level simulations of broadband radio access systems. In: Proceedings of the IEEE International Symposium on Personal, Indoor, and Mobile Radio Communications, volume 4, pp. 2306–2311. Berlin, Germany.
190. Kim J, Lee KJ, Sung CK & Lee I (2009) A simple SNR representation method for AMC schemes of MIMO systems with ML detector. IEEE Transactions on Communications 57(10): 2971–2976.
191. Choi YS & Alamouti S (2008) A pragmatic PHY abstraction technique for link adaptation and MIMO switching. IEEE Journal on Selected Areas in Communications 26(6): 960–971.
192. Jensen TL, Kant S, Wehinger J & Fleury BH (2010) Fast link adaptation for MIMO-OFDM. IEEE Transactions on Vehicular Technology 59(8): 3766–3778.
193. Proakis JG (2001) Digital Communication. McGraw–Hill, New York, NY, USA, fourth edition.
194. Peng F, Zhang J & Ryan WE (2007) Adaptive modulation and coding for IEEE 802.11n. In: Proceedings of the IEEE Wireless Communications and Networking Conference, pp. 656–661. Kowloon, Hong Kong.

195. Tan P, Wu Y & Sun S (2008) Link adaptation based on adaptive modulation and coding for multiple-antenna OFDM system. IEEE Journal on Selected Areas in Communications 26(8): 1599–1606.
196. Cavers JK (1972) Variable-rate transmission for Rayleigh fading channels. IEEE Transactions on Communications 20(1): 15–22.
197. Goldsmith AJ & Chua SG (1997) Variable-rate variable-power MQAM for fading channels. IEEE Transactions on Communications 45(10): 1218–1230.
198. Ue T, Sampei S, Morinaga N & Hamaguchi K (1998) Symbol rate and modulation level-controlled adaptive modulation/TDMA/TDD system for high-bit-rate wireless data transmission. IEEE Transactions on Vehicular Technology 47(4): 1134–1147.
199. Alouini MS, Tang X & Goldsmith AJ (1999) An adaptive modulation scheme for simultaneous voice and data transmission over fading channels. IEEE Journal on Selected Areas in Communications 17(5): 837–850.
200. Qu X & Chawla K (1999) On the performance of adaptive modulation in cellular systems. IEEE Transactions on Communications 47(6): 884–895.
201. Alouini MS & Goldsmith AJ (2000) Adaptive modulation over Nakagami fading channels. Wireless Personal Communications, Kluwer Academic Publishers 13(1–2): 119–143.
202. Paris JF, Aguayo-Torres MC & Entrambasaguas JT (2001) Optimum discrete-power adaptive QAM scheme for Rayleigh fading channels. IEEE Communications Letters 5(7): 281–283.
203. Chung ST & Goldsmith AJ (2001) Degrees of freedom in adaptive modulation: A unified view. IEEE Transactions on Communications 49(9): 1561–1571.
204. Kim J, Kim I, Ro S, Hong D & Kang C (2002) Effects of multipath diversity on adaptive QAM in frequency selective rayleigh fading channels. IEEE Communications Letters 6(9): 364–366.
205. Zhou Z, Vucetic B, Dohler M & Li Y (2005) MIMO systems with adaptive modulation. IEEE Transactions on Vehicular Technology 54(5): 1828–1842.
206. Vucetic B (1991) An adaptive coding scheme for time-varying channels. IEEE Transactions on Communications 39(5): 653–663.
207. Örmeci P, Liu X, Goeckel DL & Wesel RD (2001) Adaptive bit-interleaved coded modulation. IEEE Transactions on Communications 49(9): 1572–1581.
208. Liu Q, Zhou S & Giannakis GB (2004) Cross-layer combining of adaptive modulation and coding with truncated ARQ over wireless links. IEEE Transactions on Wireless Communications 3(5): 1746–1755.
209. Song KB, Ekbal A, Chung ST & Cioffi JM (2006) Adaptive modulation and coding (AMC) for bit-interleaved coded OFDM (BIC-OFDM). IEEE Transactions on Wireless Communications 5(7): 1685–1694.
210. Simoens S, Rouquette-Léveil S, Sartori P, Blankenship Y & Classon B (2006) Error prediction for adaptive modulation and coding in multiple-antenna OFDM systems. Signal Processing, Elsevier Publishing Company 86(8): 1911–1916.
211. Sung CK, Chung SY, Heo J & Lee I (2007) Adaptive bit-interleaved coded OFDM with reduced feedback information. IEEE Transactions on Communications 55(9): 1649–1655.
212. Ahrens A, Ng SX, Kühn V & Hanzo L (2008) Modulation-mode assignment for SVD-aided and BICM-assisted spatial division multiplexing. Physical Communication, Elsevier Publishing Company 1(1): 60–66.
213. Ahrens A & Benavente-Peces C (2009) Modulation-mode and power assignment for broadband MIMO-BICM schemes. In: Proceedings of the IEEE International Symposium

on Personal, Indoor, and Mobile Radio Communications, pp. 236–240. Tokyo, Japan.
214. Daniels RC, Caramanis CM & Heath RW (2010) Adaptation in convolutionally coded MIMO-OFDM wireless systems through supervised learning and SNR ordering. IEEE Transactions on Vehicular Technology 59(1): 114–126.
215. Lagrange X (2010) Throughput of HARQ protocols on a block fading channel. IEEE Communications Letters 14(3): 257–259.
216. Eraslan E, Wang CY & Daneshrad B (2014) Practical energy-aware link adaptation for MIMO-OFDM systems. IEEE Transactions on Wireless Communications 13(1): 246–258.
217. Alamouti SM & Kallel S (1994) Adaptive trellis-coded multiple-phase-shift keying for Rayleigh fading channels. IEEE Transactions on Communications 42(6): 2305–2314.
218. Goldsmith AJ & Chua SG (1998) Adaptive coded modulation for fading channels. IEEE Transactions on Communications 46(5): 595–602.
219. Goeckel DL (1999) Adaptive coding for time-varying channels using outdated fading estimates. IEEE Transactions on Communications 47(6): 844–855.
220. Hole KJ, Holm H & Øien GE (2000) Adaptive multidimensional coded modulation over flat fading channels. IEEE Journal on Selected Areas in Communications 18(7): 1153–1158.
221. Lau VKN & Macleod MD (2001) Variable-rate adaptive trellis coded QAM for flat-fading channels. IEEE Transactions on Communications 49(9): 1550–1560.
222. Øien GE, Holm H & Hole KJ (2004) Impact of channel prediction on adaptive coded modulation performance in Rayleigh fading. IEEE Transactions on Vehicular Technology 53(3): 758–769.
223. Blankenship YW, Sartori PJ, Classon BK, Desai V & Baum KL (2004) Link error prediction methods for multicarrier systems. In: Proceedings of the IEEE Vehicular Technology Conference, volume 6, pp. 4175–4179. Los Angeles, CA, USA.
224. Stiglmayr S, Bossert M & Costa E (2007) Adaptive coding and modulation in OFDM systems using BICM and rate-compatible punctured codes. In: Proceedings of the European Wireless Conference. Paris, France.
225. Kim SL, Rosberg Z & Zander J (1999) Combined power control and transmission rate selection in cellular networks. In: Proceedings of the IEEE Vehicular Technology Conference, volume 3, pp. 1653–1657. Amsterdam, The Netherlands.
226. Köse C & Goeckel DL (2000) On power adaptation in adaptive signaling systems. IEEE Transactions on Communications 48(11): 1769–1773.
227. Chung ST, Lozano A, Huang HC, Sutivong A & Cioffi JM (2004) Approaching the MIMO capacity with a low-rate feedback channel in V-BLAST. EURASIP Journal on Applied Signal Processing 2004(5): 762–771.
228. Kim TT & Skoglund M (2007) Diversity–multiplexing tradeoff in MIMO channels with partial CSIT. IEEE Transactions on Information Theory 53(8): 2743–2759.
229. Khaled N, Thoen S & Deneire L (2005) Optimizing the joint transmit and receive MMSE design using mode selection. IEEE Transactions on Communications 53(4): 730–737.
230. Heath RW & Paulraj AJ (2005) Switching between diversity and multiplexing in MIMO systems. IEEE Transactions on Communications 53(6): 962–968.
231. Chae CB, Forenza A, Heath RW, McKay MR & Collings IB (2010) Adaptive MIMO transmission techniques for broadband communication systems. IEEE Communications Magazine 48(5): 112–118.
232. Forenza A, McKay MR, Pandharipande A, Heath RW & Collings IB (2007) Adaptive MIMO transmission for exploiting the capacity of spatially correlated channels. IEEE

Transactions on Vehicular Technology 56(2): 619–630.
233. Zhang J, Heath RW, Kountouris M & Andrews JG (2009) Mode switching for the multi-antenna broadcast channel based on delay and channel quantization. EURASIP Journal on Applied Signal Processing 2009(1): 1–15.
234. Haleem MA & Chandramouli R (2005) Adaptive downlink scheduling and rate selection: A cross-layer design. IEEE Journal on Selected Areas in Communications 23(6): 1287–1297.
235. Rico-Alvariño A & Heath RW (2014) Learning-based adaptive transmission for limited feedback multiuser MIMO-OFDM. IEEE Transactions on Wireless Communications 13(7): 3806–3820.
236. Cui S, Goldsmith AJ & Bahai A (2005) Energy-constrained modulation optimization. IEEE Transactions on Wireless Communications 4(5): 2349–2360.
237. Miao G, Himayat N & Li GY (2010) Energy-efficient link adaptation in frequency-selective channels. IEEE Transactions on Communications 58(2): 545–554.
238. ten Brink S & Kramer G (2003) Design of repeat–accumulate codes for iterative detection and decoding. IEEE Transactions on Signal Processing 51(11): 2764–2772.
239. Tüchler M (2004) Design of serially concatenated systems depending on the block length. IEEE Transactions on Communications 52(2): 209–218.
240. ten Brink S, Kramer G & Ashikhmin A (2004) Design of low-density parity-check codes for modulation and detection. IEEE Transactions on Communications 52(4): 670–678.
241. Ashikhmin A, Kramer G & ten Brink S (2004) Extrinsic information transfer functions: Model and erasure channel properties. IEEE Transactions on Information Theory 50(11): 2657–2673.
242. Wohlgenannt R, Kansanen K, Tujkovic D & Matsumoto T (2005) Outage-based LDPC code design for SC/MMSE turbo-equalization. In: Proceedings of the IEEE Vehicular Technology Conference, volume 1, pp. 505–509. Stockholm, Sweden.
243. Yue G & Wang X (2005) Optimization of irregular repeat accumulate codes for MIMO systems with iterative receivers. IEEE Transactions on Wireless Communications 4(6): 2843–2855.
244. Jiang M, Prasad N, Yue G & Rangarajan S (2011) Efficient link adaptation for precoded multi-rank transmission and turbo SIC receivers. In: Proceedings of the IEEE International Conference on Communications, pp. 1–5. Kyoto, Japan.
245. Xue Y, Sun Q, Jiang B & Gao X (2014) Link adaptation scheme for uplink MIMO transmission with turbo receivers. In: Proceedings of the IEEE Vehicular Technology Conference, pp. 1–5. Seoul, Republic of Korea.
246. Rocher EY & Pickholtz RL (1970) An analysis of the effectiveness of hybrid transmission schemes. IBM Journal of Research and Development 14(4): 426–433.
247. Burton HO & Sullivan DD (1972) Errors and error control. Proceedings of the IEEE 60(11): 1293–1301.
248. Wu P & Jindal N (2010) Performance of hybrid-ARQ in block-fading channels: A fixed outage probability analysis. IEEE Transactions on Communications 58(4): 1129–1141.
249. El Gamal H, Caire G & Damen MO (2006) The MIMO ARQ channel: Diversity–multiplexing–delay tradeoff. IEEE Transactions on Information Theory 52(8): 3601–3621.
250. Holliday T, Goldsmith A & Poor HV (2006) The impact of delay on the diversity, multiplexing, and ARQ tradeoff. In: Proceedings of the IEEE International Conference on Communications, volume 4, pp. 1445–1449. Istanbul, Turkey.

251. Chuang A, Guillén i Fàbregas A, Rasmussen LK & Collings IB (2008) Optimal throughput–diversity–delay tradeoff in MIMO ARQ block-fading channels. IEEE Transactions on Information Theory 54(9): 3968–3986.
252. Caire G & Tuninetti D (2001) The throughput of hybrid-ARQ protocols for the Gaussian collision channel. IEEE Transactions on Information Theory 47(5): 1971–1988.
253. Leung CHC, Kikumoto Y & Sorensen SA (1988) The throughput efficiency of the go-back-N ARQ scheme under Markov and related error structures. IEEE Transactions on Communications 36(2): 231–234.
254. Lu DL & Chang JF (1993) Performance of ARQ protocols in nonindependent channel errors. IEEE Transactions on Communications 41(5): 721–730.
255. Cho YJ & Un CK (1994) Performance analysis of ARQ error controls under Markovian block error pattern. IEEE Transactions on Communications 42(2/3/4): 2051–2061.
256. Zorzi M, Rao RR & Milstein LB (1997) ARQ error control for fading mobile radio channels. IEEE Transactions on Vehicular Technology 46(2): 445–455.
257. Turin W (1999) Throughput analysis of the go-back-N protocol in fading radio channels. IEEE Journal on Selected Areas in Communications 17(5): 881–887.
258. Femenias G (2005) SR ARQ for adaptive modulation systems combined with selection transmit diversity. IEEE Transactions on Communications 53(6): 998–1006.
259. Ausavapattanakun K & Nosratinia A (2007) Analysis of selective-repeat ARQ via matrix signal-flow graphs. IEEE Transactions on Communications 55(1): 198–204.
260. Ausavapattanakun K & Nosratinia A (2007) Analysis of go-back-N ARQ in block fading channels. IEEE Transactions on Wireless Communications 6(8): 2793–2797.
261. Tuninetti D (2011) On the benefit of partial channel state information for repetition protocols in block fading channels. IEEE Transactions on Information Theory 57(8): 5036–5053.
262. Wu J, Wang G & Zheng YR (2014) Energy efficiency and spectral efficiency tradeoff in type-I ARQ systems. IEEE Journal on Selected Areas in Communications 32(2): 356–366.
263. Balachandran K & Anderson JB (1998) Mismatched decoding of intersymbol interference using a parallel concatenated scheme. IEEE Journal on Selected Areas in Communications 16(2): 255–259.
264. Doan DN & Narayanan KR (2002) Iterative packet combining schemes for intersymbol interference channels. IEEE Transactions on Communications 50(4): 560–570.
265. Samra H & Ding Z (2005) A hybrid ARQ protocol using integrated channel equalization. IEEE Transactions on Communications 53(12): 1996–2001.
266. Ait-Idr T & Saoudi S (2009) Turbo packet combining strategies for the MIMO-ISI ARQ channel. IEEE Transactions on Communications 57(12): 3782–3793.
267. Roongta A, Moon JW & Shea JM (2005) Reliability-based hybrid ARQ as an adaptive response to jamming. IEEE Journal on Selected Areas in Communications 23(5): 1045–1055.
268. Zhou Y & Wang J (2006) Optimum subpacket transmission for hybrid-ARQ systems. IEEE Transactions on Communications 54(5): 934–942.
269. Frenger P, Parkvall S & Dahlman E (2001) Performance comparison of HARQ with Chase combining and incremental redundancy for HSDPA. In: Proceedings of the IEEE Vehicular Technology Conference, volume 3, pp. 1829–1833. Atlantic City, NJ, USA.
270. Cheng JF (2006) Coding performance of hybrid ARQ schemes. IEEE Transactions on Communications 54(6): 1017–1029.

271. Hagenauer J (1988) Rate-compatible punctured convolutional codes (RCPC codes) and their applications. IEEE Transactions on Communications 36(4): 389–400.
272. Rowitch DN & Milstein LB (2000) On the performance of hybrid FEC/ARQ systems using rate compatible punctured turbo (RCPT) codes. IEEE Transactions on Communications 48(6): 948–959.
273. Kallel S (1995) Complementary punctured convolutional (CPC) codes and their applications. IEEE Transactions on Communications 43(6): 2005–2009.
274. Malkamäki E & Leib H (2000) Performance of truncated type-II hybrid ARQ schemes with noisy feedback over block fading channels. IEEE Transactions on Communications 48(9): 1477–1487.
275. Narayanan KR & Stüber GL (1997) A novel ARQ technique using the turbo coding principle. IEEE Communications Letters 1(2): 49–51.
276. Souza RD, Pellenz ME & Rodrigues T (2009) Hybrid ARQ scheme based on recursive convolutional codes and turbo decoding. IEEE Transactions on Communications 57(2): 315–318.
277. Uhlemann E, Rasmussen LK, Grant A & Wiberg PA (2003) Optimal incremental-redundancy strategy for type-II hybrid ARQ. In: Proceedings of the IEEE International Symposium on Information Theory, pp. 448–448. Yokohama, Japan.
278. Shen C, Liu T & Fitz MP (2009) On the average rate performance of hybrid-ARQ in quasi-static fading channels. IEEE Transactions on Communications 57(11): 3339–3352.
279. Makki B & Eriksson T (2012) On hybrid ARQ and quantized CSI feedback schemes in quasi-static fading channels. IEEE Transactions on Communications 60(4): 986–997.
280. Szczecinski L, Khosravirad SR, Duhamel P & Rahman M (2013) Rate allocation and adaptation for incremental redundancy truncated HARQ. IEEE Transactions on Communications 61(6): 2580–2590.
281. Pfletschinger S, Declercq D & Navarro M (2014) Adaptive HARQ with non-binary repetition coding. IEEE Transactions on Wireless Communications 13(8): 4193–4204.
282. Visotsky E, Sun Y, Tripathi V, Honig ML & Peterson R (2005) Reliability-based incremental redundancy with convolutional codes. IEEE Transactions on Communications 53(6): 987–997.
283. Hwang SH, Kim B & Kim YS (2001) A hybrid ARQ scheme with power ramping. In: Proceedings of the IEEE Vehicular Technology Conference, volume 3, pp. 1579–1583. Atlantic City, NJ, USA.
284. Su W, Lee S, Pados DA & Matyjas JD (2011) Optimal power assignment for minimizing the average total transmission power in hybrid-ARQ Rayleigh fading links. IEEE Transactions on Communications 59(7): 1867–1877.
285. Makki B, Graell i Amat A & Eriksson T (2012) Power allocation in repetition time diversity hybrid automatic repeat request feedback. In: Proceedings of the IEEE Wireless Communications and Networking Conference, pp. 2329–2334. Shanghai, China.
286. Liu H, Razoumov L, Mandayam N & Spasojević P (2009) An optimal power allocation scheme for the STC hybrid–ARQ over energy limited networks. IEEE Transactions on Wireless Communications 8(12): 5718–5722.
287. Chaitanya TVK & Larsson EG (2011) Outage-optimal power allocation for hybrid ARQ with incremental redundancy. IEEE Transactions on Wireless Communications 10(7): 2069–2074.

288. Nguyen KD, Rasmussen LK, Guillén i Fàbregas A & Letzepis N (2012) MIMO ARQ with multibit feedback: Outage analysis. IEEE Transactions on Information Theory 58(2): 765–779.
289. Ji C, Wang D, Liu N & You X (2015) On power allocation for incremental redundancy hybrid ARQ. IEEE Transactions on Wireless Communications 14(3): 1506–1518.
290. Zheng H & Viswanathan H (2005) Optimizing the ARQ performance in downlink packet data systems with scheduling. IEEE Transactions on Wireless Communications 4(2): 495–506.
291. Kim D, Jung BC, Lee H, Sung DK & Yoon H (2008) Optimal modulation and coding scheme selection in cellular networks with hybrid-ARQ error control. IEEE Transactions on Wireless Communications 7(12): 5195–5201.
292. Kim SM, Choi W, Ban TW & Sung DK (2011) Optimal rate adaptation for hybrid ARQ in time-correlated Rayleigh fading channels. IEEE Transactions on Wireless Communications 10(3): 968–979.
293. Kallel S, Bakhtiyari S & Link R (2000) An adaptive hybrid ARQ scheme. Wireless Personal Communications, Kluwer Academic Publishers 12(3): 297–311.
294. Kermoal JP, Schumacher L, Pedersen KI, Mogensen PE & Frederiksen F (2002) A stochastic MIMO radio channel model with experimental validation. IEEE Journal on Selected Areas in Communications 20(6): 1211–1226.
295. Oestges C, Özcelik H & Bonek E (2005) On the practical use of analytical MIMO channel models. In: Proceedings of the IEEE Antennas and Propagation Society International Symposium, volume 3B, pp. 406–409. Washington, DC, USA.
296. Oestges C, Clerckx B, Vanhoenacker-Janvier D & Paulraj AJ (2005) Impact of fading correlations on MIMO communication systems in geometry-based statistical channel models. IEEE Transactions on Wireless Communications 4(3): 1112–1120.
297. Oestges C (2006) Validity of the Kronecker model for MIMO correlated channels. In: Proceedings of the IEEE Vehicular Technology Conference, pp. 2818–2822. Melbourne, Vic., Australia.
298. Kansanen K (2005) Wireless Broadband Single-Carrier Systems with MMSE Turbo Equalization Receivers. Number C230 in Acta Universitatis Ouluensis, D.Sc. (Tech.) thesis. University of Oulu, Oulu, Finland.
299. Karjalainen J (2011) Broadband Single Carrier Multi-Antenna Communications with Frequency Domain Turbo Equalization. Number C387 in Acta Universitatis Ouluensis, D.Sc. (Tech.) thesis. University of Oulu, Oulu, Finland.
300. Brännström F, Rasmussen LK & Grant AJ (2005) Convergence analysis and optimal scheduling for multiple concatenated codes. IEEE Transactions on Information Theory 51(9): 3354–3364.
301. Witzke M, Bäro S, Schreckenbach F & Hagenauer J (2002) Iterative detection of MIMO signals with linear detectors. In: Proceedings of the Annual Asilomar Conference on Signals, Systems and Computers, volume 1, pp. 289–293. Pacific Grove, CA, USA.
302. Sun S, Wu Y, Li Y & Thjung TT (2008) A Bayesian MMSE turbo receiver for coded MIMO systems. IEEE Transactions on Vehicular Technology 57(5): 3283–3293.
303. Senst M & Ascheid G (2011) How the framework of expectation propagation yields an iterative IC-LMMSE MIMO receiver. In: Proceedings of the IEEE Global Telecommunication Conference, pp. 1–6. Houston, TX, USA.

304. Mood AM, Graybill FA & Boes DC (1974) Introduction to the Theory of Statistics. McGraw–Hill, New York, NY, USA, third edition.
305. Brillinger DR (1974) Fourier analysis of stationary processes. Proceedings of the IEEE 62(12): 1628–1643.
306. Nakagami M (1960) The *m*-distribution—a general formula of intensity distribution of rapid fading. In: Hoffman WC (ed.) Statistical Methods in Radio Wave Propagation, pp. 3–36. Pergamon Press, Oxford, UK.
307. Suzuki H (1977) A statistical model for urban radio propagation. IEEE Transactions on Communications 25(7): 673–680.
308. Land I, Hoeher PA & Gligorević S (2004) Computation of symbol-wise mutual information in transmission systems with LogAPP decoders and application to EXIT charts. In: Proceedings of the International ITG Conference on Source and Channel Coding, pp. 195–202. Erlangen, Germany.
309. Caire G & Shamai S (1999) On the capacity of some channels with channel state information. IEEE Transactions on Information Theory 45(6): 2007–2019.
310. Wu P & Jindal N (2011) Coding versus ARQ in fading channels: How reliable should the PHY be? IEEE Transactions on Communications 59(12): 3363–3374.
311. Zheng H, Lozano A & Haleem M (2004) Multiple ARQ processes for MIMO systems. EURASIP Journal on Applied Signal Processing 2004(5): 772–782.
312. Matzner R & Letsch K (1994) SNR estimation and blind equalization (deconvolution) using the kurtosis. In: Proceedings of the IEEE-IMS Workshop on Information Theory and Statistics, pp. 68–68. Alexandria, VA, USA.
313. Aldana CH, Salvekar AA, Tellado J & Cioffi J (2000) Accurate noise estimates in multicarrier systems. In: Proceedings of the IEEE Vehicular Technology Conference, volume 1, pp. 434–438. Boston, MA, USA.
314. Husson L, Wautier A, Antoine J & Dany JC (2001) Estimation of noise and interfering power for transmissions over Rayleigh fading channels. In: Proceedings of the IEEE Vehicular Technology Conference, volume 3, pp. 1548–1552. Rhodes, Greece.
315. Boumard S (2003) Novel noise variance and SNR estimation algorithm for wireless MIMO OFDM systems. In: Proceedings of the IEEE Global Telecommunication Conference, volume 3, pp. 1330–1334. San Francisco, CA, USA.
316. Cui T & Tellambura C (2006) Power delay profile and noise variance estimation for OFDM. IEEE Communications Letters 10(1): 25–27.
317. Coon J, Sandell M, Beach M & McGeehan J (2006) Channel and noise variance estimation and tracking algorithms for unique-word based single-carrier systems. IEEE Transactions on Wireless Communications 5(6): 1488–1496.
318. Moustakas AL & Simon SH (2007) On the outage capacity of correlated multi-path MIMO channels. IEEE Transactions on Information Theory 53(11): 3887–3903.
319. Lampe M, Giebel T, Rohling H & Zirwas W (2003) PER-prediction for PHY mode selection in OFDM communication systems. In: Proceedings of the IEEE Global Telecommunication Conference, volume 1, pp. 25–29. San Francisco, CA, USA.
320. Papoulis A & Pillai SU (2002) Probability, Random Variables and Stochastic Processes. McGraw–Hill, New York, NY, USA, fourth edition.
321. Tulino AM & Verdú S (2004) Random Matrix Theory and Wireless Communications. Now Publishers Inc.

Appendix 1 PDF of the effective SINR for flat fading SISO and uncorrelated SIMO channels

When the distribution of θ is known, the distribution of $\hat{\beta}_k$ can be derived (see [320, Sect. 5-2]). Expressing θ with respect to $\hat{\beta}_k$,

$$\theta = \frac{\hat{\beta}_k \sigma_\eta^2}{1 - \hat{\Delta}_\mathrm{a} \hat{\beta}_k}. \tag{51}$$

The PDF of $\hat{\beta}_k$,

$$f_{\hat{\beta}_k}\left(\hat{\beta}_k\right) = \left(\left|\frac{\partial \hat{\beta}_k}{\partial \theta}\right|\right)^{-1} f_\theta(\theta) \tag{52}$$

$$= \left(\left|\frac{\sigma_\eta^2}{\left(\hat{\Delta}_\mathrm{a}\theta + \sigma_\eta^2\right)^2}\right|\right)^{-1} \frac{\theta^{N_\mathrm{R}-1}}{(N_\mathrm{R}-1)!} \exp(-\theta) \tag{53}$$

$$= \frac{\left(\hat{\Delta}_\mathrm{a} \frac{\hat{\beta}_k \sigma_\eta^2}{1-\hat{\Delta}_\mathrm{a}\hat{\beta}_k} + \sigma_\eta^2\right)^2}{\sigma_\eta^2} \frac{\left(\frac{\hat{\beta}_k \sigma_\eta^2}{1-\hat{\Delta}_\mathrm{a}\hat{\beta}_k}\right)^{N_\mathrm{R}-1}}{(N_\mathrm{R}-1)!} \exp\left(-\frac{\hat{\beta}_k \sigma_\eta^2}{1 - \hat{\Delta}_\mathrm{a}\hat{\beta}_k}\right) \tag{54}$$

$$= \frac{\sigma_\eta^2}{(1 - \hat{\Delta}_\mathrm{a}\hat{\beta}_k)^2} \frac{\left(\frac{\hat{\beta}_k \sigma_\eta^2}{1-\hat{\Delta}_\mathrm{a}\hat{\beta}_k}\right)^{N_\mathrm{R}-1}}{(N_\mathrm{R}-1)!} \exp\left(-\frac{\hat{\beta}_k \sigma_\eta^2}{1 - \hat{\Delta}_\mathrm{a}\hat{\beta}_k}\right). \tag{55}$$

Appendix 2 Reformulation of the effective SINR

The following lemma proves to be useful:

Lemma: Let $\boldsymbol{\alpha} \in \mathbb{C}^{N\times 1}$ $\boldsymbol{\Xi} \in \mathbb{C}^{N\times N}$ be an invertible matrix and $\tau \in \mathbb{R}$. Then,

$$\boldsymbol{\alpha}^{\mathrm{H}}\left(\boldsymbol{\Xi}+\tau\boldsymbol{\alpha}\boldsymbol{\alpha}^{\mathrm{H}}\right)^{-1} = \left(1+\tau\boldsymbol{\alpha}^{\mathrm{H}}\boldsymbol{\Xi}^{-1}\boldsymbol{\alpha}\right)^{-1}\boldsymbol{\alpha}^{\mathrm{H}}\boldsymbol{\Xi}^{-1}.$$

Proof:

$$\boldsymbol{\alpha}^{\mathrm{H}}\boldsymbol{\Xi}^{-1}\left(\boldsymbol{\Xi}+\tau\boldsymbol{\alpha}\boldsymbol{\alpha}^{\mathrm{H}}\right) = \boldsymbol{\alpha}^{\mathrm{H}}+\tau\boldsymbol{\alpha}^{\mathrm{H}}\left(\boldsymbol{\Xi}\right)^{-1}\boldsymbol{\alpha}\boldsymbol{\alpha}^{\mathrm{H}} = \left(1+\tau\boldsymbol{\alpha}^{\mathrm{H}}\boldsymbol{\Xi}^{-1}\boldsymbol{\alpha}\right)\boldsymbol{\alpha}^{\mathrm{H}}.$$

□

Before proceeding further, (25) is rewritten for convenience,

$$\hat{\beta}'_{j,k} = \hat{\Delta}_{\mathrm{a},j}P_j\boldsymbol{\psi}_{k,j}^{\mathrm{H}}\boldsymbol{R}^{\frac{\mathrm{T}}{2}}\left(\sigma_\eta^2\boldsymbol{I}_{N_{\mathrm{R}}}+\boldsymbol{R}^{\frac{1}{2}}\boldsymbol{\Psi}_{-j,k}\hat{\boldsymbol{\Delta}}_{\mathrm{a},-j}\boldsymbol{P}_{-j}\boldsymbol{\Psi}_{-j,k}^{\mathrm{H}}\boldsymbol{R}^{\frac{\mathrm{T}}{2}}\right)^{-1}\boldsymbol{R}^{\frac{1}{2}}\boldsymbol{\psi}_{k,j}.$$

Starting from (23),

$$\begin{aligned}\hat{\beta}_{j,k} =& P_j\boldsymbol{\psi}_{k,j}^{\mathrm{H}}\boldsymbol{R}^{\frac{\mathrm{T}}{2}}\left(\sigma_\eta^2\boldsymbol{I}_{N_{\mathrm{R}}}+\boldsymbol{R}^{\frac{1}{2}}\boldsymbol{\Psi}_k\hat{\boldsymbol{\Delta}}_{\mathrm{a}}\boldsymbol{P}\boldsymbol{\Psi}_k^{\mathrm{H}}\boldsymbol{R}^{\frac{\mathrm{T}}{2}}\right)^{-1}\boldsymbol{R}^{\frac{1}{2}}\boldsymbol{\psi}_{k,j}\\ =& P_j\boldsymbol{\psi}_{k,j}^{\mathrm{H}}\boldsymbol{R}^{\frac{\mathrm{T}}{2}}\left(\sigma_\eta^2\boldsymbol{I}_{N_{\mathrm{R}}}+\boldsymbol{R}^{\frac{1}{2}}\boldsymbol{\Psi}_{-j,k}\hat{\boldsymbol{\Delta}}_{\mathrm{a},-j}\boldsymbol{P}_{-j}\boldsymbol{\Psi}_{-j,k}^{\mathrm{H}}\boldsymbol{R}^{\frac{\mathrm{T}}{2}}+\boldsymbol{R}^{\frac{1}{2}}\boldsymbol{\psi}_{k,j}\hat{\Delta}_{\mathrm{a},j}P_j\boldsymbol{\psi}_{k,j}^{\mathrm{H}}\boldsymbol{R}^{\frac{\mathrm{T}}{2}}\right)\boldsymbol{R}^{\frac{1}{2}}\boldsymbol{\psi}_{k,j}.\end{aligned} \tag{56}$$

By defining $\boldsymbol{\alpha} \equiv \boldsymbol{R}^{\frac{1}{2}}\boldsymbol{\psi}_{k,j} \in \mathbb{C}^{N_{\mathrm{R}}\times 1}$, $\boldsymbol{\Xi} \equiv \sigma_\eta^2\boldsymbol{I}_{N_{\mathrm{R}}}+\boldsymbol{R}^{\frac{1}{2}}\boldsymbol{\Psi}_{-j,k}\hat{\boldsymbol{\Delta}}_{\mathrm{a},-j}\boldsymbol{P}_{-j}\boldsymbol{\Psi}_{-j,k}^{\mathrm{H}}\boldsymbol{R}^{\frac{\mathrm{T}}{2}} \in \mathbb{C}^{N_{\mathrm{R}}\times N_{\mathrm{R}}}$ and $\tau = \hat{\Delta}_{\mathrm{a},j}P_j$, and utilising the Lemma above, (56) can be rewritten as

$$\begin{aligned}\hat{\beta}_{j,k} =& P_j\left(1+\hat{\Delta}_{\mathrm{a},j}P_j\boldsymbol{\psi}_{k,j}^{\mathrm{H}}\boldsymbol{R}^{\frac{\mathrm{T}}{2}}\left(\sigma_\eta^2\boldsymbol{I}_{N_{\mathrm{R}}}+\boldsymbol{R}^{\frac{1}{2}}\boldsymbol{\Psi}_{-j,k}\hat{\boldsymbol{\Delta}}_{\mathrm{a},-j}\boldsymbol{P}_{-j}\boldsymbol{\Psi}_{-j,k}^{\mathrm{H}}\boldsymbol{R}^{\frac{\mathrm{T}}{2}}\right)^{-1}\boldsymbol{R}^{\frac{1}{2}}\boldsymbol{\psi}_{k,j}\right)^{-1}\\ &\cdot\boldsymbol{\psi}_{k,j}^{\mathrm{H}}\boldsymbol{R}^{\frac{\mathrm{T}}{2}}\left(\sigma_\eta^2\boldsymbol{I}_{N_{\mathrm{R}}}+\boldsymbol{R}^{\frac{1}{2}}\boldsymbol{\Psi}_{-j,k}\hat{\boldsymbol{\Delta}}_{\mathrm{a},-j}\boldsymbol{P}_{-j}\boldsymbol{\Psi}_{-j,k}^{\mathrm{H}}\boldsymbol{R}^{\frac{\mathrm{T}}{2}}\right)\boldsymbol{R}^{\frac{1}{2}}\boldsymbol{\psi}_{k,j} \qquad (57)\\ =& P_j\left(1+\hat{\beta}'_{j,k}\right)^{-1}\left(\hat{\Delta}_{\mathrm{a},j}P_j\right)^{-1}\hat{\beta}'_{j,k} \qquad (58)\\ =& \hat{\Delta}_{\mathrm{a},j}^{-1}\hat{\beta}'_{j,k}\left(1+\hat{\beta}'_{j,k}\right)^{-1} \qquad (59)\\ =& \hat{\Delta}_{\mathrm{a},j}^{-1}\left(1-\left(1+\hat{\beta}'_{j,k}\right)^{-1}\right).\end{aligned}$$

□

Appendix 3 PDF of the effective SINR for RX correlated flat fading MIMO channels

The PDF of $\hat{\beta}'_{j,k}$ [167],

$$f_{\hat{\beta}'_{j,k}}\left(\hat{\beta}'_{j,k}\right) = \frac{1}{\sqrt{2\pi}} \exp\left(s_0\hat{\beta}'_{j,k} - I_{\text{erg}}(s_0) + I_{\text{erg}}(0) + \frac{v_1(s_0) + v_2(s_0)}{2}\right). \tag{60}$$

The terms within (26) and (60) are derived from [167], and are thereby largely the same. The differences arise from different scaling and the presence of $\hat{\Delta}_{\text{a},j}$, $j = 1, \ldots, N_{\text{T}}$. Let $\check{P}_j = \hat{\Delta}_{\text{a},j} P_j N_{\text{R}}/\sigma_\eta^2$,

$$I_{\text{erg}}(s) = \sum_{i=1}^{N_{\text{R}}} \ln\left[1 + \frac{\lambda_i^{\boldsymbol{R}}}{N_{\text{R}}}\left(s\check{P}_j + r(s)\right)\right] + \sum_{\substack{j'=1 \\ j'\neq j}}^{N_{\text{T}}} \ln\left[1 + \check{P}_{j'} t(s)\right] - r(s)\,t(s), \tag{61}$$

$$r(s) = \sum_{\substack{j'=1 \\ j'\neq j}}^{N_{\text{T}}} \frac{\check{P}_{j'}}{1 + \check{P}_{j'} t(s)}, \tag{62}$$

$$t(s) = \sum_{i=1}^{N_{\text{R}}} \frac{\frac{\lambda_i^{\boldsymbol{R}}}{N_{\text{R}}}}{1 + \frac{\lambda_i^{\boldsymbol{R}}}{N_{\text{R}}}\left(s\check{P}_j + r(s)\right)}, \tag{63}$$

where $\lambda_i^{\boldsymbol{R}}$, $i = 1, \ldots, N_{\text{R}}$, denote $\boldsymbol{R}$'s eigenvalues, and s_0 is a saddle point value, which is defined such that

$$t(s_0) = \check{P}_j^{-1}\hat{\beta}'_{j,k} \tag{64}$$

$$= \check{P}_j^{-1}\left(\frac{1}{1 - \hat{\Delta}_{\text{a},j}\hat{\beta}_{j,k}} - 1\right). \tag{65}$$

The remaining two terms,

$$v_1(s_0) = -\ln\left|1 - M_{r,s_0}M_{t,s_0}\right| - \ln\left|1 - M_{r,0}M_{t,0}\right| + 2\ln\left|1 - M_{r,\text{cov}}M_{t,\text{cov}}\right| \tag{66a}$$

$$v_2(s_0) = -\ln\left|\frac{\check{P}_j^2 M_{r,s_0}}{1 - M_{r,s_0}M_{t,s_0}}\right|, \tag{66b}$$

where

$$M_{r,0} = \sum_{i=1}^{N_\mathrm{R}} \left(\frac{\frac{\lambda_i^{\boldsymbol{R}}}{N_\mathrm{R}}}{1 + \frac{\lambda_i^{\boldsymbol{R}}}{N_\mathrm{R}} r(0)} \right)^2, \tag{67a}$$

$$M_{t,0} = \sum_{\substack{n=1 \\ j' \neq j}}^{N_\mathrm{T}} \left(\frac{\check{P}_{j'}}{1 + \check{P}_{j'} t(0)} \right)^2, \tag{67b}$$

$$M_{r,s_0} = \sum_{i=1}^{N_\mathrm{R}} \left(\frac{\frac{\lambda_i^{\boldsymbol{R}}}{N_\mathrm{R}}}{1 + \frac{\lambda_i^{\boldsymbol{R}}}{N_\mathrm{R}} \left(s_0 \check{P}_j + r(s_0) \right)} \right)^2, \tag{67c}$$

$$M_{t,s_0} = \sum_{\substack{j'=1 \\ j' \neq j}}^{N_\mathrm{T}} \left(\frac{\check{P}_{j'}}{1 + \check{P}_{j'} t(s_0)} \right)^2, \tag{67d}$$

$$M_{r,\mathrm{cov}} = \sum_{i=1}^{N_\mathrm{R}} \frac{\left(\frac{\lambda_i^{\boldsymbol{R}}}{N_\mathrm{R}} \right)^2}{\left(1 + \frac{\lambda_i^{\boldsymbol{R}}}{N_\mathrm{R}} r(0) \right) \left(1 + \frac{\lambda_i^{\boldsymbol{R}}}{N_\mathrm{R}} \left(s_0 \check{P}_j + r(s_0) \right) \right)}, \tag{67e}$$

$$M_{t,\mathrm{cov}} = \sum_{\substack{j'=1 \\ j' \neq j}}^{N_\mathrm{T}} \frac{\check{P}_{j'}^2}{\left(1 + \check{P}_{j'} t(0) \right) \left(1 + \check{P}_{j'} t(s_0) \right)}. \tag{67f}$$

M_{t,s_0} need not be actually calculated, since

$$v_1(s_0) + v_2(s_0) = -\ln \left| 1 - M_{r,0} M_{t,0} \right| - \ln \left| \check{P}_j^2 M_{r,s_0} \right| + 2 \ln \left| 1 - M_{r,\mathrm{cov}} M_{t,\mathrm{cov}} \right|. \tag{68}$$

Reversing (24),

$$\hat{\beta}'_{j,k} = \left(1 - \hat{\Delta}_{\mathrm{a},j} \hat{\beta}_{j,k} \right)^{-1} - 1. \tag{69}$$

The PDF of $\hat{\beta}_{j,k}$,

$$f_{\hat{\beta}_{j,k}} \left(\hat{\beta}_{j,k} \right) = \left(\left| \frac{\partial \hat{\beta}_{j,k}}{\partial \hat{\beta}'_{j,k}} \right| \right)^{-1} f_{\hat{\beta}'_{j,k}} \left(\hat{\beta}'_{j,k} \right) \tag{70}$$

$$= \frac{\hat{\Delta}_{\mathrm{a},j} \left(1 + \hat{\beta}'_{j,k} \right)^2}{\sqrt{2\pi}} \exp \left(s_0 \hat{\beta}'_{j,k} - I_{\mathrm{erg}}(s_0) + I_{\mathrm{erg}}(0) + \frac{v_1(s_0) + v_2(s_0)}{2} \right) \tag{71}$$

$$= \frac{\hat{\Delta}_{\mathrm{a},j}}{\left(1 - \hat{\Delta}_{\mathrm{a},j} \hat{\beta}_{j,k} \right)^2 \sqrt{2\pi}} \cdot \exp \left(s_0 \left(\frac{1}{1 - \hat{\Delta}_{\mathrm{a},j} \hat{\beta}_{j,k}} - 1 \right) - I_{\mathrm{erg}}(s_0) + I_{\mathrm{erg}}(0) + \frac{v_1(s_0) + v_2(s_0)}{2} \right). \tag{72}$$

Appendix 4 Closed formed mean of the effective SINR for uncorrelated MIMO channels

For vertically encoded MIMO, $\hat{\boldsymbol{\Delta}}_{\mathrm{a}} = \hat{\Delta}_{\mathrm{a}} \boldsymbol{I}_{N_{\mathrm{T}}}$ and $\boldsymbol{P} = N_{\mathrm{T}}^{-1} \boldsymbol{I}_{N_{\mathrm{T}}}$. Assume that $\boldsymbol{R} = \boldsymbol{I}_{N_{\mathrm{R}}}$. Then the frequency-bin-wise effective SINR after averaging over all the TX antennas

$$\hat{\beta}_k = N_{\mathrm{T}}^{-1} \mathrm{tr} \left\{ \sigma_\eta^2 \boldsymbol{I}_{N_{\mathrm{T}}} + \boldsymbol{P}^{\frac{1}{2}} \boldsymbol{\Psi}_k^{\mathrm{H}} \boldsymbol{R}^{\frac{\mathrm{T}}{2}} \left(\boldsymbol{R}^{\frac{1}{2}} \boldsymbol{\Psi}_k \hat{\boldsymbol{\Delta}}_{\mathrm{a}} \boldsymbol{P} \boldsymbol{\Psi}_k^{\mathrm{H}} \boldsymbol{R}^{\frac{\mathrm{T}}{2}} \right)^{-1} \boldsymbol{R}^{\frac{1}{2}} \boldsymbol{\Psi}_k \boldsymbol{P}^{\frac{1}{2}} \right\} \tag{73}$$

$$= N_{\mathrm{T}}^{-1} \mathrm{tr} \left\{ \sigma_\eta^2 \boldsymbol{I}_{N_{\mathrm{T}}} + \boldsymbol{P}^{\frac{1}{2}} \boldsymbol{\Psi}_k^{\mathrm{H}} \left(\hat{\Delta}_{\mathrm{a}} \boldsymbol{\Psi}_k \boldsymbol{P} \boldsymbol{\Psi}_k^{\mathrm{H}} \right)^{-1} \boldsymbol{\Psi}_k \boldsymbol{P}^{\frac{1}{2}} \right\} \tag{74}$$

$$= N_{\mathrm{T}}^{-1} \mathrm{tr} \left\{ \left(\frac{1}{\hat{\Delta}_{\mathrm{a}}} \boldsymbol{I}_{N_{\mathrm{T}}} - \frac{1}{\hat{\Delta}_{\mathrm{a}}} \left(\boldsymbol{I}_{N_{\mathrm{T}}} + \frac{\hat{\Delta}_{\mathrm{a}}}{\sigma_\eta^2} \boldsymbol{\Psi}_k^{\mathrm{H}} \boldsymbol{P} \boldsymbol{\Psi}_k \right)^{-1} \right) \right\} \tag{75}$$

$$= N_{\mathrm{T}}^{-1} \mathrm{tr} \left\{ \left(\frac{1}{\hat{\Delta}_{\mathrm{a}}} \boldsymbol{I}_{N_{\mathrm{T}}} - \frac{1}{\hat{\Delta}_{\mathrm{a}}} \left(\boldsymbol{I}_{N_{\mathrm{T}}} + \frac{N_{\mathrm{R}} \hat{\Delta}_{\mathrm{a}}}{N_{\mathrm{T}} \sigma_\eta^2} \check{\boldsymbol{\Psi}}_k^{\mathrm{H}} \check{\boldsymbol{\Psi}}_k \right)^{-1} \right) \right\}. \tag{76}$$

In step (75), the Woodbury matrix identity was used, while in step (76), $\check{\boldsymbol{\Psi}}_k = N_{\mathrm{R}}^{-1/2} \boldsymbol{\Psi}_k$. Although the distributions of $\hat{\beta}_k$ and $\hat{\beta}_{j,k}$ are not the same, $\mathrm{E}\left\{\hat{\beta}_k\right\} = \mathrm{E}\left\{\hat{\beta}_{j,k}\right\}$, since the elements of $\check{\boldsymbol{\Psi}}_k$ are IID. Thus, $\mathrm{E}\left\{\hat{\beta}_k\right\}$ can be used to estimate $\mathrm{var}\left(\hat{\beta}_{j,k}\right)$. The limiting Stieltjes transform is used to evaluate the asymptotic eigenvalues of the complex Wishart matrix $\check{\boldsymbol{\Psi}}_k^{\mathrm{H}} \check{\boldsymbol{\Psi}}_k$. Their empirical distribution converges almost surely, when $N_{\mathrm{T}}/N_{\mathrm{R}} = \zeta_{N_{\mathrm{R}}} \xrightarrow{N_{\mathrm{R}} \to \infty} \zeta$, to the Marčenko–Pastur law. Let λ_j^{W}, $j = 1, \ldots, N_{\mathrm{T}}$, denote the eigenvalues of the complex Wishart matrix $\check{\boldsymbol{\Psi}}_k^{\mathrm{H}} \check{\boldsymbol{\Psi}}_k$. Thus,

$$\mathrm{E}\left\{\hat{\beta}_k\right\} = \frac{1}{\hat{\Delta}_{\mathrm{a}}} \left(1 - \frac{1}{N_{\mathrm{T}}} \sum_{j=1}^{N_{\mathrm{T}}} \frac{1}{1 + \frac{N_{\mathrm{R}} \hat{\Delta}_{\mathrm{a}}}{N_{\mathrm{T}} \sigma_\eta^2} \lambda_j^{\mathrm{W}}} \right) \tag{77}$$

$$\to \frac{1}{\hat{\Delta}_{\mathrm{a}}} \left(1 - \int_0^\infty \frac{f_{\lambda_j^{\mathrm{W}}}\left(\lambda_j^{\mathrm{W}}\right)}{1 + \frac{N_{\mathrm{R}} \hat{\Delta}_{\mathrm{a}}}{N_{\mathrm{T}} \sigma_\eta^2} \lambda_j^{\mathrm{W}}} d\lambda_j^{\mathrm{W}} \right) \tag{78}$$

$$= \frac{1}{\hat{\Delta}_{\mathrm{a}}} \left(1 - \eta \left[\frac{N_{\mathrm{R}} \hat{\Delta}_{\mathrm{a}}}{N_{\mathrm{T}} \sigma_\eta^2} \right] \right) \tag{79}$$

$$= \frac{1}{\hat{\Delta}_{\mathrm{a}}} \left(1 - 1 + \frac{\mathcal{F}\left(\frac{N_{\mathrm{R}} \hat{\Delta}_{\mathrm{a}}}{N_{\mathrm{T}} \sigma_\eta^2}, \frac{N_{\mathrm{T}}}{N_{\mathrm{R}}} \right)}{4 \frac{N_{\mathrm{R}} \hat{\Delta}_{\mathrm{a}}}{N_{\mathrm{T}} \sigma_\eta^2} \frac{N_{\mathrm{T}}}{N_{\mathrm{R}}}} \right) \tag{80}$$

$$= \frac{\sigma_\eta^2}{4 \hat{\Delta}_{\mathrm{a}}^2} \mathcal{F}\left(\frac{N_{\mathrm{R}} \hat{\Delta}_{\mathrm{a}}}{N_{\mathrm{T}} \sigma_\eta^2}, \frac{N_{\mathrm{T}}}{N_{\mathrm{R}}} \right), \tag{81}$$

where $\mathcal{F}(\kappa_1, \kappa_2) = \left(\sqrt{\kappa_1 \left(1 + \sqrt{\kappa_2}\right)^2 + 1} - \sqrt{\kappa_1 \left(1 - \sqrt{\kappa_2}\right)^2 + 1} \right)^2$. The CLT was applied in step (78), while in steps (79) and (80), the η-transform from [321, Sect. 2.2.2] was used.

Appendix 5 PDF of LLR variance

Expressing $\hat{\beta}_j$ with respect to $\hat{\sigma}^2_{\mathrm{a},j}$,

$$\hat{\beta}_j = \frac{\hat{\sigma}^2_{\mathrm{a},j}}{4N_{\mathcal{M}} + \hat{\Delta}_{\mathrm{a},j}\hat{\sigma}^2_{\mathrm{a},j}}. \tag{82}$$

Since the distribution of $\hat{\beta}_j$ was approximated as Gaussian with mean $\mathrm{E}\left\{\hat{\beta}_{j,k}\right\}$ and variance $\mathrm{var}\left(\hat{\beta}_{j,k}\right)/L$,

$$f_{\hat{\sigma}^2_{\mathrm{a},j}}\left(\hat{\sigma}^2_{\mathrm{a},j}\right) \approx \left(\left|\frac{\partial\hat{\sigma}^2_{\mathrm{a},j}}{\partial\hat{\beta}_j}\right|\right)^{-1} f_{\hat{\beta}_j}\left(\hat{\beta}_j\right) \tag{83}$$

$$\approx \left(\left|\frac{4N_{\mathcal{M}}}{\left(1-\hat{\Delta}_{\mathrm{a},j}\hat{\beta}_j\right)^2}\right|\right)^{-1} \frac{1}{\sqrt{2\pi\frac{\mathrm{var}\left(\hat{\beta}_{j,k}\right)}{L}}} \exp\left(-\frac{\left(\hat{\beta}_j - \mathrm{E}\left\{\hat{\beta}_{j,k}\right\}\right)^2}{2\frac{\mathrm{var}\left(\hat{\beta}_{j,k}\right)}{L}}\right) \tag{84}$$

$$\approx \frac{\left(1-\hat{\Delta}_{\mathrm{a},j}\frac{\hat{\sigma}^2_{\mathrm{a},j}}{4N_{\mathcal{M}}+\hat{\Delta}_{\mathrm{a},j}\hat{\sigma}^2_{\mathrm{a},j}}\right)^2}{4N_{\mathcal{M}}} \frac{1}{\sqrt{2\pi\frac{\mathrm{var}\left(\hat{\beta}_{j,k}\right)}{L}}} \exp\left(-\frac{\left(\frac{\hat{\sigma}^2_{\mathrm{a},j}}{4N_{\mathcal{M}}+\hat{\Delta}_{\mathrm{a},j}\hat{\sigma}^2_{\mathrm{a},j}} - \mathrm{E}\left\{\hat{\beta}_{j,k}\right\}\right)^2}{2\frac{\mathrm{var}\left(\hat{\beta}_{j,k}\right)}{L}}\right) \tag{85}$$

$$\approx \frac{4N_{\mathcal{M}}}{(4N_{\mathcal{M}} + \hat{\Delta}_{\mathrm{a},j}\hat{\sigma}^2_{\mathrm{a},j})^2} \frac{1}{\sqrt{2\pi\frac{\mathrm{var}\left(\hat{\beta}_{j,k}\right)}{L}}} \exp\left(-\frac{\left(\frac{\hat{\sigma}^2_{\mathrm{a},j}}{4N_{\mathcal{M}}+\hat{\Delta}_{\mathrm{a},j}\hat{\sigma}^2_{\mathrm{a},j}} - \mathrm{E}\left\{\hat{\beta}_{j,k}\right\}\right)^2}{2\frac{\mathrm{var}\left(\hat{\beta}_{j,k}\right)}{L}}\right). \tag{86}$$

Appendix 6 FER computation formulae for a horizontally encoded or an MU-MIMO system with three or four spatial streams

When there are three spatial streams, the FER of the first stream,

$$\begin{aligned}\widetilde{\mathrm{FER}}_1 = &\left[1-\ddot{\mathcal{P}}_2^{\epsilon}\left(\hat{I}_{\mathrm{a},1}^{\mathrm{apr}},\hat{I}_{\mathrm{a},2}^{\mathrm{apr}}\,\middle|\,\hat{I}_{\mathrm{a},3}^{\mathrm{apr}}=0\right)\right]\cdot\\ &\left[\left[1-\ddot{\mathcal{P}}_3^{\epsilon}\left(\hat{I}_{\mathrm{a},1}^{\mathrm{apr}},\hat{I}_{\mathrm{a},3}^{\mathrm{apr}}\,\middle|\,\hat{I}_{\mathrm{a},2}^{\mathrm{apr}}\to 1\right)\right]\dot{\mathcal{P}}_1^{\epsilon}\left(\hat{I}_{\mathrm{a},1}^{\mathrm{apr}}\,\middle|\,\hat{I}_{\mathrm{a},2}^{\mathrm{apr}}\to 1,\hat{I}_{\mathrm{a},3}^{\mathrm{apr}}\to 1\right)+\right.\\ &\left.\ddot{\mathcal{P}}_3^{\epsilon}\left(\hat{I}_{\mathrm{a},1}^{\mathrm{apr}},\hat{I}_{\mathrm{a},3}^{\mathrm{apr}}\,\middle|\,\hat{I}_{\mathrm{a},2}^{\mathrm{apr}}\to 1\right)\dot{\mathcal{P}}_1^{\epsilon}\left(\hat{I}_{\mathrm{a},1}^{\mathrm{apr}}\,\middle|\,\hat{I}_{\mathrm{a},2}^{\mathrm{apr}}\to 1,\hat{I}_{\mathrm{a},3}^{\mathrm{apr}}=0\right)\right]+\\ &\ddot{\mathcal{P}}_2^{\epsilon}\left(\hat{I}_{\mathrm{a},1}^{\mathrm{apr}},\hat{I}_{\mathrm{a},2}^{\mathrm{apr}}\,\middle|\,\hat{I}_{\mathrm{a},3}^{\mathrm{apr}}=0\right)\left[\left[1-\ddot{\mathcal{P}}_3^{\epsilon}\left(\hat{I}_{\mathrm{a},1}^{\mathrm{apr}},\hat{I}_{\mathrm{a},3}^{\mathrm{apr}}\,\middle|\,\hat{I}_{\mathrm{a},2}^{\mathrm{apr}}=0\right)\right]\cdot\right.\\ &\left[\left[1-\ddot{\mathcal{P}}_2^{\epsilon}\left(\hat{I}_{\mathrm{a},1}^{\mathrm{apr}},\hat{I}_{\mathrm{a},2}^{\mathrm{apr}}\,\middle|\,\hat{I}_{\mathrm{a},3}^{\mathrm{apr}}\to 1\right)\right]\dot{\mathcal{P}}_1^{\epsilon}\left(\hat{I}_{\mathrm{a},1}^{\mathrm{apr}}\,\middle|\,\hat{I}_{\mathrm{a},2}^{\mathrm{apr}}\to 1,\hat{I}_{\mathrm{a},3}^{\mathrm{apr}}\to 1\right)+\right.\\ &\left.\ddot{\mathcal{P}}_2^{\epsilon}\left(\hat{I}_{\mathrm{a},1}^{\mathrm{apr}},\hat{I}_{\mathrm{a},2}^{\mathrm{apr}}\,\middle|\,\hat{I}_{\mathrm{a},3}^{\mathrm{apr}}\to 1\right)\dot{\mathcal{P}}_1^{\epsilon}\left(\hat{I}_{\mathrm{a},1}^{\mathrm{apr}}\,\middle|\,\hat{I}_{\mathrm{a},2}^{\mathrm{apr}}=0,\hat{I}_{\mathrm{a},3}^{\mathrm{apr}}\to 1\right)\right]+\\ &\left.\ddot{\mathcal{P}}_3^{\epsilon}\left(\hat{I}_{\mathrm{a},1}^{\mathrm{apr}},\hat{I}_{\mathrm{a},3}^{\mathrm{apr}}\,\middle|\,\hat{I}_{\mathrm{a},2}^{\mathrm{apr}}=0\right)\dot{\mathcal{P}}_1^{\epsilon}\left(\hat{I}_{\mathrm{a},1}^{\mathrm{apr}}\,\middle|\,\hat{I}_{\mathrm{a},2}^{\mathrm{apr}}=0,\hat{I}_{\mathrm{a},3}^{\mathrm{apr}}=0\right)\right].\end{aligned} \tag{87}$$

$\widetilde{\mathrm{FER}}_j$, $j=2,3$, are calculated by changing the indexing.

For four spatial streams, the FER of the first stream,

$$
\begin{aligned}
\widetilde{\mathrm{FER}}_1 \approx & \left[1-\ddot{\mathcal{P}}_2^{\epsilon}\left(\hat{I}_{\mathrm{a},1}^{\mathrm{apr}},\hat{I}_{\mathrm{a},2}^{\mathrm{apr}} \mid \hat{I}_{\mathrm{a},3}^{\mathrm{apr}}=0,\hat{I}_{\mathrm{a},4}^{\mathrm{apr}}=0\right)\right]\left[\left[1-\ddot{\mathcal{P}}_3^{\epsilon}\left(\hat{I}_{\mathrm{a},1}^{\mathrm{apr}},\hat{I}_{\mathrm{a},3}^{\mathrm{apr}} \mid \hat{I}_{\mathrm{a},2}^{\mathrm{apr}}\to 1,\hat{I}_{\mathrm{a},4}^{\mathrm{apr}}=0\right)\right]\cdot\right. \\
& \left[\left[1-\ddot{\mathcal{P}}_4^{\epsilon}\left(\hat{I}_{\mathrm{a},1}^{\mathrm{apr}},\hat{I}_{\mathrm{a},4}^{\mathrm{apr}} \mid \hat{I}_{\mathrm{a},2}^{\mathrm{apr}}\to 1,\hat{I}_{\mathrm{a},3}^{\mathrm{apr}}\to 1\right)\right]\dot{\mathcal{P}}_1^{\epsilon}\left(\hat{I}_{\mathrm{a},1}^{\mathrm{apr}} \mid \hat{I}_{\mathrm{a},2}^{\mathrm{apr}}\to 1,\hat{I}_{\mathrm{a},3}^{\mathrm{apr}}\to 1,\hat{I}_{\mathrm{a},4}^{\mathrm{apr}}\to 1\right)+\right. \\
& \left.\left.\ddot{\mathcal{P}}_4^{\epsilon}\left(\hat{I}_{\mathrm{a},1}^{\mathrm{apr}},\hat{I}_{\mathrm{a},4}^{\mathrm{apr}} \mid \hat{I}_{\mathrm{a},2}^{\mathrm{apr}}\to 1,\hat{I}_{\mathrm{a},3}^{\mathrm{apr}}\to 1\right)\dot{\mathcal{P}}_1^{\epsilon}\left(\hat{I}_{\mathrm{a},1}^{\mathrm{apr}} \mid \hat{I}_{\mathrm{a},2}^{\mathrm{apr}}\to 1,\hat{I}_{\mathrm{a},3}^{\mathrm{apr}}\to 1,\hat{I}_{\mathrm{a},4}^{\mathrm{apr}}=0\right)\right]+\right. \\
& \ddot{\mathcal{P}}_3^{\epsilon}\left(\hat{I}_{\mathrm{a},1}^{\mathrm{apr}},\hat{I}_{\mathrm{a},3}^{\mathrm{apr}} \mid \hat{I}_{\mathrm{a},2}^{\mathrm{apr}}\to 1,\hat{I}_{\mathrm{a},4}^{\mathrm{apr}}=0\right)\left[\left[1-\ddot{\mathcal{P}}_4^{\epsilon}\left(\hat{I}_{\mathrm{a},1}^{\mathrm{apr}},\hat{I}_{\mathrm{a},4}^{\mathrm{apr}} \mid \hat{I}_{\mathrm{a},2}^{\mathrm{apr}}\to 1,\hat{I}_{\mathrm{a},3}^{\mathrm{apr}}=0\right)\right]\cdot\right. \\
& \left[\left[1-\ddot{\mathcal{P}}_3^{\epsilon}\left(\hat{I}_{\mathrm{a},1}^{\mathrm{apr}},\hat{I}_{\mathrm{a},3}^{\mathrm{apr}} \mid \hat{I}_{\mathrm{a},2}^{\mathrm{apr}}\to 1,\hat{I}_{\mathrm{a},4}^{\mathrm{apr}}\to 1\right)\right]\dot{\mathcal{P}}_1^{\epsilon}\left(\hat{I}_{\mathrm{a},1}^{\mathrm{apr}} \mid \hat{I}_{\mathrm{a},2}^{\mathrm{apr}}\to 1,\hat{I}_{\mathrm{a},3}^{\mathrm{apr}}\to 1,\hat{I}_{\mathrm{a},4}^{\mathrm{apr}}\to 1\right)+\right. \\
& \left.\left.\ddot{\mathcal{P}}_3^{\epsilon}\left(\hat{I}_{\mathrm{a},1}^{\mathrm{apr}},\hat{I}_{\mathrm{a},3}^{\mathrm{apr}} \mid \hat{I}_{\mathrm{a},2}^{\mathrm{apr}}\to 1,\hat{I}_{\mathrm{a},4}^{\mathrm{apr}}\to 1\right)\dot{\mathcal{P}}_1^{\epsilon}\left(\hat{I}_{\mathrm{a},1}^{\mathrm{apr}} \mid \hat{I}_{\mathrm{a},2}^{\mathrm{apr}}\to 1,\hat{I}_{\mathrm{a},3}^{\mathrm{apr}}=0,\hat{I}_{\mathrm{a},4}^{\mathrm{apr}}\to 1\right)\right]+\right. \\
& \left.\left.\ddot{\mathcal{P}}_4^{\epsilon}\left(\hat{I}_{\mathrm{a},1}^{\mathrm{apr}},\hat{I}_{\mathrm{a},4}^{\mathrm{apr}} \mid \hat{I}_{\mathrm{a},2}^{\mathrm{apr}}\to 1,\hat{I}_{\mathrm{a},3}^{\mathrm{apr}}=0\right)\dot{\mathcal{P}}_1^{\epsilon}\left(\hat{I}_{\mathrm{a},1}^{\mathrm{apr}} \mid \hat{I}_{\mathrm{a},2}^{\mathrm{apr}}\to 1,\hat{I}_{\mathrm{a},3}^{\mathrm{apr}}=0,\hat{I}_{\mathrm{a},4}^{\mathrm{apr}}=0\right)\right]\right]+ \\
& \ddot{\mathcal{P}}_2^{\epsilon}\left(\hat{I}_{\mathrm{a},1}^{\mathrm{apr}},\hat{I}_{\mathrm{a},2}^{\mathrm{apr}} \mid \hat{I}_{\mathrm{a},3}^{\mathrm{apr}}=0,\hat{I}_{\mathrm{a},4}^{\mathrm{apr}}=0\right)\cdot \\
& \left[\left[1-\ddot{\mathcal{P}}_3^{\epsilon}\left(\hat{I}_{\mathrm{a},1}^{\mathrm{apr}},\hat{I}_{\mathrm{a},3}^{\mathrm{apr}} \mid \hat{I}_{\mathrm{a},2}^{\mathrm{apr}}=0,\hat{I}_{\mathrm{a},4}^{\mathrm{apr}}=0\right)\right]\left[\left[1-\ddot{\mathcal{P}}_2^{\epsilon}\left(\hat{I}_{\mathrm{a},1}^{\mathrm{apr}},\hat{I}_{\mathrm{a},2}^{\mathrm{apr}} \mid \hat{I}_{\mathrm{a},3}^{\mathrm{apr}}\to 1,\hat{I}_{\mathrm{a},4}^{\mathrm{apr}}=0\right)\right]\cdot\right.\right. \\
& \left[\left[1-\ddot{\mathcal{P}}_4^{\epsilon}\left(\hat{I}_{\mathrm{a},1}^{\mathrm{apr}},\hat{I}_{\mathrm{a},4}^{\mathrm{apr}} \mid \hat{I}_{\mathrm{a},2}^{\mathrm{apr}}\to 1,\hat{I}_{\mathrm{a},3}^{\mathrm{apr}}\to 1\right)\right]\cdot\dot{\mathcal{P}}_1^{\epsilon}\left(\hat{I}_{\mathrm{a},1}^{\mathrm{apr}} \mid \hat{I}_{\mathrm{a},2}^{\mathrm{apr}}\to 1,\hat{I}_{\mathrm{a},3}^{\mathrm{apr}}\to 1,\hat{I}_{\mathrm{a},4}^{\mathrm{apr}}\to 1\right)+\right. \\
& \left.\left.\ddot{\mathcal{P}}_4^{\epsilon}\left(\hat{I}_{\mathrm{a},1}^{\mathrm{apr}},\hat{I}_{\mathrm{a},4}^{\mathrm{apr}} \mid \hat{I}_{\mathrm{a},2}^{\mathrm{apr}}\to 1,\hat{I}_{\mathrm{a},3}^{\mathrm{apr}}\to 1\right)\dot{\mathcal{P}}_1^{\epsilon}\left(\hat{I}_{\mathrm{a},1}^{\mathrm{apr}} \mid \hat{I}_{\mathrm{a},2}^{\mathrm{apr}}\to 1,\hat{I}_{\mathrm{a},3}^{\mathrm{apr}}\to 1,\hat{I}_{\mathrm{a},4}^{\mathrm{apr}}=0\right)\right]+\right. \\
& \ddot{\mathcal{P}}_2^{\epsilon}\left(\hat{I}_{\mathrm{a},1}^{\mathrm{apr}},\hat{I}_{\mathrm{a},2}^{\mathrm{apr}} \mid \hat{I}_{\mathrm{a},3}^{\mathrm{apr}}\to 1,\hat{I}_{\mathrm{a},4}^{\mathrm{apr}}=0\right)\left[\left[1-\ddot{\mathcal{P}}_4^{\epsilon}\left(\hat{I}_{\mathrm{a},1}^{\mathrm{apr}},\hat{I}_{\mathrm{a},4}^{\mathrm{apr}} \mid \hat{I}_{\mathrm{a},2}^{\mathrm{apr}}=0,\hat{I}_{\mathrm{a},3}^{\mathrm{apr}}\to 1\right)\right]\cdot\right. \\
& \left[\left[1-\ddot{\mathcal{P}}_2^{\epsilon}\left(\hat{I}_{\mathrm{a},1}^{\mathrm{apr}},\hat{I}_{\mathrm{a},2}^{\mathrm{apr}} \mid \hat{I}_{\mathrm{a},3}^{\mathrm{apr}}\to 1,\hat{I}_{\mathrm{a},4}^{\mathrm{apr}}\to 1\right)\right]\dot{\mathcal{P}}_1^{\epsilon}\left(\hat{I}_{\mathrm{a},1}^{\mathrm{apr}} \mid \hat{I}_{\mathrm{a},2}^{\mathrm{apr}}\to 1,\hat{I}_{\mathrm{a},3}^{\mathrm{apr}}\to 1,\hat{I}_{\mathrm{a},4}^{\mathrm{apr}}\to 1\right)+\right. \\
& \left.\left.\ddot{\mathcal{P}}_2^{\epsilon}\left(\hat{I}_{\mathrm{a},1}^{\mathrm{apr}},\hat{I}_{\mathrm{a},2}^{\mathrm{apr}} \mid \hat{I}_{\mathrm{a},3}^{\mathrm{apr}}\to 1,\hat{I}_{\mathrm{a},4}^{\mathrm{apr}}\to 1\right)\dot{\mathcal{P}}_1^{\epsilon}\left(\hat{I}_{\mathrm{a},1}^{\mathrm{apr}} \mid \hat{I}_{\mathrm{a},2}^{\mathrm{apr}}=0,\hat{I}_{\mathrm{a},3}^{\mathrm{apr}}\to 1,\hat{I}_{\mathrm{a},4}^{\mathrm{apr}}\to 1\right)\right]+\right. \\
& \left.\left.\ddot{\mathcal{P}}_4^{\epsilon}\left(\hat{I}_{\mathrm{a},1}^{\mathrm{apr}},\hat{I}_{\mathrm{a},4}^{\mathrm{apr}} \mid \hat{I}_{\mathrm{a},2}^{\mathrm{apr}}=0,\hat{I}_{\mathrm{a},3}^{\mathrm{apr}}\to 1\right)\dot{\mathcal{P}}_1^{\epsilon}\left(\hat{I}_{\mathrm{a},1}^{\mathrm{apr}} \mid \hat{I}_{\mathrm{a},2}^{\mathrm{apr}}=0,\hat{I}_{\mathrm{a},3}^{\mathrm{apr}}\to 1,\hat{I}_{\mathrm{a},4}^{\mathrm{apr}}=0\right)\right]\right]+ \\
& \ddot{\mathcal{P}}_3^{\epsilon}\left(\hat{I}_{\mathrm{a},1}^{\mathrm{apr}},\hat{I}_{\mathrm{a},3}^{\mathrm{apr}} \mid \hat{I}_{\mathrm{a},2}^{\mathrm{apr}}=0,\hat{I}_{\mathrm{a},4}^{\mathrm{apr}}=0\right)\cdot \\
& \left[\left[1-\ddot{\mathcal{P}}_4^{\epsilon}\left(\hat{I}_{\mathrm{a},1}^{\mathrm{apr}},\hat{I}_{\mathrm{a},4}^{\mathrm{apr}} \mid \hat{I}_{\mathrm{a},2}^{\mathrm{apr}}=0,\hat{I}_{\mathrm{a},3}^{\mathrm{apr}}=0\right)\right]\left[\left[1-\ddot{\mathcal{P}}_2^{\epsilon}\left(\hat{I}_{\mathrm{a},1}^{\mathrm{apr}},\hat{I}_{\mathrm{a},2}^{\mathrm{apr}} \mid \hat{I}_{\mathrm{a},3}^{\mathrm{apr}}=0,\hat{I}_{\mathrm{a},4}^{\mathrm{apr}}\to 1\right)\right]\cdot\right.\right. \\
& \left[1-\ddot{\mathcal{P}}_3^{\epsilon}\left(\hat{I}_{\mathrm{a},1}^{\mathrm{apr}},\hat{I}_{\mathrm{a},3}^{\mathrm{apr}} \mid \hat{I}_{\mathrm{a},2}^{\mathrm{apr}}\to 1,\hat{I}_{\mathrm{a},4}^{\mathrm{apr}}\to 1\right)\right]\dot{\mathcal{P}}_1^{\epsilon}\left(\hat{I}_{\mathrm{a},1}^{\mathrm{apr}} \mid \hat{I}_{\mathrm{a},2}^{\mathrm{apr}}\to 1,\hat{I}_{\mathrm{a},3}^{\mathrm{apr}}\to 1,\hat{I}_{\mathrm{a},4}^{\mathrm{apr}}\to 1\right)+ \\
& \left.\left.\ddot{\mathcal{P}}_3^{\epsilon}\left(\hat{I}_{\mathrm{a},1}^{\mathrm{apr}},\hat{I}_{\mathrm{a},3}^{\mathrm{apr}} \mid \hat{I}_{\mathrm{a},2}^{\mathrm{apr}}\to 1,\hat{I}_{\mathrm{a},4}^{\mathrm{apr}}\to 1\right)\dot{\mathcal{P}}_1^{\epsilon}\left(\hat{I}_{\mathrm{a},1}^{\mathrm{apr}} \mid \hat{I}_{\mathrm{a},2}^{\mathrm{apr}}\to 1,\hat{I}_{\mathrm{a},3}^{\mathrm{apr}}=0,\hat{I}_{\mathrm{a},4}^{\mathrm{apr}}\to 1\right)\right]+\right. \\
& \ddot{\mathcal{P}}_2^{\epsilon}\left(\hat{I}_{\mathrm{a},1}^{\mathrm{apr}},\hat{I}_{\mathrm{a},2}^{\mathrm{apr}} \mid \hat{I}_{\mathrm{a},3}^{\mathrm{apr}}=0,\hat{I}_{\mathrm{a},4}^{\mathrm{apr}}\to 1\right)\left[\left[1-\ddot{\mathcal{P}}_3^{\epsilon}\left(\hat{I}_{\mathrm{a},1}^{\mathrm{apr}},\hat{I}_{\mathrm{a},3}^{\mathrm{apr}} \mid \hat{I}_{\mathrm{a},2}^{\mathrm{apr}}=0,\hat{I}_{\mathrm{a},4}^{\mathrm{apr}}\to 1\right)\right]\cdot\right. \\
& \left[1-\ddot{\mathcal{P}}_2^{\epsilon}\left(\hat{I}_{\mathrm{a},1}^{\mathrm{apr}},\hat{I}_{\mathrm{a},2}^{\mathrm{apr}} \mid \hat{I}_{\mathrm{a},3}^{\mathrm{apr}}\to 1,\hat{I}_{\mathrm{a},4}^{\mathrm{apr}}\to 1\right)\right]\dot{\mathcal{P}}_1^{\epsilon}\left(\hat{I}_{\mathrm{a},1}^{\mathrm{apr}} \mid \hat{I}_{\mathrm{a},2}^{\mathrm{apr}}\to 1,\hat{I}_{\mathrm{a},3}^{\mathrm{apr}}\to 1,\hat{I}_{\mathrm{a},4}^{\mathrm{apr}}\to 1\right)+ \\
& \left.\left.\ddot{\mathcal{P}}_2^{\epsilon}\left(\hat{I}_{\mathrm{a},1}^{\mathrm{apr}},\hat{I}_{\mathrm{a},2}^{\mathrm{apr}} \mid \hat{I}_{\mathrm{a},3}^{\mathrm{apr}}\to 1,\hat{I}_{\mathrm{a},4}^{\mathrm{apr}}\to 1\right)\dot{\mathcal{P}}_1^{\epsilon}\left(\hat{I}_{\mathrm{a},1}^{\mathrm{apr}} \mid \hat{I}_{\mathrm{a},2}^{\mathrm{apr}}=0,\hat{I}_{\mathrm{a},3}^{\mathrm{apr}}\to 1,\hat{I}_{\mathrm{a},4}^{\mathrm{apr}}\to 1\right)\right]+\right. \\
& \left.\left.\ddot{\mathcal{P}}_3^{\epsilon}\left(\hat{I}_{\mathrm{a},1}^{\mathrm{apr}},\hat{I}_{\mathrm{a},3}^{\mathrm{apr}} \mid \hat{I}_{\mathrm{a},2}^{\mathrm{apr}}=0,\hat{I}_{\mathrm{a},4}^{\mathrm{apr}}\to 1\right)\dot{\mathcal{P}}_1^{\epsilon}\left(\hat{I}_{\mathrm{a},1}^{\mathrm{apr}} \mid \hat{I}_{\mathrm{a},2}^{\mathrm{apr}}=0,\hat{I}_{\mathrm{a},3}^{\mathrm{apr}}=0,\hat{I}_{\mathrm{a},4}^{\mathrm{apr}}\to 1\right)\right]\right]+ \\
& \ddot{\mathcal{P}}_4^{\epsilon}\left(\hat{I}_{\mathrm{a},1}^{\mathrm{apr}},\hat{I}_{\mathrm{a},4}^{\mathrm{apr}} \mid \hat{I}_{\mathrm{a},2}^{\mathrm{apr}}=0,\hat{I}_{\mathrm{a},3}^{\mathrm{apr}}=0\right)\dot{\mathcal{P}}_1^{\epsilon}\left(\hat{I}_{\mathrm{a},1}^{\mathrm{apr}} \mid \hat{I}_{\mathrm{a},2}^{\mathrm{apr}}=0,\hat{I}_{\mathrm{a},3}^{\mathrm{apr}}=0,\hat{I}_{\mathrm{a},4}^{\mathrm{apr}}=0\right)\Big].
\end{aligned}
\tag{88}
$$

As before $\widetilde{\mathrm{FER}}_j$, $j=2,3,4$, are calculated by changing the indexing.

547. Pääkkönen, Tiina (2015) Improving the energy efficiency of processes : reduction of the crystallization fouling of heat exchangers

548. Ylä-Mella, Jenni (2015) Strengths and challenges in the Finnish waste electrical and electronic equipment recovery system : consumers' perceptions and participation

549. Skön, Jukka-Pekka (2015) Intelligent information processing in building monitoring systems and applications

550. Irannezhad, Masoud (2015) Spatio-temporal climate variability and snow resource changes in Finland

551. Pekkinen, Leena (2015) Information processing view on collaborative risk management practices in project networks

552. Karjalainen, Mikko (2015) Studies on wheat straw pulp fractionation : fractionation tendency of cells in pressure screening, hydrocyclone fractionation and flotation

553. Nelo, Mikko (2015) Inks based on inorganic nanomaterials for printed electronics applications

554. Kursu, Olli-Erkki (2015) Micromotion compensation and a neural recording and stimulation system for electrophysiological measurements

555. Hallman, Lauri (2015) Single photon detection based devices and techniques for pulsed time-of-flight applications

556. Omran, Mamdouh (2015) Microwave dephosphorisation of high phosphorus iron ores of the Aswan region, Egypt : developing a novel process for high phosphorus iron ore utilization

557. Kiljander, Jussi (2016) Semantic interoperability framework for smart spaces

558. Aula, Matti (2016) Optical emission from electric arc furnaces

559. Ferdinand, Nuwan Suresh (2016) Low complexity lattice codes for communication networks

560. Xue, Qiang (2016) Analysis of near-optimal relaying schemes for wireless tandem and multicast relay networks

561. Rautio, Anne-Riikka (2016) On the stability of carbon nanotube and titania nanowire based catalyst materials : from synthesis to applications

562. Kuokkanen, Ville (2016) Utilization of electrocoagulation for water and wastewater treatment and nutrient recovery : techno-economic studies

Book orders:
Granum: Virtual book store
http://granum.uta.fi/granum/

UNIVERSITY OF OULU P.O. Box 8000 FI-90014 UNIVERSITY OF OULU FINLAND

ACTA UNIVERSITATIS OULUENSIS

UNIVERSITY of OULU
OULUN YLIOPISTO

ISBN 978-952-62-1146-6 (Paperback)
ISBN 978-952-62-1147-3 (PDF)
ISSN 0355-3213 (Print)
ISSN 1796-2226 (Online)